Stable Isotopes in Unstable Times:

A geochemical investigation of the end Cretaceous mass extinction

Thomas S. Tobin

A thesis

Submitted in partial fulfillment of the

Requirements for the degree of

Doctor of Philosophy

University of Washington

2014

Reading Committee

Peter Ward, Chair

Greg Wilson

Eric Steig

Program Authorized to Offer Degree

Earth and Space Sciences

University of Washington

Abstract

Stable Isotopes in Unstable Times:

A geochemical investigation of the end Cretaceous mass extinction

Thomas Tobin

Chair of Supervisory Committee

Professor Peter Ward

Department of Earth and Space Sciences

This primary goal of this dissertation is to increase understanding of the end Cretaceous (or Cretaceous – Paleogene or K-Pg) mass extinction through the use of light stable isotope geochemistry. These studies attempt to examine any climatic and environmental changes that occurred around the K-Pg boundary, and might have contributed to the K-Pg mass extinction, specifically by examining isotopic records at high stratigraphic resolution around the boundary. Studies are completed in two field areas, the Antarctic Peninsula and eastern Montana, USA, both of which preserve the K-Pg boundary. While these works, like most scientific studies, lead to further questions that warrant investigation and confirmation, they generally support the idea the end Cretaceous mass extinction was more complicated than a simple asteroid strike.

This dissertation is comprised of five scientific chapters as well as short introductory and concluding sections. The introduction explains the background and context behind each study, and the process by which I ultimately worked with a wide variety of co-authors to complete the various projects. The conclusion begins the process of examining the differences and similarities of each study, and explores further avenues of research to test some of the proposed hypotheses or reconcile potentially contradictory data. Four of the chapters are written as scientific manuscripts, while a fifth chapter details the work done as part of my astrobiology rotation.

Chapter 1 (Tobin et al., 2011) outlines the discovery of analytical errors in the typical process of measuring carbonate stable isotopes ($\delta^{13}C$ and $\delta^{18}O$) on small sample sizes of powder. Carbonate material is typically prepared using one of two methods, either by drilling using a high speed drill or micromill, or by crushing a sample using a mortar and pestle. Drilling produces a finer grain size of material, which is consequently more prone to being altered in its $\delta^{18}O$ value during a typical automated measurement process, while the sample is waiting in the queue to be analyzed. This chapter outlines the specific parameters under which this phenomenon occurs, and describes a correction procedure, though we encourage every lab to develop their own correction scheme.

Chapter 2 (Tobin and Ward, submitted) is the second of two papers (in order of analysis and publication, but first presented here) that analyze and interpret $\delta^{13}C$ and $\delta^{18}O$ values from molluscan shell carbonate collected on the Antarctic Peninsula, though a small amount of fossil shell material was also used in Chapter 1. In this study, we examine trends in $\delta^{13}C$ for ammonites and other benthic mollusks using our own collections with added samples coming from collections currently housed at the Paleontological Research Institute (PRI). In both collections we find a notable offset in $\delta^{13}C$ between ammonites and benthic mollusks, though good correspondence in $\delta^{18}O$. Ultimately, the best interpretation of this pattern is that ammonites are incorporating more respired CO_2 into their shell material, potentially from a higher metabolic rate. A more active

lifestyle could potentially have increased the susceptibility of ammonites to an event like bolide impact at the end of the Cretaceous.

Chapter 3 (Tobin et al., 2012) also looks at isotopic records, in this case focusing on $\delta^{18}O$ values, for fossil mollusks from Antarctica. Paleotemperature can generally be inferred from $\delta^{18}O$ values if the $\delta^{18}O$ of the water from which it came can be estimated reliably, as is generally thought to be the case for seawater during the Cretaceous. We generate a time series of $\delta^{18}O$ across the K-Pg boundary. We also generated a magnetostratigraphic record for the section, as well as paleobiological data in the same stratigraphic context. Statistical analysis revealed two extinction events, one at the peak of warming from the paleotemperature record (50 meters below the K-Pg boundary), the other simultaneous with the iridium anomaly indicating the asteroid strike. The warming events are also correlated (using magnetostratigraphy) with the timing of Deccan Traps volcanism, which could potentially generate warming via CO_2 emission. The evidence is most consistent multiple causes contributing to the end Cretaceous mass extinction over a short geological interval. The plausibility of the Deccan – warming link is explored in Chapter 5, though it is ultimately inconclusive due to the uncertainty in total volumes of CO_2 emitted during this event.

Chapter 4 (Tobin et al., 2014) performs a similar analysis to that in Chapter 3, but on freshwater mollusks from eastern Montana. Because the paleo-depositional setting was fluvial/lacustrine, traditional $\delta^{18}O$ paleotemperature reconstruction is not a useful tool. Carbonate clumped isotope paleothermometry, while more challenging analytically, avoids this problem, and was used to generate a temperature record across the K-Pg boundary. A cooling trend in summer temperatures was identified in the last ~30 meters of the Cretaceous (though bivalve nutrient stress could plausibly explain the pattern as well). This pattern occurs over the same stratigraphic interval that vertebrate paleontologists have identified biodiversity changes, and could plausibly be related. As with Chapter 3, this study is most consistent with a multiple cause mass extinction.

Table of Contents

APPENDICES

List of Figures

To my parents, Graham Tobin and Elizabeth Bird, who have encouraged my curiosity about the natural world since I was a child hunting agates along the shores of Lake Superior. Your continual love and support has helped me grow into the person I am today. Thank you.

Acknowledgements

Here I would like to acknowledge people who have been supportive of my time in graduate school and have made the six years at the University of Washington an enjoyable experience; I have acknowledged scientific assistance and funding sources for each chapter individually.

I would like to start by thanking my advisor, Peter Ward, who pulled my application out of the pile and called me with an invitation to Antarctica. Despite having a project in place, he gave me the freedom to pursue my own research in the directions that excited me. Part of that freedom allowed me to work with Greg Wilson, who let me piggyback on his project and complete research I could not have done without his assistance. I also appreciate the guidance and advice from the rest of my committee, Eric Steig, Cecilia Bitz, and Andrew Connolly.

Thanks also to Joe Kirschvink and John Eiler at Caltech, who both made their laboratories available to me on multiple occasions, which led me to explore new avenues of research that were previously unavailable to me. In addition to those listed above or in my lab, many others have assisted me in some way in the field in Antarctica (Eduardo Olivero, Stian Alesandrini, Melissa Rider, Tomas Wagener, Lauren Edgar, Sarah Slotznick) and in Montana (Dave Demar, Shelly Donohue, Lauren Berg Debey, Stephanie Smith), as well as in the Isolab (Andy Schauer, Kyle Samek, Rebecca Teel).

I am very thankful for the support from the other graduate students in my lab, Kelly Hillbun, Dave Smith, Shane Schoepfer, and Ricky Dooley. They have all increased my enjoyment and the success of field expeditions and been good and reliable friends. My graduate career has also been made much more fun by all of my friends currently in, and graduated from, the Earth and Space Sciences department; a complete list is far too long to include here. The graduate student community was one of the best parts of working at the University of Washington. I would also like to thank the Paleo Lunch and Astrobiology students, who have enriched my academic experience.

I also thank my family, including my parents Graham Tobin and Elizabeth Bird, to whom this dissertation is dedicated, and my brother, Dan Tobin. Finally, I want to thank my girlfriend, Emily Tompkins, for her love and support over our graduate and undergraduate schooling, especially through the periods of long distance and field work.

Introduction

Five major biological crises, the so called “big five” mass extinctions (Raup and Sepkoski, 1982; Sepkoski Jr., 1997), have been recognized over the Phanerozoic period (542 Ma), as have a number of less severe “minor” mass extinctions. Catastrophic extinctions of microscopic life have been theorized to have occurred in Precambrian, but the fossil record of life over this period is too poor for us to be sure. Some effort has been made to identify cyclicity in their patterns , but these efforts have been generally unsuccessful (Rohde and Muller, 2005). While there may be causal mechanisms that are common to some or all mass extinctions, better understanding of each individual mass extinction must be established first.

Mass extinctions appear to be unique periods in the history of earth where typical extinction selectivity patterns are different than ‘background’ periods (Purvis, 2000). Due both to the uniqueness of their selectivity and the magnitude of their severity, these events have had a profound effect on the trajectory of life on earth. Mass extinctions are so important to biota of earth that they are targeted as a field of study by the NASA astrobiology roadmap (specifically Goals 4 and 5). While potential mass extinction causal mechanisms like extraterrestrial bolide impacts are likely universal to any life that has emerged elsewhere in the universe, other proposed causes, like flood basalt volcanism, marine regression ,and global glaciation, are likely more specific to earth. However, the evolutionary pressures of catastrophic events of any kind are likely to follow the patterns observed in our terrestrial mass extinctions regardless of cause.

The end Cretaceous mass extinction is the most recent and well-studied of the ‘Big Five’ mass extinctions. This event occurred at (and in some ways defines) the Cretaceous – Paleogene (K-Pg) boundary, previously called Cretaceous – Tertiary (K-T) boundary, a stratigraphic division that has recently been reclassified. This document used both end Cretaceous mass extinction and K-Pg mass extinction to refer to the same event. Evidence for a large (≈ 10 km diameter) bolide impact

at the K-Pg boundary was discovered over 30 years ago and has since been refined (Alvarez et al., 1980; Hildebrand et al., 1991). A vast majority of geologists accept that this event was contemporaneous, or nearly so, with the extinction of previously widespread geologic groups (e.g. ammonites, non-avian dinosaurs), but the relative importance of the bolide impact as a causal mechanism is still the subject of some debate in the paleontological community (Archibald et al., 2010; Courtillot and Fluteau, 2010; Keller et al., 2010; Schulte et al., 2010). Few researchers, though there are some exceptions, believe that the bolide impact was inconsequential, but there are some who believe the evidence points to a more complex interplay between more gradual climatic changes and the sudden bolide impact (Arens and West, 2008; Gertsch et al., 2011; Mitchell et al., 2012; Scheffer et al., 2001; Wilson et al., 2014).

Even events considered long-term by modern human standards, like climate change, can occur on scales that are very short, and therefore difficult to resolve, in a geologic context. Consequently, difficulties have arisen in our ability to rigorously compare multiple hypotheses about the cause or causes of many mass extinctions. As the most recent of the big five mass extinctions, the K-Pg extinction is the most likely to yield stratigraphic sections with high temporal resolution. The K-Pg event also has the only undisputed evidence for a bolide impact, as proposed extraterrestrial evidence at other mass extinction boundaries have generally not been accepted by the scientific community.

The primary goal of this dissertation is to examine the events around the K-Pg boundary in order to determine if any proposed environmental contributions to the mass extinction can be resolved, and if they appear to have any effect on the biota over that same time period. It is important not only to identify whether such climatic perturbations occurred, but whether they occurred with the right timing relative to biotic records to have been a plausible contribution to the causes of the mass extinction. The primary means by which I have examined paleoclimatic variation

is through light stable isotope geochemistry, specifically carbon ($\delta^{13}C$), oxygen ($\delta^{18}O$), and combined – or clumped – isotope (Δ_{47}) analysis. Most of these analyses have been completed on fossil material from stratigraphic sections on Seymour Island, Antarctica, with another study completed in the Hell Creek area of eastern Montana. Both of these locations have deposition crossing the K-Pg boundary, but with very different environmental and geographical conditions.

Apart from the introductory and concluding chapters, this dissertation is comprised of four scientific chapters, each of which also stands alone as a scientific paper. Three of the four have been published already, with a fourth having recently been submitted. The concluding chapter compares the results of each more directly with each other, in a way that was somewhat beyond the scope of each individual study. While the work in total contributes to our understanding of the end Cretaceous mass extinction, it also raises new questions that should be addressed, and I hope to work towards answering those questions in my research as my career continues.

Below I will briefly explain the context and background of each of the chapters, specifically why the individual scientific questions were asked, and how they were answered. Taken individually, each of the chapters may appear to be somewhat disconnected from the others, but they all grew out of the same research goals and contribute to our understanding of stable isotopic records around the K-Pg boundary. I was fortunate that I was able to work with a wide variety of co-authors, on the separate papers, which gave me a range of views on how to complete and write a scientific manuscript.

The first of these chapters (Chapter 1) focuses on methodological changes to way stable isotope measurements are performed in the UW IsoLab, as well as in other labs around the country (Tobin et al., 2011). We were attempting to generate oxygen isotope ($\delta^{18}O$) records from fossil shell carbonates, both aragonite and calcite, across K-Pg boundary from Seymour Island. However, I noticed that replicate measurements on the same powders completed in different analytical groups

were not always consistent, and often had systematic biases between groups. It took some time to pin down the source of the error, but working with Andrew Schauer, the lab manager for the IsoLab, we explored a number of possibilities. The direction of change in the $\delta^{18}O$ values for later analyses was consistent and in the direction of sample alteration, which suggested to us that something was happening to samples that were prepared and untouched for a long period of time between analyses. None of our initial experimental attempts at the effects of 'storage time' were able to replicate the observed results. We also explored the effect of mineralogy, reasoning that aragonite is metastable at earth surface temperature and pressure, and might be more likely alter during long term storage, but this also proved to be incorrect.

We finally determined that alteration was happening, not during long term storage, but during short term storage immediately prior to analysis. It was common practice in our lab, and other labs (the measurement device is built for this protocol), for samples weighed and ready for analysis to be stored in the processing machine (Kiel III Device) prior to their analysis. The Kiel device is effectively a low temperature (70°C) oven to facilitate that the acid digestion of carbonates, and storage in the device was thought to minimize the water interaction with the sample to minimize alteration. Unfortunately, we found that storing finely powdered samples in the device would cause them to begin to alter their isotopic values, with the alteration dependent on the time spend in the Kiel device. It took some time to reach this conclusion, as more coarsely powdered specimens were not susceptible to this type of alteration. My third co-author, undergraduate Evan Lewarch, assisted in a more thorough investigation of this phenomenon, preparing and analyzing suites of samples to test the predictability and consistency of the alteration. Ultimately, we were able to create a way of correcting for this problem, and changed our lab protocol to stop the pre-storage of samples at elevated temperatures, and instead to store the samples in a room temperature desiccator. Even with a changed protocol the correction procedure is still in use, as the last samples analyzed in a group have still been in the Kiel for almost 24 hours.

Having determined the source of the measurement problems in Chapter 1, I was then able to complete the analyses for $\delta^{18}O$ and $\delta^{13}C$ from Seymour Island which now include Chapter 3 (Tobin et al., 2012) and part of Chapter 2 (Tobin and Ward, submitted). Seymour Island is located just off the Antarctic Peninsula, and is part of larger island basin called the James Ross Island Basin which includes sediments of Coniacian through Danian age, as well as overlying Eocene deposits. Seymour Island contains the Maastrichtian (Cretaceous) and Danian (Paleogene) stages, and continuous sedimentation across the K-Pg boundary. Fossils there are very well preserved, both physically and chemically, and consequently make excellent targets for isotope geochemistry and paleobiological investigations. One of the major geological difficulties with working in this area is that precise correlations with elsewhere around the world are difficult, due to endemic ammonite groups (challenging biostratigraphy), and lack of radiometric age dating targets.

Work on Seymour Island was completed as part of a large team, including scientists (and co-authors) from Caltech and CADIC in Argentina. My work was focused on the geochemical and paleobiological data, and the Caltech group, led by Joseph Kirschvink, generated magnetostratigraphic records that allowed us to correlate Seymour Island with global events. I would later complete paleomagnetic analyses at the Caltech lab under the direction of Kirschvink to create a similar record for the whole James Ross Island Basin. This work will be written up separately (and after) my dissertation, as it is neither geochemical nor directly related to the K-Pg extinction.

By combining our geochemical data with new and previously published paleobiological data, we were able to determine that there was substantial warming in the latest part of the Cretaceous. This warming was synchronous with a local multi-species extinction that was stratigraphically lower than a second local multi-species extinction at the precise K-Pg boundary (as determined by previous workers finding the iridium anomaly). This period of warming is

coincident with the main phase of Deccan traps flood volcanism, which can be well correlated with our section using the magnetostratigraphy. Ultimately the evidence from this study is consistent with both volcanism forced climate change and the bolide impact influencing the overall end Cretaceous mass extinction. These events happened geologically very close together, and it likely that in other sections around the globe that they would time-averaged together and not resolvable.

The warming – volcanism link was explored further by some simple climate modelling in Chapter 5. This work was completed as part of my astrobiology research rotation but was not explored fully enough to generate a scientific manuscript. A box model based off GEOCARB III was employed to examine the effects of CO_2 perturbations to the Cretaceous atmosphere. Ultimately, we concluded that any warming experienced from flood volcanic CO_2 release was not strongly dependent on total emission duration of the volcanic episode, or on the number of individual emission events over the total duration of the episode. This effect was primarily due to the relatively long time that CO_2 remains in the atmosphere. However, the total volume of CO_2 released was very important for the resultant warming; unfortunately the published estimates for this volume range over almost two orders of magnitude. Given these estimates, the warming observed in Chapter 3 can be plausibly generated by Deccan volcanism.

In the course of the isotopic measurements completed for Chapter 3, the analytical methods I employed also generate carbon isotopic values ($\delta^{13}C$) in addition to $\delta^{18}O$. As these values were generated from a range of different biological groups, an important step in the quality control for Chapter 3 was a comparison of variation between biological groups. No differences were seen in $\delta^{18}O$, but there was a systematic offset in $\delta^{13}C$ between ammonites and the other benthic mollusks. In Chapter 2, I explored some of the potential causes for this anomaly, as it may shed some light on the reason ammonites, and not other shelled mollusks, became extinct at the end of the Cretaceous (Tobin and Ward, submitted).

While there were overall population differences in $\delta^{13}C$ between ammonites and benthic mollusks, I wanted more samples to better quantify the pattern. There were no more immediate opportunities for field work to collect more samples on that island, so I visited previously collected specimens at the Paleontological Research Institute. From these samples, I generated a reasonably comparable isotopic record, albeit with poorer stratigraphic control. The $\delta^{18}O$ results from this study compared very well with those from our UW collection, and yield a higher confidence in our paleotemperature record. Similarly, we also continued to see the offset between ammonites and other mollusks in the carbon isotopic record.

The $\delta^{13}C$ offset could theoretically be caused by a number of different phenomena. We were able to rule out some possibilities by ensuring that the pattern was not an issue of comparing different stratigraphic horizons and by quantifying the magnitude of the difference (>3.0‰). Two possible explanations remained. The first, that ammonites are in some way influenced by significantly depleted carbon from cold methane seeps, is plausible, though unlikely, given that this pattern has been observed in other population studies around the globe, and the ammonites record the same water temperature as the benthic mollusks. Our evidence may explain the $\delta^{13}C$ values at geologically clear methane seeps, instead of attributing the isotopic values to the methane seep itself (Landman et al., 2012). Instead, we believe it is more likely that ammonites incorporate respired CO_2 into their shell material due to constricted exchange of their extra-palial fluid with the ocean. Alternatively, their metabolic rate could have been significantly increased, indicating that they were very active swimmers and feeders. This active need may be the reason ammonites were more susceptible to a sudden catastrophic event like the bolide impact at the end of the Cretaceous.

In the process of completing analysis for Chapter 2, I was able to confirm the temperature record that was published and now comprises Chapter 3 of this dissertation. While the temperature patterns we observed from Antarctica match those of other ocean sites in the Atlantic and Indian

oceans, it is not clear how global the pattern is, and particular whether terrestrial environments were responding the same way. I wanted to generate a similar paleotemperature record from another outcrop environment, as it would allow substantial macrofossil paleobiological data to be compared with the temperature record, which is not possible from analysis of core. I also wanted to test a terrestrial environment.

Fortunately for me, a member of my committee, Greg Wilson, was leading a project in the terrestrial K-Pg sediments of eastern Montana, in the Hell Creek area. His project had been focusing mostly on the vertebrate paleobiological record, but there is also sporadic preservation of freshwater mussels in the field area. In the preceding years, a new isotopic technique, carbonate clumped isotope paleothermometry, was being developed. This method allows the determination of carbonate formation temperature in terrestrial environments, as it does not depend on an estimation of the paleowater chemistry. For the work detailed in Chapter 4, I analyzed the freshwater mussels from the Hell Creek area during two trips to Caltech to generate temperature values across the K-Pg boundary (Tobin et al., 2014). Putting field sites in their relative stratigraphic position is complicated in this area due to infrequent rock exposure due to vegetation cover, lateral facies changes in the fluvial and floodplain environment, and land access rights. In the local field area, the K-Pg boundary has been demonstrated to be almost exactly coeval (<10cm difference) with the formational contact between the lower Hell Creek Formation and the overlying Fort Union Formation. High precision GPS measurements of this boundary across the field area allowed us to model the contact as simple plane, and project many of our field sites to the plane to get their stratigraphic positions.

Having analyzed a several samples from stratigraphically irregularly distributed horizons, we were able to generate horizon average temperatures in a stratigraphic series. Sampling was better in the Cretaceous, and we recorded a cooling trend in summer temperatures across the last

~300ka of the Cretaceous before the K-Pg boundary. This trend corresponded temporally to decreases in biodiversity observed in the paleobiological record by Greg Wilson and his graduate students. The temperature record we developed also corresponded very well to leaf based paleotemperature proxies generated a decade earlier. However, comparing the Hell Creek record with the Seymour Island record is complicated by the poor resolution in the Hell Creek area. I explore these issues further in a short Conclusion section.

Chapter 1. Alteration of Micromilled Carbonate $\delta^{18}O$ During Kiel Device Analysis (Tobin et al. 2011)

Thomas S. Tobin, Andrew J. Schauer, Evan Lewarch

Abstract

Isotopic analysis of carbonate material has been greatly facilitated by the development of autosampling devices such as the Kiel III Carbonate Device, allowing rapid automated analysis of small sample sizes. This analysis is facilitated by holding samples and acid at temperatures around 70°C prior to reaction. In most situations this has no measurable effect on sample powders on practical timeframes, but, when analyzing exceptionally fine-grained material produced by micromilling, the $\delta^{18}O$ of both aragonite and calcite is altered by -0.1‰/day. Laboratories that use this technique should thoroughly test and correct for this phenomenon and avoid storing pre-weighed materials within the Kiel device or similar drying oven prior to analysis.

Introduction

The stable isotopic composition of carbonate has been used as record of paleotemperature and other paleoclimatic variables for over fifty years (Epstein et al., 1953). This analysis is typically done by phosphoric acid digestion of solid carbonate material to release H_2O and CO_2 with subsequent purification of CO_2 gas for analysis in an isotope ratio mass spectrometer capable of measuring *m/z* 44-46 (Coplen et al., 1983; McCrea, 1950). Advances in this technique have allowed for analysis of sample sizes as low as 10 µg, with a throughput approaching 100 analyses per day, using an autosampling instrument such as the Kiel III Carbonate device (Thermo Scientific, Bremen, Germany, and hereafter Kiel device). The Kiel device holds samples, standards and acid at above ambient temperatures (Kiel device default is 70°C) to facilitate acid digestion.

As required sample sizes have decreased, numerous studies (e.g. Correa et al., 2010; Dutton et al., 2007; Spötl and Mattey, 2006) have employed computer guided, fine-tipped, high-speed drills, for example the Merchantek Micromill (New Wave, Portland, OR, USA). These tools have allowed high-resolution sampling in fossil and modern shell material, often generating temporal resolution at the monthly, or finer, scale, an impossible task using coarser sampling methods. Previous studies have debated the effect of high speed drilling on aragonite material. Gill et al. (1995) argue for a significant direct effect of drilling on $\delta^{18}O$, though Swart et al. (1996) were concerned about the homogeneity of their material. Foster et al. (2008) later confirmed that high speed drilling has no detectable influence on the measurable isotopic value of the aragonite. While micromilling likely does not induce direct alteration of carbonate material, we present evidence below that it may compromise the stability of $\delta^{18}O$ in both aragonite and calcite when analyzed using a Kiel III Carbonate Device.

Methods

Aragonite and calcite, confirmed by X-Ray Diffraction, was sampled via two methods, crushing with mortar and pestle (hereafter crushed), and drilling with a fine-tipped, high-speed Merchantek Micromill drill (hereafter micromilled). The drill was set to 50% speed (approximately 18,500 rpm). Aragonite was derived from a Late Cretaceous molluscan shell which was crushed and sieved through a set of standard sized sieves, generating a sub-32μm fraction. Crushed and micromilled samples from the same shell were homogenized and then weighed (0.049 ± 0.017mg:1σ) and interspersed into two full 46-analysis, 20-hour runs for analysis in a Kiel device attached to a Delta Plus Isotope Ratio Mass Spectrometer (Thermo Finnigan, Bremen, Germany). The first run was put directly into the carousel for immediate analysis while the second run sat in a sample tray within the Kiel device oven. Samples were interspersed within a run with internal lab standards calibrated to NBS-18 (-3.01‰ VPBD) (IAEA, Vienna, Austria) and NBS-19 (-2.20‰

VPDB) for $\delta^{18}O$ and NBS-19 (+1.95‰ VPBD) and LSVEC (-46.6‰ VPBD) for $\delta^{13}C$ (NIST, Gaithersburg, MD, USA). Internal lab standards are pure calcite, and experience a different oxygen isotope fractionation than aragonite as demonstrated by Kim et al. (2007b). Aragonite $\delta^{18}O$ values were therefore corrected for this fractionation, adjusted to 70 °C. This procedure was repeated with a crushed internal lab marble calcite standard and a micromilled Late Cretaceous molluscan shell preparation. In addition to focused testing as outlined above, a variety of aragonite materials were run as duplicates, one placed at the beginning and one placed at the end of a 46-analysis, 20-hour run, over a period of eight months to determine whether any alteration was a product of seasonal variations in humidity or other factors.

The micromilled and the smallest crushed size fractions of aragonite were also examined at high magnification to assess grain size as sieves were unavailable to provide the size details in the sub-32μm range (Fig. 1.1). Grains were sonicated on non-contaminating weighing paper (Fisher Scientific, Hampton, NH, USA) for five seconds to disperse clumps, then pressed onto an adhesive carbon stub and carbon coated for analysis and imaged using a JEOL 733 electron microprobe equipped with an Everhart-Thornley secondary electron detector (JEOL USA, Peadbody, MA, USA) and the Geller dPict imaging system (Geller MicroÅnalytical Laboratory, Inc., Topsfield, MA, USA). Size measurements on each size fraction were performed by randomly selecting pixels via a random number generator, and if a grain was selected, its longest visible dimension was measured, as was the widest distance perpendicular to the long axis.

Results

The mean (±1 σ) size of micromilled aragonite is 13±6 x 11±5μm (Fig. 1.1). Fig. 1.1 (c) summarizes measurement statistics for the long and perpendicular axes of the micromilled and crushed (<32μm) size fractions examined with the microprobe. A Welch's t-test confirms, at greater

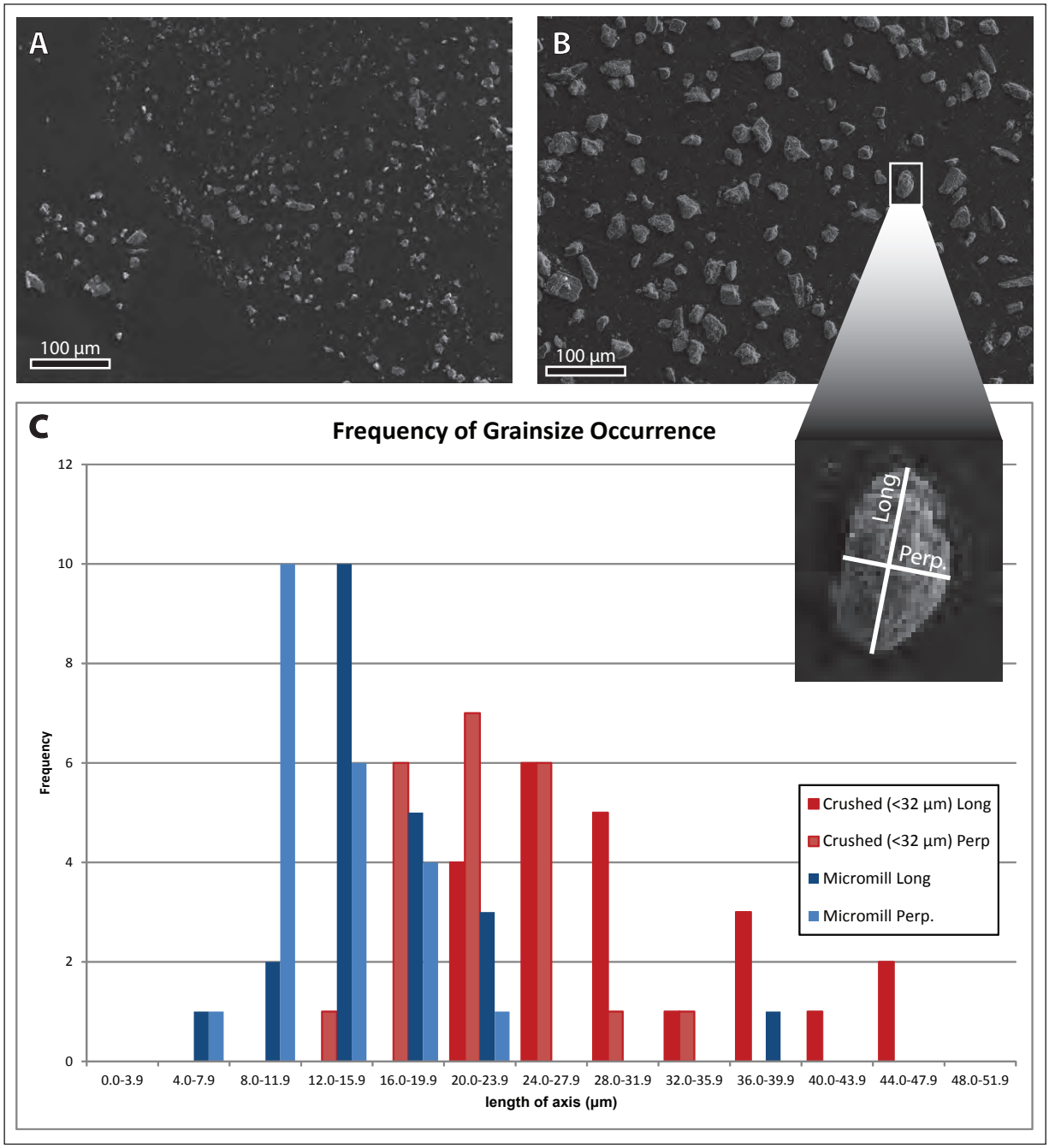

Figure 1.1. Representative scanning electron micrographs of the micromilled aragonite (A) and (<32µm) crushed aragonite size fraction (B) with a histogram of the distribution of long and perpendicular axes lengths(C).

than 99.999% likelihood, the visual evidence from the micrographs and histogram that the two size fractions are significantly different.

An 'accepted' isotopic value (‰) for each different preparation and mineralogy was calculated by taking the mean of the first three measurements (shortest time spent in Kiel device) from each sample group. Each subsequent value was subtracted from this accepted value to determine the amount of change due to alteration. Fig. 1.2 shows the pattern of alteration in $\delta^{18}O$ with total time spent in the Kiel device at 70°C. Micromilled aragonite (Fig. 1.2a) and calcite (Fig. 1.2b) demonstrate a significant trend toward more negative values in $\delta^{18}O$ with longer exposure time: -0.12±0.03 ‰/day for aragonite ($p<0.001$) and -0.10±0.02 ‰/day for calcite ($p<0.001$). This trend is not present in either of the crushed sample size fractions or in the $\delta^{13}C$ of any sample (data not shown). In some cases the best-fit line intercept is non-zero, as would be initially anticipated for unaltered samples. The calculated intercept is an artifact of the assigned 'accepted' value for each sample group, a value that does not affect the slope that describes the rate of alteration. Additionally, data collected during long-term analysis had a consistent trend with the short-term experiment (-0.15±0.03 ‰/day, $p<0.001$). Data are available is Appendix 1.

Discussion

The $\delta^{18}O$ of micromilled carbonate is detectably altered (-0.1‰/day) over a 24 hour period when stored at 70°C. Only micromilled carbonate, with grain size 13 x 11 μm, showed alteration in isotopic values, and only in $\delta^{18}O$, while carbonate above 27 x 19 μm grain size, did not show alteration. The authors attribute the alteration to exchange with atmospheric water facilitated by the high temperature inside the Kiel device. Exchange with gaseous CO_2 may also occur, though the lack of alteration in $\delta^{13}C$ values suggests this is a relatively minor factor. This alteration likely occurs in every sample and standard, but only affects the surficial layer, and consequently, only has a measurable isotopic effect on very small grain sizes with high surface area to volume ratios. This

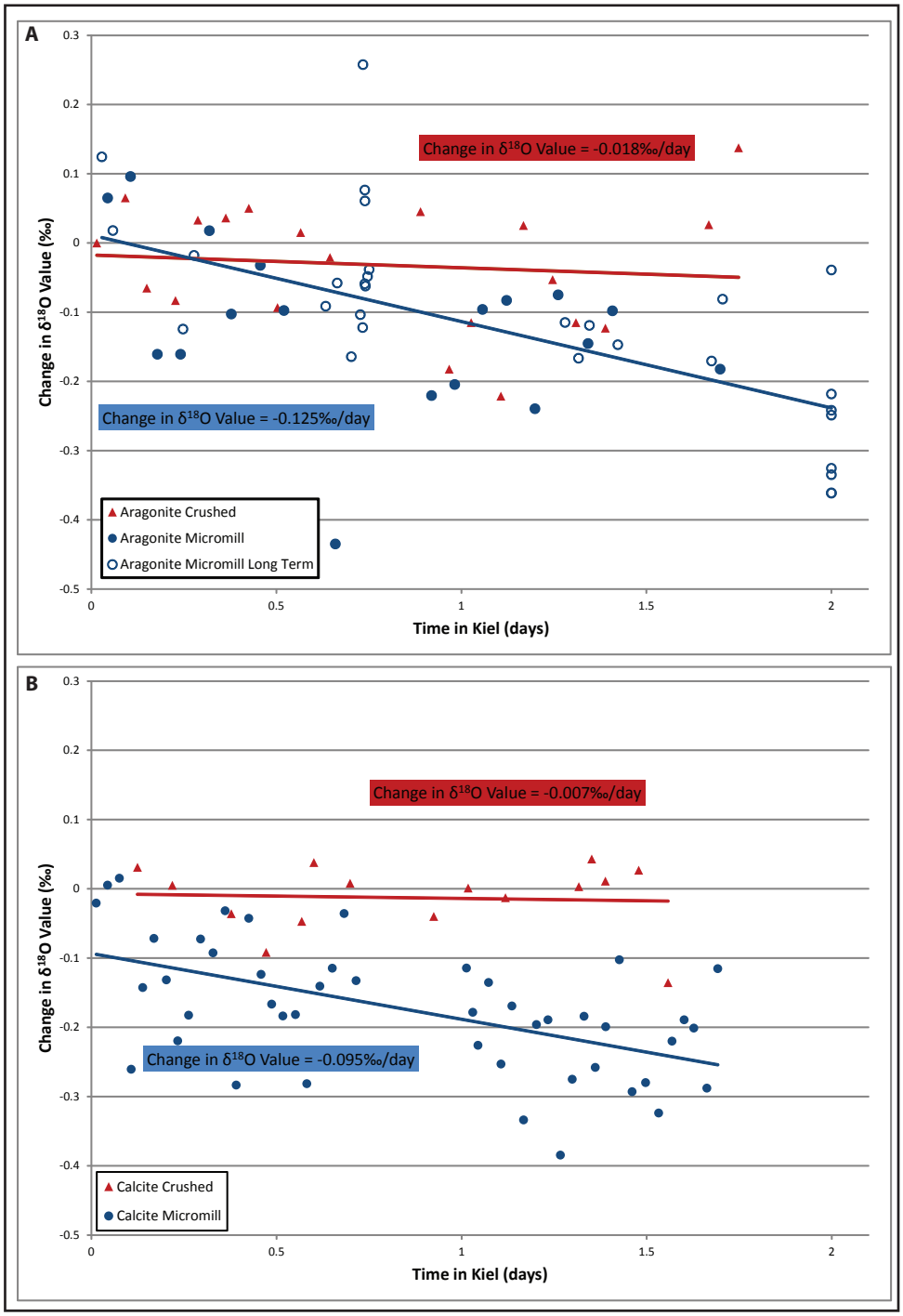

Figure 1.2. Alteration of δ18O for crushed (triangles) and micromilled (circles) size fractions for aragonite (A) and calcite (B). Open symbols are data generated over a longer (months) time frame. The slope for micromilled data in 2a is generated using all micromilled data, including the long term analyses. Data presented in supplemental information (Table 1).

effect is just measurable over the course of a single day run, as regularly reported precision for $\delta^{18}O$ in Kiel device systems is ±0.1‰, suggesting a correction factor should be applied to micromilled, or similarly prepared, carbonate samples based on total time spent in the Kiel device. Ideally, standards of similar grain size would be run in tandem with micromilled samples. Due to the limitations of available sieves creating a sufficiently small grain size by conventional crushing and sieving might be problematic. The practice of placing pre-weighed samples inside the Kiel device or similar low-temperature oven for storage or drying should be avoided. The authors recommend storing pre-weighed samples in a room temperature desiccator, optionally with soda lime to scrub CO_2 (Friedman et al., 1982). Furthermore, similar alteration tests should be performed for other carbonate processing procedures.

Acknowledgements

The authors would like to thank NSF Grant 0739432 that in part funded lab work and was the source of some fossil shell material. Matthieu Carre similarly provided funding as well as samples of modern shell material and critical comments. Thanks also to Kelly Hillbun for assistance in the laboratory and Eric Steig for valuable commentary. In addition, the authors would like to thank two anonymous reviewers for constructive reviews.

Chapter 2. Carbon isotope ($\delta^{13}C$) discrepancies between Late Cretaceous ammonites and benthic mollusks from Antarctica

Thomas S. Tobin, Peter D. Ward

Abstract

Ammonites are one of the most common fossils from the Mesozoic, but there is little consensus on their mode of life. Isotopic studies have been used to reconstruct their preferred water temperature from $\delta^{18}O$ measurements, but $\delta^{13}C$ values have more ambiguous interpretations. Previous studies have recorded population differences in $\delta^{13}C$ between ammonite and benthic organisms without explaining the cause in detail. Here we examine a molluscan community from Seymour Island, Antarctica and also find a carbon isotope offset between ammonites and other benthic mollusks. The most likely cause of this anomaly is an increased metabolic carbon contribution to ammonite shell material when compared with other mollusks, but we cannot rule out the possibility of a methane seep contribution. Increased respired CO_2 production could be generated by a more active lifestyle and increased energy demands, which may have increased the susceptibility of ammonites to the end Cretaceous mass extinction.

Introduction

Ammonites, biostratigraphically and ecologically important shelled cephalopods, were one of the most notable casualties of the Cretaceous – Paleogene (K-Pg) mass extinction (66 Ma). Their complete and rapid extinction was one of the most important demonstrations of the rapidity of the K-Pg mass extinction event (Marshall and Ward, 1996; Marshall, 1995). While most other major molluscan groups survived the extinction, albeit with some losses, all ammonites went extinct rapidly at the end of the Cretaceous. While evidence for an asteroid impact at the K-Pg boundary remains overwhelming more than three decades after it was first proposed (Alvarez et al., 1980),

the specific aspects of this catastrophe responsible for directly killing organisms (Archibald et al., 2010; Schulte et al., 2010), and the potential contributions of other events like Deccan Traps flood volcanism (Mitchell et al., 2012; Tobin et al., 2014, 2012), are still being debated. Any kill mechanism must explain the preferential extinction of ammonites compared to other molluscan groups, and this still unresolved question provides a compelling driver for continued research into their paleoecology.

It is not clear that there are any good modern analogs for ammonites, as the only nektonic or demersal carbonate secreting mollusks today are *Sepia, Spirula,* and *Nautilus*. Stable isotope and morphological evidence has been used to argue that ammonites lived in relatively shallow waters in a demersal, or nektobenthic, lifestyle (e.g. Moriya et al., 2003; Westermann, 1996) though recent work has argued for more complexity, both taxonomically between ammonite species and ontogenetically (Ritterbush and Bottjer, 2012; Ritterbush et al., 2014). *Nautilus* (Taylor and Ward, 1983) and *Spirula* (Warnke et al., 2010) both prefer deeper water and a more pelagic lifestyle, though they may come to the shallow waters at night to feed. Other morphological evidence also raises questions about *Nautilus* as an ammonite analog (Jacobs and Landman, 1993) as does the internal nature of the *Spirula* and *Sepia* shells.

Much of the evidence for lifestyle patterns of ammonites has come from stable isotopic analysis of shell carbonate. In most of these analyses, both $\delta^{18}O$ and $\delta^{13}C$ values are generated, but many studies focus primarily on the $\delta^{18}O$ values as these can generally be used to reconstruct paleotemperature (Kim et al., 2007b) with reasonable accuracy. Less well studied are the $\delta^{13}C$ values, which have more ambiguous interpretations, and few attempts have been made to explicitly compare and explain the $\delta^{13}C$ of ammonites relative to contemporary mollusks. Analysis of $\delta^{13}C$ from modern *Nautilus* has encountered mixed results; some studies (Crocker et al., 1985; Taylor and Ward, 1983) found no significant changes in $\delta^{13}C$ over the lifespan of the organism, while

others have recorded a decreasing pattern (Auclair et al., 2004). In both cases $\delta^{13}C$ values were at, or very near, equilibrium values expected from seawater. In contrast, $\delta^{13}C$ values from modern *Spirula* record $\delta^{13}C$ values out of equilibrium with seawater, a phenomenon attributed to the internal nature of their shell, and which may increase the incorporation of respired CO_2 into their shell (Price et al., 2009). Ontogenetic series for *Spirula* are also inconsistent, showing both increasing and decreasing patterns, sometimes in the same shell (Price et al., 2009; Warnke et al., 2010). *Sepia* also show a 'vital effect' on their $\delta^{13}C$ values, similar to that in *Spirula*, and probably from the same cause – the internal nature of the shell (Rexfort and Mutterlose, 2006).

Many studies that have investigated fossil molluscan populations found that ammonites have lower $\delta^{13}C$ values than benthic mollusks, including in the Jurassic of England and Poland (Malchus and Steuber, 2002), the Cretaceous of the United States (da Silva, 2006; He et al., 2005) and Canadian (Forester et al., 1977) Western Interior, the Cretaceous of Australia (Henderson and Price, 2012). Belemnites, another extinct fossil cephalopod group, have also shown a $\delta^{13}C$ offset in the same direction (Alberti et al., 2012; Wierzbowski and Joachimski, 2007; Wierzbowski, 2002). Wierzbowski and Joachimski (2007) analyzed a wider variety of taxonomic groups and find that ammonites and belemnites have more negative $\delta^{13}C$ values than oysters, but similar $\delta^{13}C$ values to trigonid bivalves. In these studies, if the $\delta^{13}C$ offset is commented on, it is generally briefly attributed to a vital effect or diagenesis, as most studies are focused on interpretation of the $\delta^{18}O$ values for temperature.

Landman et al. (2012) examined a molluscan population from a Campanian-aged deposit they convincingly argued is a methane seep environment based on overall morphology and very light $\delta^{13}C$ values (-40 to -45‰) of matrix carbonate. Mollusk $\delta^{13}C$ values were depleted relative to mollusks not at the seep, a discrepancy they attribute to the incorporation of relatively light methane carbon influencing the dissolved inorganic carbon (DIC) pool around the seep

environment. Within the seep samples the $\delta^{13}C$ of ammonites is lower than those of the benthic mollusks (see Conclusion for more). Here we examine another Late Cretaceous (Maastrichtian) molluscan community from Seymour Island, off the Antarctic Peninsula. We examine multiple stratigraphic horizons from two fossil collections and find consistently depleted $\delta^{13}C$ values for ammonites when compared with benthic mollusks. We explore some hypotheses, but the most likely explanation is that this phenomenon is a vital effect caused by the incorporation of a significant percentage of respired, or metabolic, carbon into the shell.

Geologic Setting

Seymour Island is located on the northeastern end of the Antarctic Peninsula (Fig. 2.1), and has continuous sedimentation of Maastrichtian to Danian age, including a complete Cretaceous – Paleogene (K-Pg) boundary section. The sediments comprise the uppermost Marambio group, and an unconformity separates them from overlying Eocene Seymour Island Group (see Olivero, 2012; Olivero et al., 2007 for more information). All the samples were collected from the Lopez de Bertodano Formation (LBF), which contains the K-Pg interval and is interpreted as continental shelf deposition (Macellari, 1988) during the uplift of the Antarctic Peninsula. Since deposition, the area has seen little change in its paleogeographic location or paleolatitude (~62 °S) since deposition (Tobin et al., 2012; Torsvik et al., 2008). Additionally there has been little tectonic influence, with only minor homoclinal tilting (5° – 10°) and minimal burial history.

The LBF is well exposed during austral summer when not covered in snow, and it is highly fossiliferous, particularly in the uppermost "molluscan units" as defined by Macellari (1988, 1986). Fossils are not only abundant, but are very well preserved, both physically in their three-dimensional structure, but also chemically, in the persistence of primary mineralogy, principally aragonite, with a small number of taxa precipitating calcite. Two similar but separate collections of fossils were analyzed for $\delta^{13}C$ and $\delta^{18}O$. The first group (hereafter: 'UW collection') was collected by

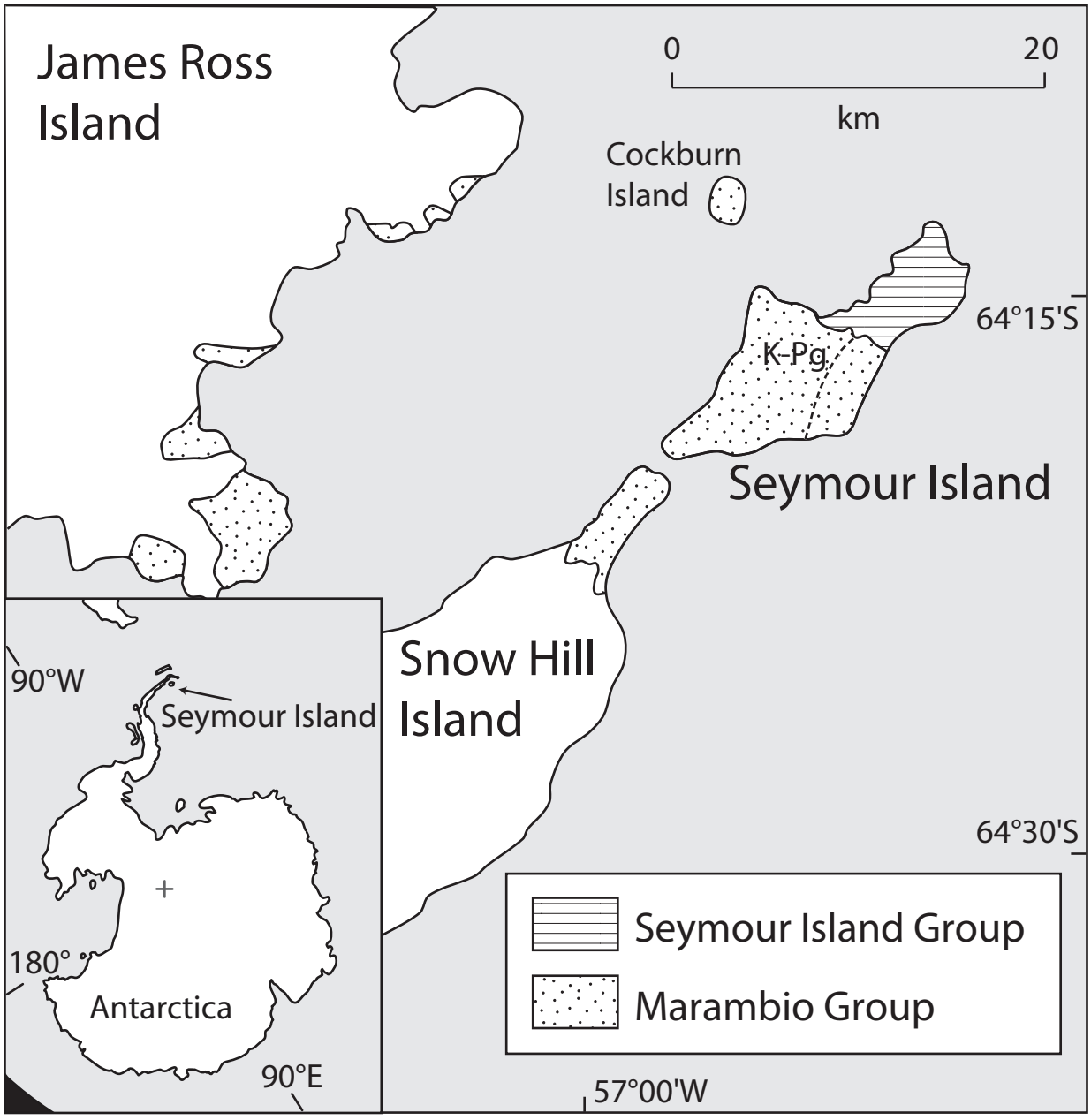

Figure 2.1. Map of field area, samples for this study were collected from the uppermost Marambio Group on Seymour Island, which contains the K-Pg boundary. Inset shows location of Seymour Island in relation to Antarctica and the southernmost South America.

the authors and assisting field workers during field seasons between 2008 and 2011. The second group (hereafter: 'PRI collection') was collected by expeditions lead by Zinsmeister (e.g. Zinsmeister, 1998; Zinsmeister et al., 1989) over many field seasons during the 1980s and 1990s, and is currently housed at the Paleontological Research Institute (PRI). We sampled and analyzed the PRI collection in 2012 and 2013.

The UW collection was collected for the purposes of generating an isotopic record across the K-Pg boundary (Tobin et al., 2012) and as such was collected with attention to stratigraphic detail, but without a focused attempt to acquire large numbers of specimens at any stratigraphic level. The $\delta^{18}O$ values for this collection were explored in Tobin et al. (2012) to reconstruct paleotemperature, but the $\delta^{13}C$ values were not, and required further investigation. The PRI collection has some stratigraphic information, though with larger uncertainties in their relative positions (Zinsmeister, 2001), but is much larger in terms of numbers, and has many localities with a variety of taxa represented. These collections cannot be placed in a 1:1 stratigraphic correspondence with each other, as the K-Pg boundary horizon is the only suitable correlative bed. The collections must be treated separately, but that is not a major drawback of this study.

Methods

Sample processing for the collections differed due to restrictions necessary for the curated PRI museum collection. Fossil shells from the UW collection were cut, polished, and drilled using a computer controlled Merchantek micromill to generate powder for isotopic analysis. This processed allowed access to the interior of the fossil shell, which is less likely to experience diagenetic alteration. Samples analyzed for the UW collection were also checked for diagenesis using cold cathodoluminescence microscopy, trace element concentrations, and X-Ray diffraction to assess primary mineralogy (see further details in Tobin et al. 2012). Some of the earliest samples from the UW collection were prepared using tool tip made of carbide. While there was no variance

in these values with relation to $\delta^{18}O$, these samples were often significant outliers in $\delta^{13}C$ space, and all analyses made using this tool were removed from this analysis. Fossils from the PRI collection could not be subjected to the same destructive cutting process, so small pieces of shell were either pried off the shell for later powdering, or drilled using a Dremel tool to powder the shell directly from the fossil. In both cases shells were not sampled near cracks or near any location where iridescent aragonite was not observed, and before drilling the very outermost layer of shell was powdered and removed to avoid any potential surficial diagenetic effects.

Sample powders were then weighed and analyzed along with internal lab standards calibrated to NBS-18 and NBS-19 for $\delta^{18}O$ and NBS-19 and LSVEC for $\delta^{13}C$. Samples were reacted at 70 °C with anhydrous phosphoric acid at 70 °C in a Kiel III Carbonate Device attached to Delta Plus isotope ratio mass spectrometer at the IsoLab at the University of Washington. Any sample powder generated with a drill was corrected for time sensitive isotopic reset in the Kiel Device (Tobin et al., 2011). In most cases multiple analyses were completed on each powder aliquot and averaged together for mean shell $\delta^{13}C$ and $\delta^{18}O$ values.

Results

Diagenesis- The PRI collection was unable to be tested extensively for diagenesis, though every effort was made to avoid any fossils with signs of potential diagenesis (see Methods). However, previous work on the UW collection demonstrated that these measures were sufficient to generate a reliable data set (Tobin et al., 2012). Diagenesis is more likely to affect the $\delta^{18}O$ composition of carbonate material (Banner and Hanson, 1990), and here we demonstrate the PRI collection data set records essentially the same stratigraphic $\delta^{18}O$ pattern as the UW collection (Fig. 2.2) though the two records can only be reliably correlated using the K-Pg boundary horizon. We conclude that it given the correspondence of the $\delta^{18}O$ records, it is unlikely that the $\delta^{13}C$ of the PRI collection fossils has been altered. Similarly, there is no strong correlation between individual shell $\delta^{13}C$ and

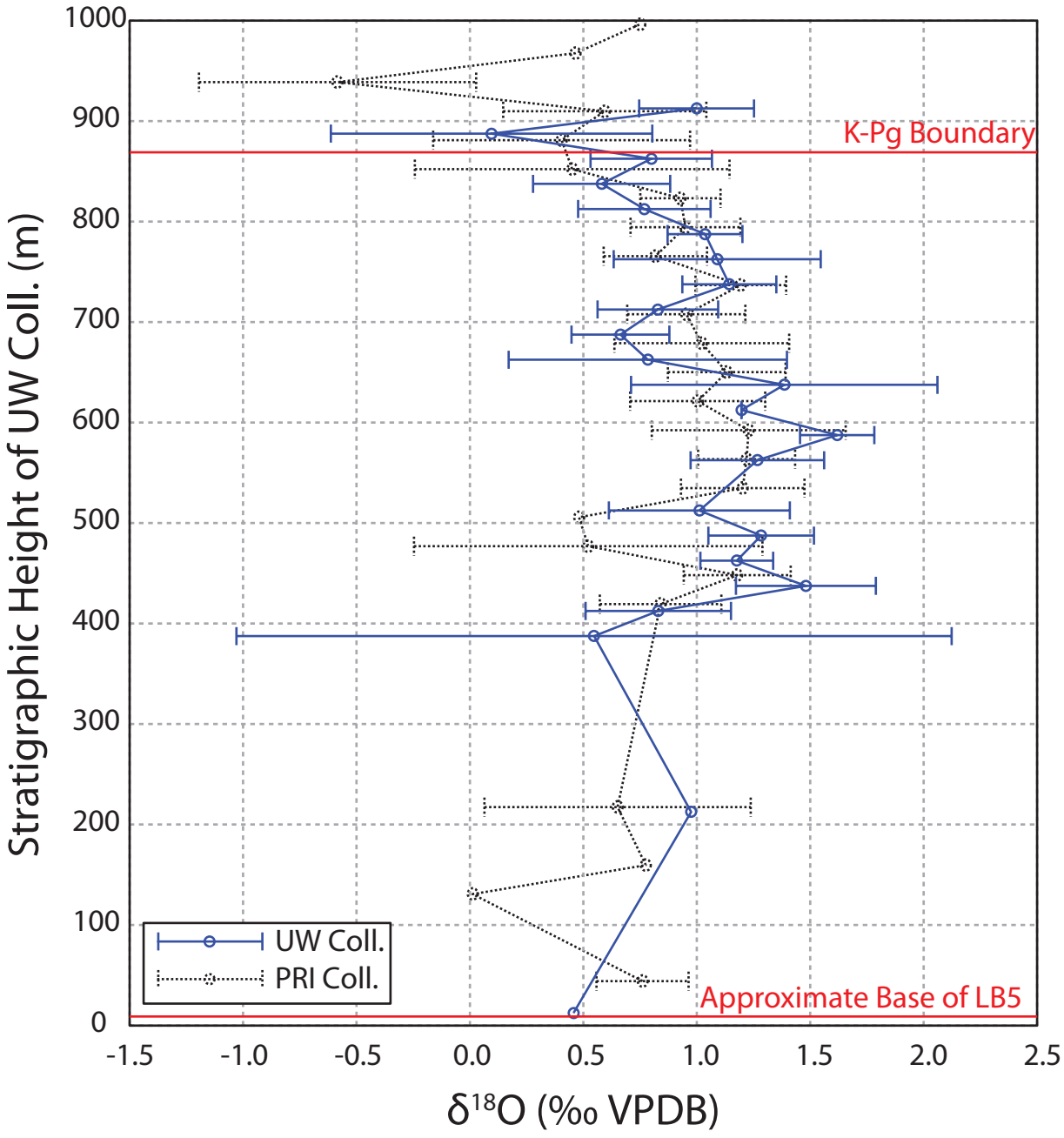

Figure 2.2. Oxygen isotopic ($\delta^{18}O$) records for the UW and PRI sample collections, stratigraphically correlated, and linearly stretched, using the K-Pg boundary and the base of informal unit 5 from Macellari (1988). Apart from the two tie points, the stratigraphic relationship between the two collections has unquantifiable uncertainty. Overall good correspondence suggests that there are no diagenetic differences between the two collections.

$\delta^{18}O$ values in either the entire PRI or UW data set, or when broken down into ammonite or benthic data sets (R^2 values between 0.03 and 0.22), which adds circumstantial evidence to support a lack of diagenesis, where diagenesis would be represented by covariance between $\delta^{13}C$ and $\delta^{18}O$.

Stratigraphic $\delta^{13}C$ and $\delta^{18}O$ comparisons- The differences in $\delta^{13}C$ are most apparent when plotted in their stratigraphic context, though differences are apparent in $\delta^{18}O$-$\delta^{13}C$ crossplots (Fig. 2.3). Because ocean water $\delta^{13}C$ values (and local environmental factors) can change through time, averaging $\delta^{13}C$ values across a long stratigraphic range will incorporate these changes as "noise" in an attempt to discern $\delta^{13}C$ differences between ammonites and their contemporary benthic mollusks. In an effort to make the stratigraphic patterns clear, $\delta^{13}C$ were plotted in their stratigraphic context (Fig. 2.4 (top), and horizons from which both ammonite and benthic fauna were recovered are separated out and plotted (Fig. 2.4 (bottom)). A horizon was defined in the PRI collection as a single collecting locality. In the UW collection, samples were collected along a stratigraphic section with their stratigraphic position given in meters. Fossils were considered to be in a single horizon when they were within one meter of each other stratigraphically. Average ammonite and benthic molluscan $\delta^{13}C$ values were calculated at each horizon, and their differences (defined here as $\Delta\delta^{13}C_{ben\text{-}amm}$) are plotted in Figure 2.4 and Table 2.1. In every case, the ammonite mean $\delta^{13}C$ value is lower than the mean benthic $\delta^{13}C$ values, though there is substantial variation in magnitude. At some horizons, there is only one representative ammonite or benthic mollusk, which is reflected in Figure 2.4 by the point overlying the benthic or nektic mean. The average $\Delta\delta^{13}C_{ben\text{-}amm}$ for the selected horizons is 4.7‰ for the PRI collection, 2.7‰ for the UW collection and 3.8‰ for the combined data set.

Separating the $\delta^{13}C$ values for the ammonites and benthic mollusks also reveals the previously unrecognized $\delta^{13}C$ anomaly at the K-Pg boundary. A negative ~3‰ excursion has long been observed globally at the boundary (e.g. Molina et al., 2006; Schulte et al., 2010). This pattern is

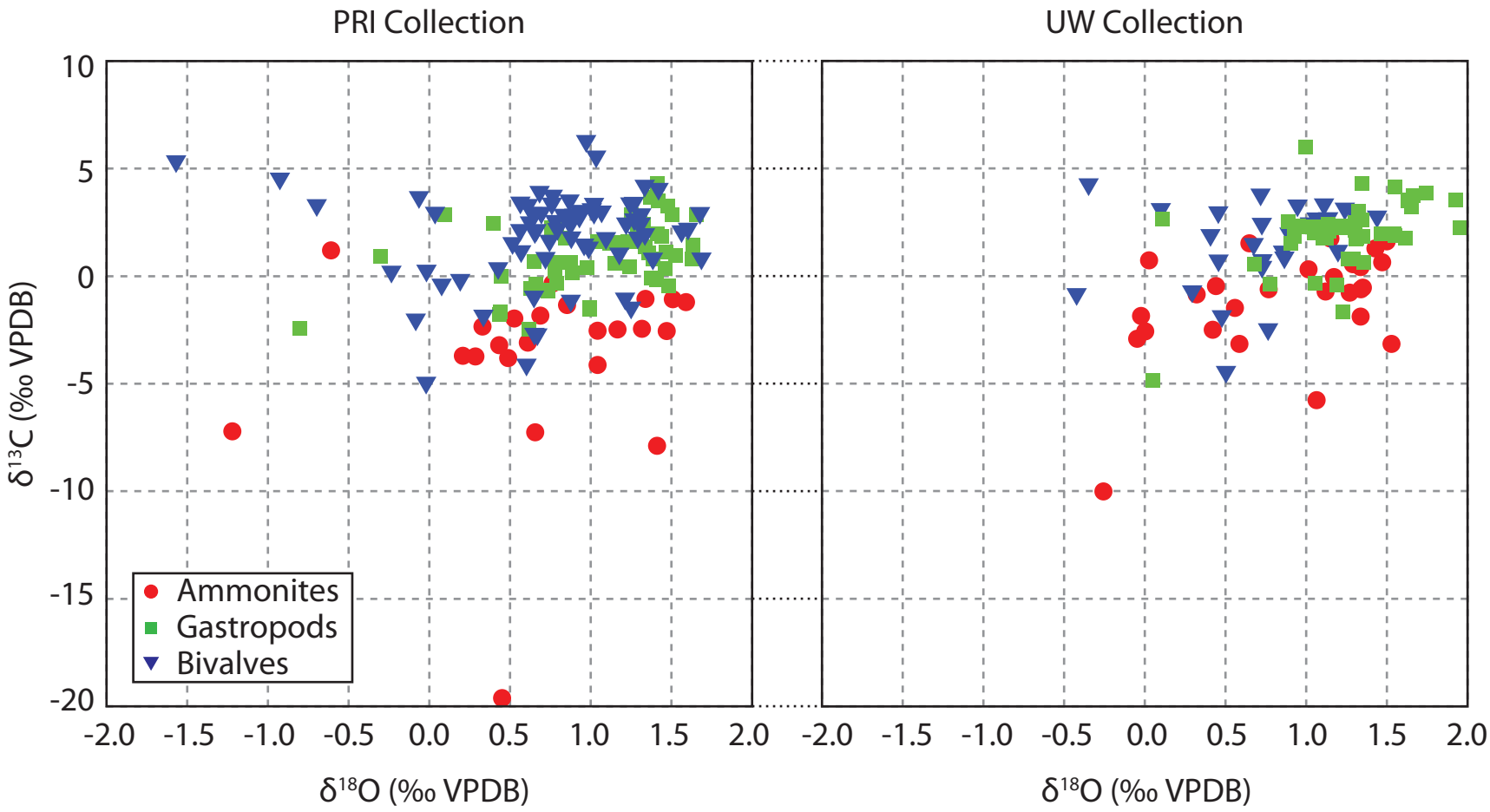

Figure 2.3. Crossplots of $\delta^{13}C$ and $\delta^{18}O$ for both the UW and PRI collections, separated by taxonomic group. No significant or strong correlations were found between $\delta^{13}C$ and $\delta^{18}O$ for any subset or the total data set.

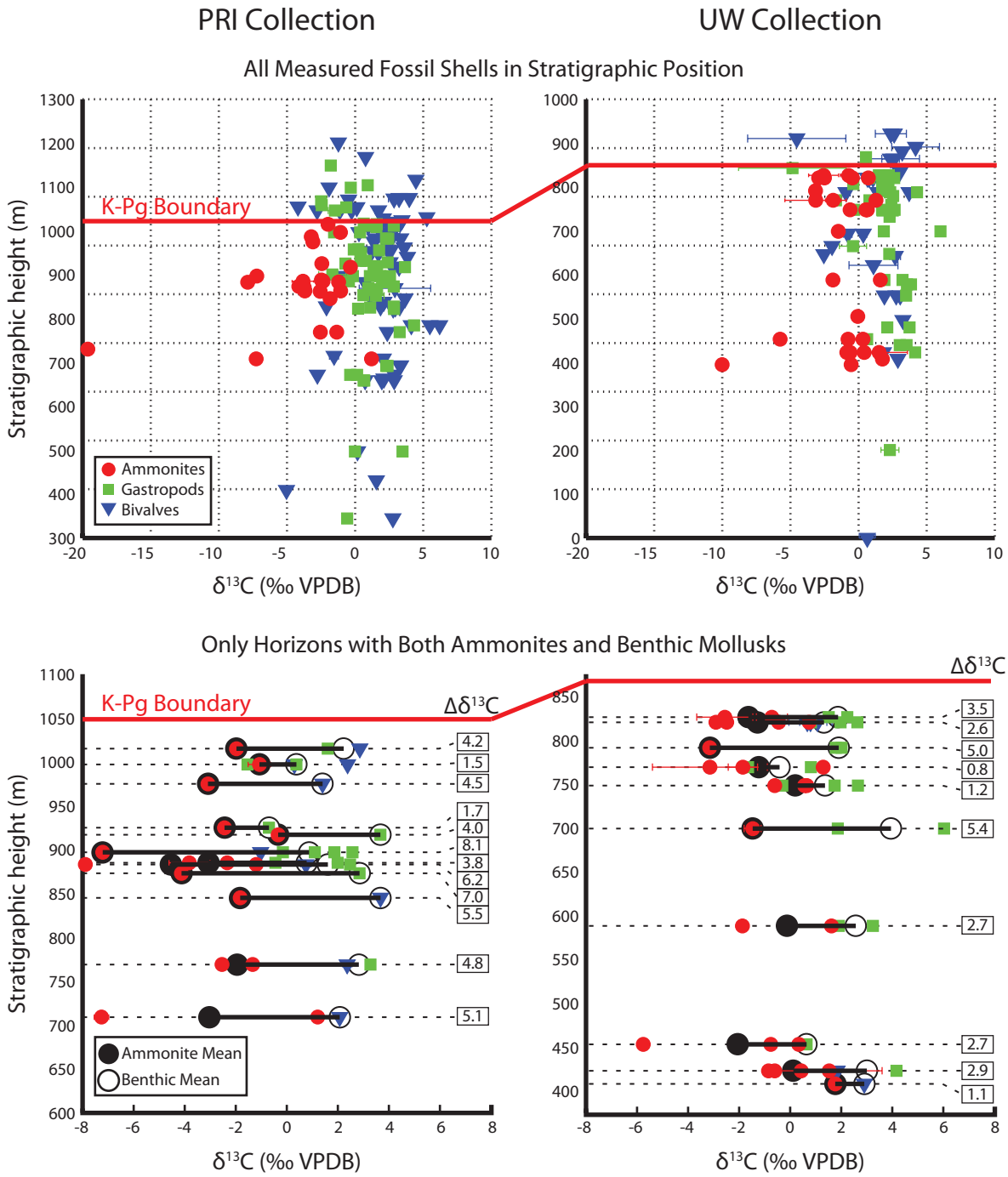

Figure 2.4. (Top) Carbon isotopic ($\delta^{13}C$) records in stratigraphic context, separated by taxonomic group, for both UW and PRI collections. Average ammonite and benthic populations for each collection are statistically distinct. (Bottom) Average $\delta^{13}C$ values for horizons (see text for definition) with both ammonites and benthic mollusks present. Every horizon has lower $\delta^{13}C$ for ammonites than benthic mollusks.

Table 2.1

	Amm. $\delta^{13}C$ (‰)	n	Ben. $\delta^{13}C$ (‰)	n	$\Delta\delta^{13}C_{ben\text{-}amm}$ (‰)	Strat (m)	Benthic R = 10% DIC $\delta^{13}C$ (‰)	Benthic R = 10% Amm. C_{meta} (%)	Benthic R = 0% DIC $\delta^{13}C$ (‰)	Benthic R = 0% Amm. C_{meta} (%)
PRI Collection Individual Horizons	-3.0	2	2.1	1	5.1	709	1.4	39	-0.6	31
	-1.9	2	2.8	2	4.8	769	2.2	36	0.1	28
	-1.8	1	3.7	1	5.5	845	3.2	38	1.0	31
	-4.1	1	2.8	1	7.0	873	2.3	47	0.1	41
	-4.5	4	1.6	2	6.2	883	0.9	45	-1.1	39
	-3.1	1	0.8	2	3.8	885	0.0	34	-1.9	26
	-7.2	1	0.9	4	8.1	897	0.1	58	-1.8	53
	-0.3	1	3.7	1	4.0	917	3.2	31	1.0	22
	-2.4	1	-0.7	1	1.7	925	-1.7	23	-3.4	13
	-3.1	1	1.4	1	4.5	975	0.7	37	-1.3	29
	-1.1	1	0.4	4	1.5	997	-0.5	20	-2.3	10
	-2.0	1	2.2	2	4.2	1015	1.6	34	-0.5	25
Average=	**-2.9**	**17**	**1.8**	**22**	**4.7**	-	**1.1**	**36.8**	**-0.9**	**28.9**
UW Collection Individual Horizons	1.8	1	2.9	1	1.1	408	2.3	17	0.2	7
	0.1	4	3.0	2	2.9	423	2.4	26	0.3	17
	-2.1	3	0.6	1	2.7	453	-0.2	27	-2.1	18
	-0.1	2	2.6	2	2.7	588	2.0	25	-0.1	16
	-1.5	1	3.9	2	5.4	699	3.5	37	1.2	30
	0.2	2	1.4	3	1.2	748	0.6	18	-1.3	7
	-1.2	3	-0.4	2	0.8	769	-1.4	16	-3.1	6
	-3.0	1	1.9	2	4.9	791	1.3	38	-0.8	30
	-1.3	4	1.3	5	2.6	820	0.5	26	-1.4	16
	-0.8	2	2.1	2	2.9	826	1.4	27	-0.6	18
Average=	**-0.8**	**23**	**1.9**	**22**	**2.7**	-	**1.2**	**25.8**	**-0.8**	**16.5**
UW & PRI Horizons=	**-1.9**	**40**	**1.9**	**44**	**3.8**	-	**1.2**	**31.8**	**-0.8**	**23.2**

not observed in our data if ammonite $\delta^{13}C$ values are included, as they bias average Cretaceous $\delta^{13}C$ values in a negative direction. The boundary negative excursion is disguised by their disappearance. Figure 4.5 shows the benthic $\delta^{13}C$ record for the PRI collection with a running average showing a negative 3‰ excursion. The seven point running average was calculated using horizon averages of benthic values, weighted by the number of samples at each horizon; excursion presence is insensitive to the weighting or the length of the running average.

Discussion

The stable isotopic data show that ammonites have comparable $\delta^{18}O$ values but lower $\delta^{13}C$ values than benthic mollusks. With similar $\delta^{18}O$ values it is most likely that these organisms are living in water of similar temperature, if not living in precisely the same environment. Three hypotheses, outlined below, are capable of explaining this offset under the assumption that mollusks secrete their shell under equilibrium conditions. Two are based on different living environments, specifically ammonites exploring $\delta^{13}C$ water depth gradients or methane seep localities, while the third involves the incorporation of metabolic, or respired, CO_2 into the extra-palial fluid (EPF) used to generate shell material. Kinetic isotopic effects could plausibly explain differences in $\Delta\delta^{13}C_{ben\text{-}amm}$, but would usually influence $\delta^{18}O$ values as well, which is not present in our data sets (McConnaughey, 1989a, 1989b). Most mollusks are thought to precipitate shell in equilibrium with surrounding water, though it may be more accurate to say they secrete their shell in equilibrium with the EPF, which may be significantly altered from seawater by respired CO_2 (Gillikin et al., 2007). It is unlikely that the lower $\delta^{13}C$ values are a consequence of diagenesis, as the $\delta^{18}O$ values are much more prone to alteration due to the relative amounts of carbon and oxygen in diagenetic fluids (Banner and Hanson, 1990).

Environmental differences- In the modern ocean there are vertical gradients in dissolved inorganic carbon (DIC) $\delta^{13}C$ where the surface can range up to 3‰ higher than at ~500 meters depth, though

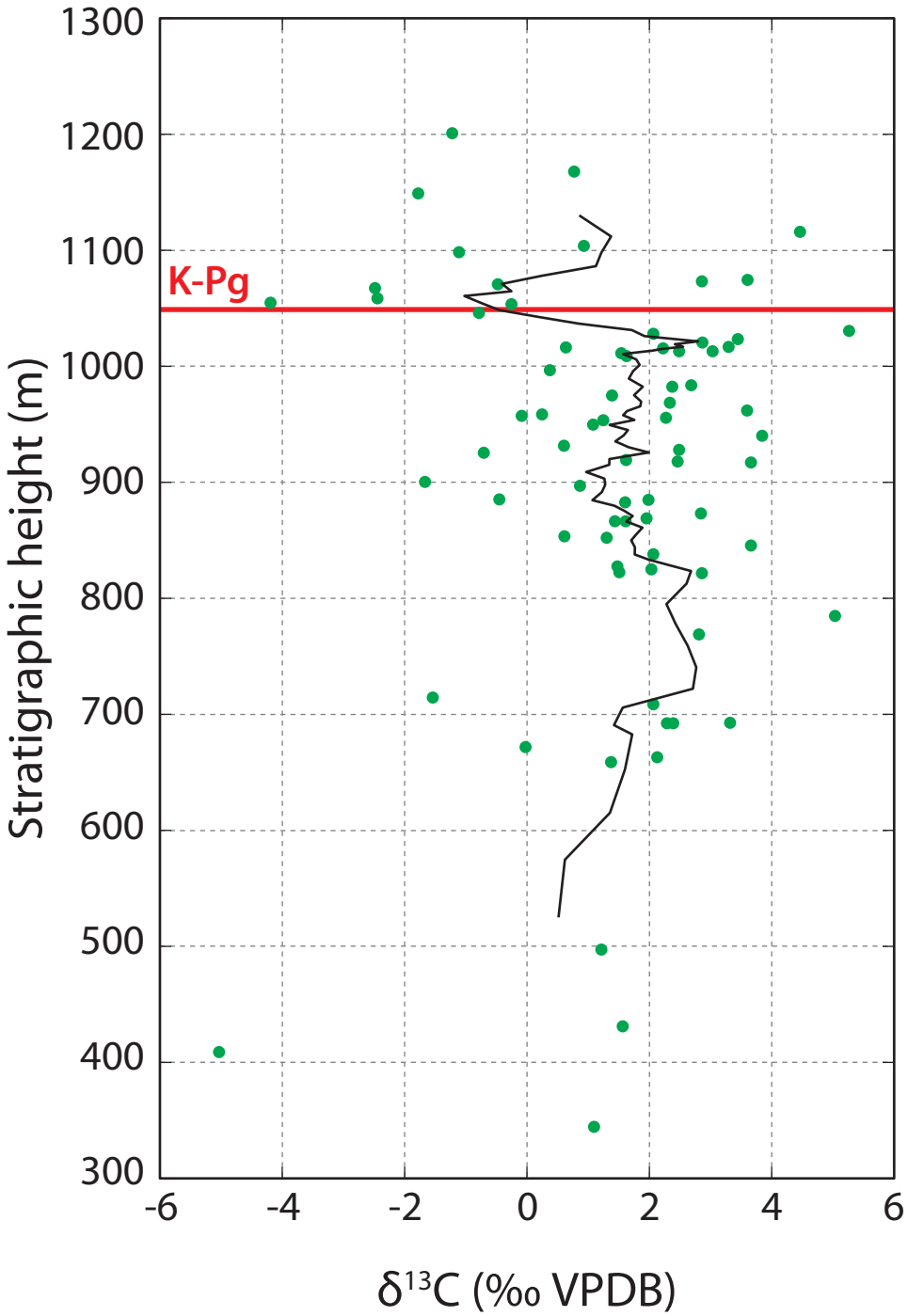

Figure ç.5. Horizon average $\delta^{13}C$ values for benthic mollusks (points) and 7-point running average (line). Negative ~3‰ excursion is coincident with the K-Pg boundary.

the magnitude of the difference is more commonly less than 2‰ for the last million years (Hodell et al., 2003). Given that the average $\Delta\delta^{13}C_{ben\text{-}amm}$ observed was 3.7‰, it is possible that a greater-than-modern $\delta^{13}C_{DIC}$ gradient existed during the Late Cretaceous in this specific location, but foraminiferal differences in the South Atlantic for the latest Cretaceous record a 2‰ maximum carbon isotope gradient (D'Hondt, 2005). The western interior of North America may have had a higher $\delta^{13}C_{DIC}$ gradient of 3‰ (Fisher and Arthur, 2002) but is likely to have been more stratified. Higher gradients may still exist, and have been recorded in the past, including at the Permo-Triassic boundary (Song et al., 2013). Given the range of $\Delta\delta^{13}C_{ben\text{-}amm}$ values, some of the smaller differences could reasonably be explained by a lower $\delta^{13}C_{DIC}$ ammonite habitat, but the larger differences present a significant challenge to this hypothesis. Additionally, we do not see higher $\delta^{18}O_{shell}$ values in ammonites that would reflect them living in a cooler, deeper environment. In the interest of completeness, it is theoretically possible that ammonites could be living in brackish water heavily influenced by terrestrial runoff, but there is no reliable evidence to date of ammonites living in anything but true marine environments.

Metabolic CO_2- Modern mollusks have occasionally been recorded as incorporating significant amounts of depleted carbon in the form of metabolic CO_2 into their EPF, where it mixes with the DIC pool of the EPF reducing the overall $\delta^{13}C_{shell}$. This effect may occur in most marine mollusks, but if so, it is likely a small contribution, somewhere less than ten percent (McConnaughey and Gillikin, 2008). There are often fluid pathways connecting the EPF with ambient water, reducing the impact of respired CO_2, but in some cases it appears water, and consequently DIC, exchange across these pathways can be reduced or the relative metabolic rate increased (Gillikin et al., 2009, 2005). In this situation the percentage of respired CO_2 contributing to the DIC pool can grow substantially larger than 10%, allowing the low $\delta^{13}C$ of respired CO_2 to significantly reduce $\delta^{13}C_{DIC}$ of the EPF, and consequently the shell material precipitated from it.

If we assume that the high $\Delta\delta^{13}C_{ben\text{-}amm}$ is a consequence of respired CO_2 contribution, it is straightforward to model the percentage contribution of respired CO_2 (C_{meta}) if the $\delta^{13}C_{DIC}$ of ambient seawater is known. A reasonable assumption is to use the $\delta^{13}C_{shell}$ of bivalves and gastropods as a proxy for oceanic $\delta^{13}C_{DIC}$, either by assuming there is no respired CO_2 contribution, or assuming that there is an average 10% contribution of respired CO_2 as McConnaughey and Gillikin (2008) demonstrate may be common for mollusks. Equation 1 below (McConnaughey and Gillikin, 2008; McConnaughey et al., 1997), describes the relationship between these components:

$$C_{metabolic} = \frac{\delta^{13}C_{shell} - \varepsilon_{aragonite} - \delta^{13}C_{DIC}}{\delta^{13}C_{metabolic} - \delta^{13}C_{DIC}}$$

Where $\varepsilon_{aragonite}$ is the $\delta^{13}C$ fractionation between DIC and aragonite (Romanek et al., 1992). The value of $\delta^{13}C_{metabolic}$ in the benthic mollusks can be estimated by examining modern examples, usually between -18‰ and -20‰ (e.g. Gillikin et al., 2007). Modern *Nautilus*, a potential analog for ammonites, has been recorded with a similar value, -17 ± 2‰ (Crocker et al., 1985). Given these values for benthic mollusks, we can solve for $\delta^{13}C_{DIC}$, rearranging equation 1 to equation 2:

$$\delta^{13}C_{DIC} = \frac{\delta^{13}C_{shell} - \varepsilon_{aragonite} - (C_{metabolic} \times \delta^{13}C_{metabolic})}{1 - C_{metabolic}}$$

When C_{meta} is equal to 0, equation 1 simplifies to $\delta^{13}C_{DIC} = \delta^{13}C_{shell} - \varepsilon_{aragonite}$. Estimated $\delta^{13}C_{DIC}$ values using this method are recorded in Table 2.1, for both benthic C_{meta} = 0% and 10% cases. This $\delta^{13}C_{DIC}$ value can be used with equation 1 for ammonites to determine the metabolic carbon contribution necessary to generate the measured $\Delta\delta^{13}C_{ben\text{-}amm}$ at any stratigraphic horizon. Cases where C_{meta} = 0%, instead of 10%, for benthic organisms produce lower estimates of C_{meta} for ammonites.

Calculated values of C_{meta} for ammonites were variable when values for individual horizons were examined (~10-50%, see Table 2.1), but averages were between 17% and 37% for the two collections. Using the averages for all data in both collections ammonite C_{meta} was calculated as

between 24% and 33% for benthic C_{meta} values ranging from 0-10%. All of these ammonite C_{meta} values are within published ranges for vital effects in marine mollusks, suggesting that the contribution of respired carbon to ammonite shell material is a plausible explanation for the discrepancy between ammonites and benthic mollusks. A potential modern analog, *Nautilus*, does not show a significant difference between their $\delta^{13}C_{shell}$ signal and that of other benthic organisms (Crocker et al., 1985; Taylor and Ward, 1983; Zakharov et al., 2006). As described above, modern benthic mollusks have, in some cases, been shown to display substantially negative $\delta^{13}C_{shell}$ values that are attributed to higher C_{meta} contributions. Some modern bivalves have shown a dependence of $\delta^{13}C_{shell}$ on body size or age (Gillikin et al., 2009) which can be explained by some combination of an increased production of metabolic carbon from increased tissue volume and a decrease in mixing between EPF and ambient ocean water. It is possible that ammonites generate greater amounts of respired CO_2 due to increased metabolic activity, possibly due to an active swimming and feeding lifestyle when compared with benthic mollusks. Due to the morphology and sampling restrictions on the ammonites, samples were generally obtained from later in life positions on the shells, in contrast to fossil bivalves, which were sampled towards the earliest life stages (near the umbo). This potential age difference, and the generally larger ammonite body size, could also explain the higher C_{meta} values inferred from the lower $\delta^{13}C_{shell}$. However, ontogenetic stable isotope studies of ammonites have generally not shown decreasing patterns of ontogenetic $\delta^{13}C_{shell}$, and in some cases record an increase in $\delta^{13}C_{shell}$ (Fatherree et al., 1998; Lukeneder et al., 2010).

Methane seep influence- Cold methane seeps bring depleted ($\delta^{13}C$) organic carbon to the ocean floor, which can influence the local DIC pool around the seep. This negative $\delta^{13}C$ source could plausibly explain a depleted ammonite $\delta^{13}C_{shell}$. Landman et al. (2012) observed that ammonite shells have been found in direct association with methane seep environments. Geologic and paleobiological data both support the interpretation of their environment as a cold methane seep, as does the depleted carbon signal from the inorganic carbonates. Lower $\delta^{13}C_{shell}$ values for the seep associated

ammonites, when compared with nearby non-seep ammonites could be explained by the seep ammonites actively participating in the chemoautotrophically driven ecosystem. The range of ammonite $\delta^{13}C_{shell}$ values observed in our study is within the upper range of those observed for seep ammonites (-13.7‰ to 0.7‰), but also in lower range of the non-seep ammonites (-1.8‰ to 3.4‰) from Landman et al. (2012). Many of our ammonite samples are more depleted than the non-seep ammonite range from Landman et al. (2012).

On Seymour Island specifically, where all of the measured samples were collected, there is little clear evidence for methane seeps. On Snow Hill Island (Fig. 1), bivalves commonly associated with methane seeps (Eduardo Olivero, personal communication) have been found in association with well cemented mounds that are typical of preserved methane seep environments. The sediments on Snow Hill Island are stratigraphically equivalent to, or slightly below, the lowest deposits on Seymour Island, and demonstrate the potential of cold methane seep production in this area. While methane seeps could have been present contemporaneously to deposition on Seymour Island, there is no geologic evidence that the fossils were preserved in such an environment.

Slight decreases in $\delta^{13}C_{shell}$ have been observed in modern benthic mollusks (mussels) living exclusively at methane seep environments (Paull et al., 1989). Despite living on the seep itself, and feeding on highly depleted organic matter, the $\delta^{13}C_{shell}$ was only marginally depleted, ranging from -3‰ to -8‰. In contrast, their organic tissues were strongly influenced by the methane seep organic carbon, as almost all sampled tissues were below -70‰. The small effect on the shell isotopic values is likely because the local DIC pool is only marginally influenced by the exchange with the depleted carbon, and dominated by more typical ocean DIC values.

The range of $\delta^{13}C$ observed in these modern bivalves (Paull et al., 1989) is similar to that observed in the Seymour Island ammonites, and could be a potential explanation for the observed $\Delta\delta^{13}C_{ben\text{-}amm}$. For ammonites to preserve depleted $\delta^{13}C_{shell}$ value, but similar $\delta^{18}O_{shell}$ values, they

must live in water of similar temperature to the bivalves with which they were preserved, but with different $\delta^{13}C_{DIC}$ values, assuming no metabolic carbon contribution. In this scenario, ammonites could be moving between the depositional area where benthic mollusks are found and a methane seep environment, but spending a substantial portion of their life cycle at the methane seep, as their $\delta^{13}C_{shell}$ values are similar to mollusks living their entire life on the seep. This lifestyle could reflect a feeding preference for methane seeps, but a need to leave for more oxygenated waters. Alternatively, the ammonites could live exclusively at the methane seep, but their empty shells could be transported after their death, leading to their deposition with the benthic mollusks. In either case, large transport distances, either laterally or vertically in the water column, would be unlikely due to the good correspondence in water temperature ($\delta^{18}O$) with benthic mollusks and the size of the ammonite shells (Wani et al., 2005).

Conclusion

Ammonites from Seymour Island show a significant offset in $\delta^{13}C_{shell}$ when compared with benthic mollusks. Given that many studies involving different taxonomic groups find a notable $\Delta\delta^{13}C_{ben\text{-}amm}$, we believe the most likely vital effect is the contribution of metabolic carbon. Though we cannot rule out the possibility, it would be unlikely that ammonites in all of these locations all lived in methane seep environments and were transported or migrated to other locations before dying. In addition to the commonness of this pattern, the comparable $\delta^{18}O_{shell}$ values also suggest a metabolic carbon contribution is the most parsimonious interpretation. We believe that an elevated C_{meta} can, at least partially, explain the results from Landman et al. (2012). We do not dispute that the organisms in their study were all found on, and likely living in, a methane seep environment. From modern studies (Paull et al., 1989), even benthic mollusks living on top of seeps only see a mild methane carbon contribution to their shell carbonate. If the depleted carbon isotope values of seep ammonites were caused by depleted DIC values, the benthic mollusks living closest to the seep

should have a greater depletion that the nektic ammonites, the opposite of that observed by Landman et al. (2012). If the one significant outlier from the ammonite and benthic groups is removed, the populations also have means with statistically significant differences (-3.5‰ and -1.2% from ammonites and benthic mollusks; Students t-test p-value = 0.003).

Modern *Spirula* have also been shown to have an increased metabolic carbon contribution to their shell material despite their small size (Price et al., 2009) as have *Sepia* (Rexfort and Mutterlose, 2006) and fossil belemnites (Wierzbowski, 2002). Their internal shell may slow or reduce the connection between the EPF and the sea water, which one would predict to increase C_{meta}. We feel it is unlikely that ammonites would have a similar internal shell due to the complex shell ornamentation on many species, and lack of fossil evidence, though ammonite soft tissue preservation is very rare. More plausibly, many ammonite species have been interpreted as active swimmers (see Ritterbush et al., 2014 for a review), and an active swimming and feeding lifestyle could substantially increase their metabolic rate and amount of respired CO_2 produced. This signal would be expected to be recorded as more negative $\delta^{13}C$ values in the shell material unless the exchange rate between EPF and ambient sea water was increased. Unfortunately, with the exception of a few examples of *Diplomoceras*, ammonites found on Seymour Island are relatively compressed, smooth, planaspiral forms that are more hydrodynamic and more likely to be active swimmers (Ritterbush and Bottjer, 2012; Westermann, 1996). Higher energy demands could increase the susceptibility of adult ammonites to a major event like the end Cretaceous bolide impact when compared with the low energy demands of *Nautilus* (Boutilier et al., 1996). This affect would compound the vulnerability of ammonites planktonic egg forms compared with the benthic embryonic stage of *Nautilus* (Ward, 1996). A better understanding of this $\delta^{13}C$ anomaly could help contribute to our understanding of ammonite lifestyle, and their possibly their susceptibility to the end Cretaceous mass extinction.

Acknowledgements

Raw data for UW and PRI collections as available as Appendix 2.1 and 2.2 respectively. The authors would like to acknowledge support from NSF grant OPP-0739432, the University of Washington Earth and Space Sciences Department, and the Paleontological Research Institute John W. Wells Grants-in-Aid of Research Program. We would like to thank Gregory Dietl, Judith Nagel-Myers, and Leslie Skibinski for assistance with the PRI collections. Fossils are housed at the Burke Museum of Natural History and Culture (UW Collection) and at the Paleonotological Research Institute (PRI Collection). We would also like to thank Joseph Kirschvink, David J. Smith, Eduardo Olivero, Kelly Hillbun, Shane Schoepfer, and many others for assistance in the field.

Chapter 3. Extinction patterns, $\delta^{18}O$ trends, and magnetostratigraphy from a southern high-latitude Cretaceous – Paleogene section: links with Deccan volcanism (Tobin et al., 2012)

Thomas S. Tobin, Peter D. Ward, Eric J. Steig, Eduardo B. Olivero, Isaac A. Hilburn, Ross N. Mitchell, Matthew R. Diamond, Timothy D. Raub, Joseph L. Kirschvink

Abstract

Although abundant evidence now exists for a massive bolide impact coincident with the Cretaceous-Paleogene (K-Pg) mass extinction event (~65.5 Ma), the relative importance of this impact as an extinction mechanism is still the subject of debate. On Seymour Island, Antarctic Peninsula, the López de Bertodano Formation yields one of the most expanded K-Pg boundary sections known. Using a new chronology from magnetostratigraphy, and isotopic data from carbonate-secreting macrofauna, we present a high-resolution, high-latitude paleotemperature record spanning this time interval. We find two prominent warming events synchronous with the three main phases of Deccan Traps flood volcanism, and the onset of the second is contemporaneous with a local extinction that pre-dates the bolide impact. What has been termed the K-Pg extinction is potentially the sum of multiple, independent events, at least at high latitudes.

Introduction

Five major mass extinction events punctuate the history of animal life on earth. Of these, the Cretaceous-Paleogene (K-Pg) extinction is the most recent and well-studied. Like all mass extinctions, the K-Pg event was originally interpreted as a gradual event, but the discovery of unmistakable evidence of a large bolide impact with the Earth essentially coincident with the paleontologically recognized K-Pg mass extinction (Alvarez et al., 1980) led to a change in this paradigm. Today, more than three decades since the Alvarez et al. (1980) publication, a large

number of researchers are convinced that the bolide impact, located near present day Chicxulub, Mexico (Hildebrand et al., 1991), was either solely or largely responsible for the K-Pg extinction (Schulte et al., 2010). This view, however, has never been universal (Archibald et al., 2010; Courtillot and Fluteau, 2010), and reported evidence for impacts at the late Devonian (Playford et al., 1984), end Permian (Becker et al., 2001), and end Triassic extinctions (Olsen et al., 2002) have been disputed (respectively, Farley et al., 2005; McLaren, 1985; Tanner et al., 2008). Another candidate that may cause mass extinction, flood basalt volcanism, has been claimed to demonstrate strong temporal correlation with all mass extinction events over the past ~360 Ma, including the Deccan Traps large igneous province at the K-Pg boundary (Alvarez, 2003; Courtillot and Renne, 2003). Global warming, with associated climatic complications, provides a likely causal link between flood volcanic episodes at the Permian-Triassic (Siberian Traps) and Triassic-Jurassic (Central Atlantic Magmatic Province – CAMP) mass extinctions (Kump et al., 2005; Whiteside et al., 2010). Another hypothesis suggests that both flood volcanism and bolide impact combined are necessary for a major mass extinction (Arens and West, 2008; White and Saunders, 2005).

If flood basalt volcanism on a scale equivalent to the Siberian Traps or CAMP was indeed a mechanism causing mass extinction of species, there should be some signature of this during the emplacement of the Deccan Traps. To date, the geologically short interval during which the extinction, volcanism, and the impact occurred has confounded efforts to separate the biotic effects of Deccan Traps volcanism and the Chicxulub impact on end Cretaceous extinctions. The Deccan Traps erupted in three discrete pulses (Chenet et al., 2009; Jay et al., 2009), the second of which extruded a volume of basalt comparable to the Siberian Traps or CAMP events (Courtillot and Renne, 2003) sometime during the 400 yra prior to the K-Pg boundary. The outcrop sections on Seymour Island, Antarctica, provide an ideal place to examine the biotic impacts of Deccan volcanism due to their expanded nature and high paleolatitude location, allowing high temporal resolution in a location with increased sensitivity to climate change.

Field Setting

Seymour Island is located off the northeast of the Antarctic Peninsula (Fig. 3.1) at 64°S. It contains the stratigraphically highest exposures in the James Ross Island Group, well-exposed back-arc basin marine deposits that span the Early Cretaceous through the Early Paleogene. The basin has experienced minimal tectonic modification in the past 80 Ma, as evidenced by minor homoclinal tilt (5°-9°) and well-preserved fossils. Reconstructed paleolatitude (62°) is similar to current latitude and is in agreement with plate reconstructions (Torsvik et al., 2008), making Seymour Island one of the highest-paleolatitude K-Pg boundary outcrops. This location makes it ideal for examining climate changes associated with the K-Pg extinction, since polar amplification is likely to produce larger and more detectable temperature changes at high latitudes (Holland and Bitz, 2003; Manabe and Stouffer, 1980).

On Seymour Island, the biostratigraphically determined Maastrichtian through lower Danian interval is represented by the López de Bertodano Formation (LBF) which is uncomformably overlain by the Sobral Formation of Paleocene age. The LBF is comprised of over 1000 meters of predominantly immature mudstones with interspersed sandy and concretionary layers. Ten numbered informal lithostratigraphic units have been defined (Macellari, 1988, 1986) and are used here. This study focuses on the upper "molluscan units" (Units 7-10), which become increasingly fossiliferous through Units 9 and 10. Comprised mostly of siltstones with a larger percentage of sand and concretionary layers than the lower units, these upper units are interpreted as transgressive over the lower group, deposited in shelf and slope facies at water depths between 100 and 200 meters (Macellari, 1988; Olivero, 2012). Horizons containing early-diagenetic carbonate concretions, often rich in fossils, occur throughout at roughly ten-meter intervals. Although modern freeze-thaw cycling can disturb the structural integrity of finer-grained and

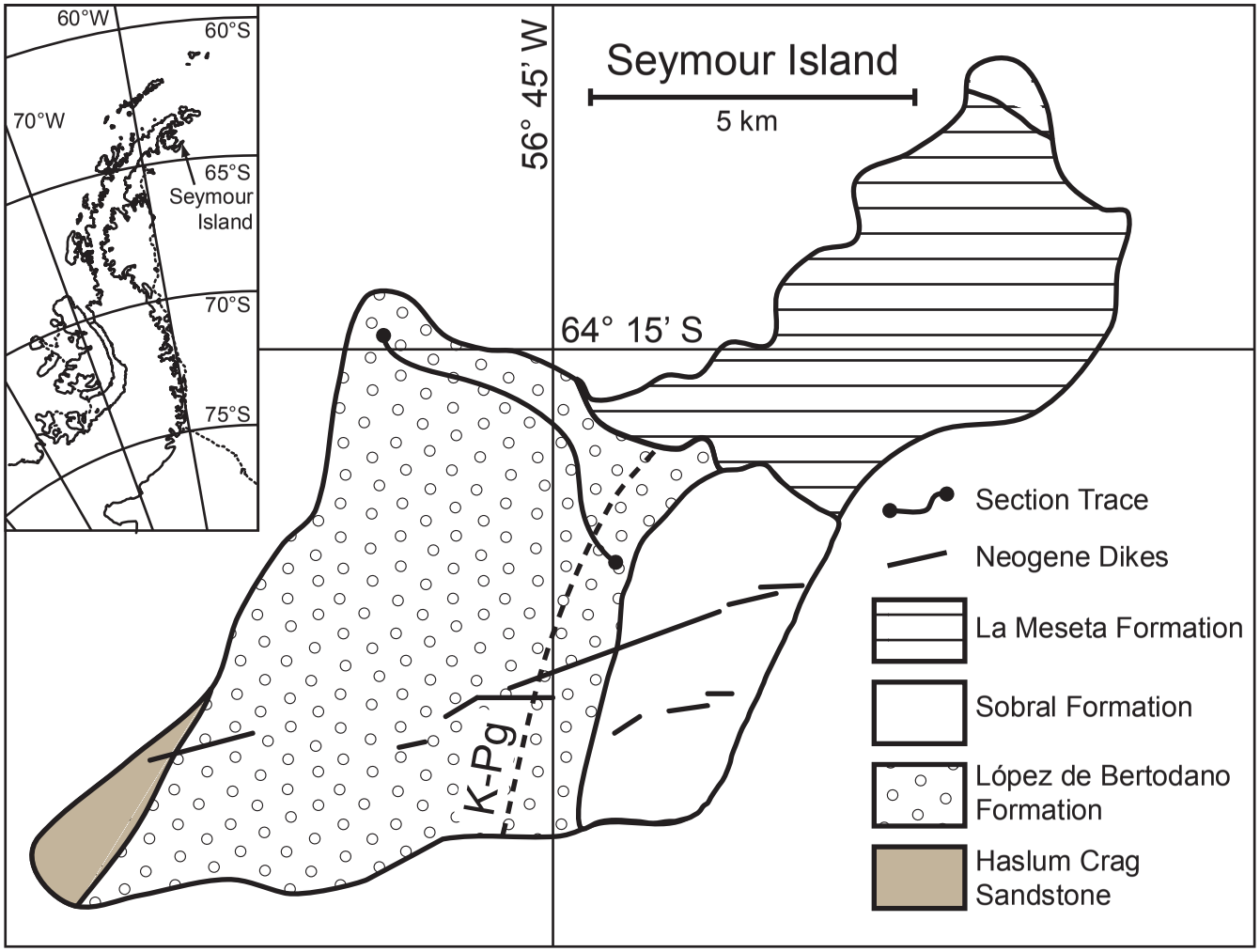

Figure 3.1. Map of Seymour Island and its location on the Antarctic Peninsula (inset) showing location of geologic formations and sampling trace, adapted from Dutton et al. (2007). GPS coordinates for sampling trace are available in Appendix 3.1.

loosely-consolidated mudstones, many of these indurated concretions retain their original orientation with respect to bedding and are suitable for paleomagnetic analysis.

Most fossils exhibit outstanding preservational characteristics, including the primary mineralogy and undeformed three-dimensional shape. Most mollusks, with the exception of originally calcitic pycnodonte bivalves, preserve original aragonite, which is recrystallized easily by heating or any form of diagenesis. Its presence is used as a guide for the collection of paleomagnetic and geochemical samples with minimal levels of thermochemical alteration (Filmer and Kirschvink, 1989; Ward et al., 1997).

The K-Pg boundary has been located between Units 9 and 10 of the upper LBF through various means in the past and is currently defined by the first occurrence of Paleogene dinocyst fossils that are essentially coincident with an iridium enhancement (Elliot et al., 1994). Apart from the iridium anomaly, global correlation of the late Cretaceous interval on Seymour Island has been hampered by the increasing endemism of macrofossils and microfossils in the Maastrichtian (Bowman et al., 2012; Macellari, 1987; Olivero and Medina, 2000) and an absence of any absolute age control from ash layers. While some age constraints from Sr isotope ratios on molluscan carbonate have been reported from the lower units of the LBF (McArthur et al., 2000), no age constraints prior to this study have been reported from the youngest units of this formation that approach and cross the K-Pg boundary.

Methods

The results of this paper hinge on three separate analytical techniques which are detailed below. Fossil material and paleomagnetic samples were collected from stratigraphic sections largely following previous studies (Crame et al., 2004; Macellari, 1988; Olivero et al., 2007). A schematic sample path is mapped in Figure 3.1, and specific GPS coordinates are available in Appendix 3.1. Magnetostratigraphy was used to create a high resolution chronostratigraphic

framework that allows for global correlation. Oxygen isotope analysis of well preserved fossil shell carbonate was used to reconstruct sea water temperature over the same stratigraphic interval. Additionally, fossil occurrence data from previous studies (Zinsmeister et al., 1989) were reexamined using modern statistical techniques that place confidence intervals on local multi-species extinctions (Wang and Marshall, 2004).

Paleomagnetism and Magnetostratigraphy- On Seymour Island, the LBF has deterred previous paleomagnetic studies primarily due to the tendency of the mudstone matrix to become unconsolidated during annual freeze-thaw cycles. It was thought that this annual surface disruption would scramble the orientation of any magnetic particles capable of preserving a stable natural remanent magnetization (NRM). However, the formation contains numerous layers with early-diagenetic carbonate-cemented concretions that are demonstrably in place; many of these contain 3-dimensionally preserved macrofossils, implying that the cementation occurred during early diagenesis before sedimentary compaction. Such concretions are thought to form by initial carbonate cementation at grain-grain contacts, a process that acts to lock in post-depositional remanent magnetizations without the inclination errors associated with sediment compaction (Filmer and Kirschvink, 1989; Ward et al., 1997). We targeted these concretionary horizons preferentially for paleomagnetic analysis. GPS coordinates for these major concretion beds, as well as their tie-in to the measured stratigraphic section, are given in Appendix 3.1. Digital images of sampling sites, as well as the magnetic data used in this study, are deposited at the Magnetic Information Consortium (MagIC) site (http://earthref.org/MAGIC/).

Thermochemical alteration is essentially absent in the Campanian through Maastrichtian strata of the James Ross Basin. Molluscan fossils from Seymour Island preserve nacreous metastable aragonite. Iridescence in molluscan nacre is a result of a diffraction grating effect of un-denatured protein layers within the original aragonite (Lowenstam and Weiner, 1989), and its

presence in ancient rock constrains the peak burial metamorphic conditions to be less than ~60° C with none of the thermochemical alteration which often remagnetizes sediments. In addition, extensive petrographic work reported by Pirrie (1994) shows no evidence for smectite-illite transformation, conversion of clinoptilolite-heulandite to analcite, increased vitrinite reflectivity, or resetting of fission-tracks in apatite, all of which are consistent with shallow burial and no significant heating. Presumably, secondary magnetic components would be due to a combination of viscous remanent magnetizations (VRMs) or the formation of antiferromagnetic minerals during recent surface weathering. However, in sediments of this sort it is quite common for thermochemical changes during demagnetization at fairly low temperatures (< 300°C) to produce fine-grained ferrimagnetic phases during decomposition of clays and Fe-rich carbonate phases. Hence, it is necessary to use the hybrid demagnetization strategies noted below to identify and isolate secondary components, and much of the stable remanence appears to be preserved in ferrimagnetic minerals (such as biogenic magnetites) that have blocking temperatures < 300°C due to thermal-demagnetization reactions. These techniques have proven effective in past studies of Cretaceous sediments with similar lithologies (Filmer and Kirschvink, 1989; Ward et al., 1997).

We collected samples for paleomagnetic analysis as oriented blocks broken from concretions that were judged to be essentially in place (examples in Figure 3.2). As surface weathering can produce a trace of the antiferromagnetic mineral goethite, we took special care to crack open concretions in the field in search of those that were visibly the least altered. From these we cut a series of 1 cm-high, 2.54 cm diameter cylindrical samples for paleomagnetic and rock magnetic analyses. One or more specimen from each sample was analyzed at the California Institute of Technology paleomagnetics laboratory, using 3-axis DC-SQUID moment magnetometer systems housed in magnetically shielded rooms. The background noise of these instruments is less than 1 picoA·m^2, and they are equipped with the vacuum pick-and-place, computer-controlled sample handling systems that can measure up to 180 samples automatically. AF demagnetization was

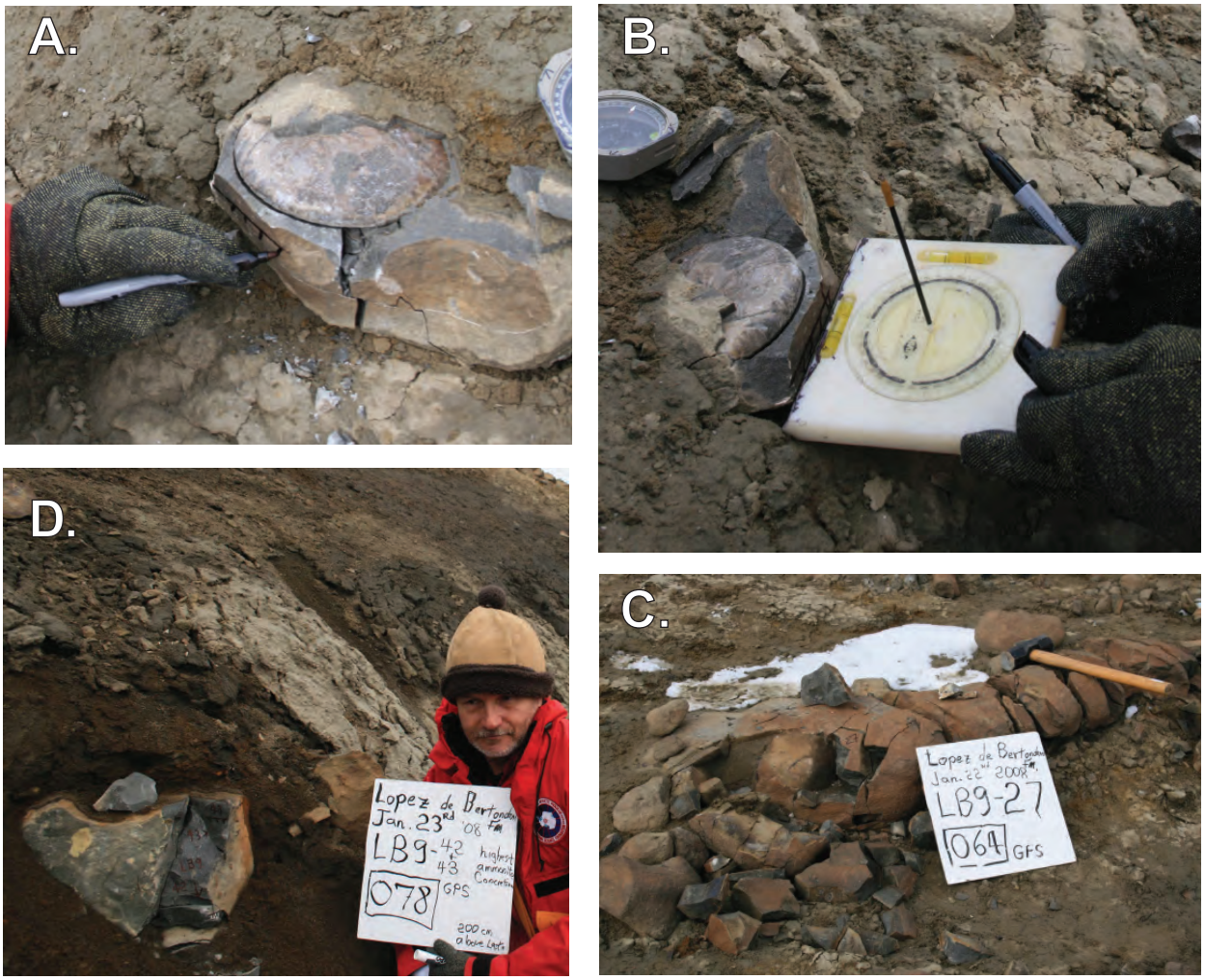

Figure 3.2. Example of a typical concretion in the Lopéz de Bertodano Formation of Seymour Island, Antarctica. A horizontal line is first drawn on a flat surface, and a perpendicular line is drawn to it define together a planar surface. The azimuth of the horizontal line is measured in the right-handed fashion, both with magnetic and sun compass (where available). This particular example also shows the preservation of an ammonite, located about 15 m below the stratigraphically defined position of the K-Pg boundary. The pearly aragonite in the fossil is an indicator of the low levels of diagenesis in the samples. (C) Concretions are elongated, lenticular bodies that have been fractured during repeated freeze/fracture cycles in the Antarctic winter. This is an example of an elongate such concretion that was sampled for paleomagnetics. (D) example of an ammonite-bearing concretion just 1 m below the Cretaceous/Paleocene boundary at the Zinsmeister locality on Seymour Island.

performed with computer-controlled, three-axis coil systems fit in-line in the sample path. Thermal demagnetization was performed in commercially-built magnetically shielded furnaces that had been modified to minimize sample oxidation by using a gentle flow of N_2 gas to expel air and measured twice after each set of demagnetization experiments, in the 'arrow-up' and 'arrow-down' modes (Kirschvink et al., 2008). This allows the averaging of eight sets of independent measurements, providing several additional measures of measurement reliability.

For paleomagnetic analyses, one sample was selected for detailed demagnetization from the sample set generated at each locality, and if this proved to unstably magnetized, additional sub-samples were run through the demagnetization analysis, particularly from sites in critical intervals. Specimens were initially measured for NRM and then subjected to several low-temperature cooling cycles in liquid nitrogen (77 °K) to remove viscous components often held by magnetically-soft, multi-domain magnetite grains that might be present (Dunlop and Ozdemir, 1997; Halgedahl, 1993). This was then followed by low alternating-field (AF) demagnetization up to 6.9 mT in 2.3 mT steps to remove low coercivity magnetizations, such as those that might have been introduced during passage through airport X-ray machines. The samples were then treated with thermal demagnetization from ~60°C in 5 to 25°C increments up to 400°C, or until they displayed unstable, irreproducible behavior (examples shown in Fig. 3.3), presumably from the formation of magnetite from thermal decomposition of glauconitic clays. Demagnetization data were analyzed using principal component analysis (Kirschvink, 1980), using the now-standard criteria: Only demagnetization lines with MAD values below 10° and circles below 15° were included in the statistical analysis shown in Figure 3.4 and Table 3.1. Mean directions were obtained using Fisher statistics (Fisher, 1953). The method of McFadden & McElhinny (1988) was used for combining data from demagnetization lines and arcs, and the final iterative directions along the arc constraints were combined with lines for the stratigraphic polarity interpretation. The reversals test followed that of McFadden & McElhinny (1990).

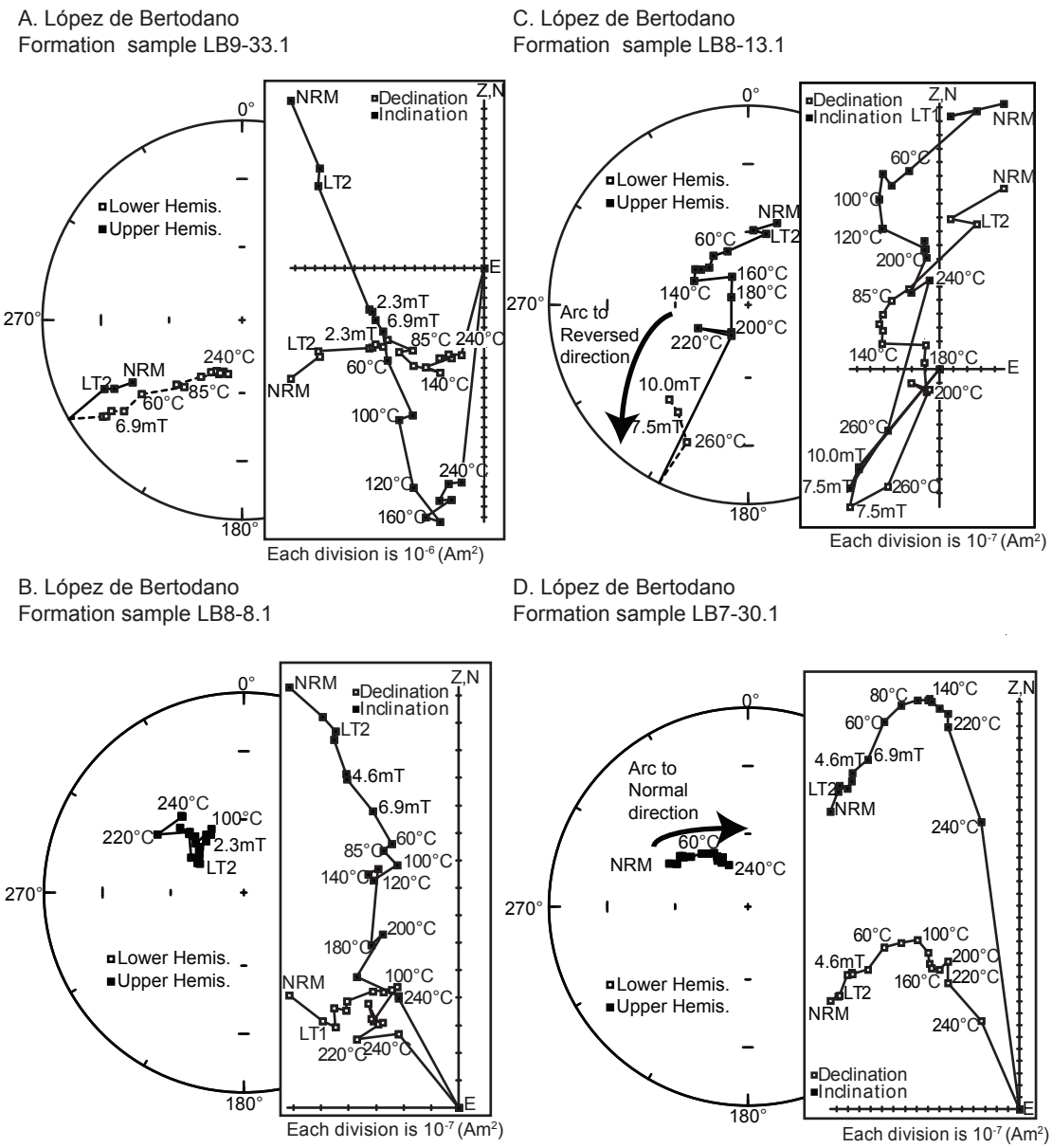

Figure 3.3. Typical demagnetization behavior of samples from the López de Bertodano Formation. Projections use tilt-corrected directions. (A) On sample LB9-33.1, low-temperature thermal cycling, low-field Alternating-Field, and relatively low thermal demagnetization removes a nearly vertical component interpreted to be of Recent origin, producing a clear directional arc to the South/Down component interpreted to be of late Cretaceous (chron 29R) origin. (Higher T data where the magnetization becomes unstable are not shown). (B) Sample LB8-8.1 is interpreted to be of Normal polarity, as the low-intensity demagnetization procedure removes a similarly steep up direction to that of LB9-33.1, yet it retains a North/Up direction well beyond this point. (C) Sample LB8-13.1 shows an example of a demagnetization circle heading towards the Reverse direction, but becomes unstable before isolating the stable component. D. Sample LB7-30.1 similarly shows a clear arc associated with the removal of a magnetically soft component, leading to the isolation of a characteristic direction interpreted as Normal polarity.

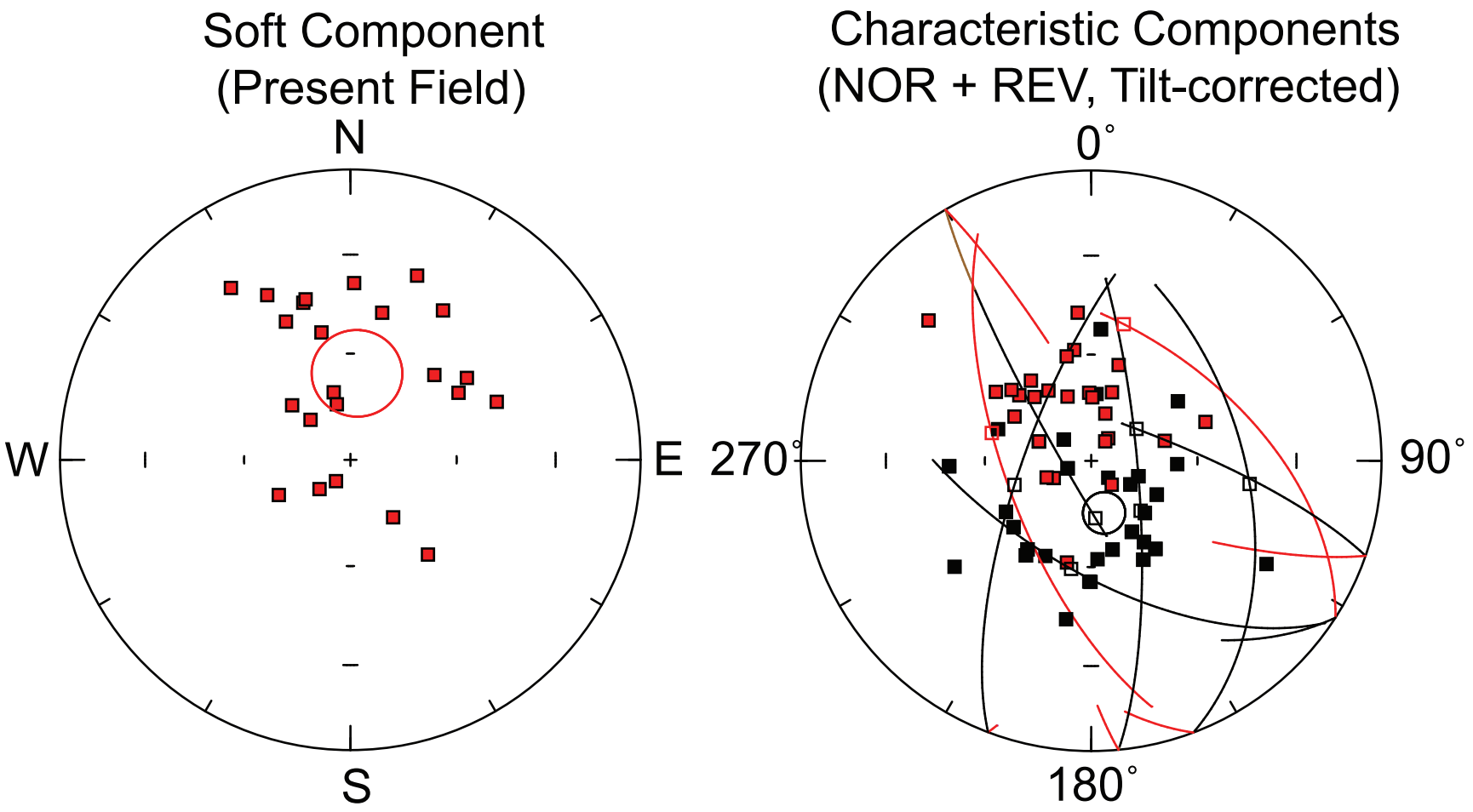

Figure 3.4. Equal-area plots showing the principal magnetic components isolated from the demagnetization data generated in this study. Directions obtained from linear components are shown as solid squares, and the arc-segments show the constraints from demagnetization planes (McFadden and McElhinny, 1988) with the last directional iteration indicated as a hollow square. Data for the cones of 95% confidence are shown in Table 3.1. Black (red) points are lower (upper) hemisphere.

Table 3.1.
Paleomagnetic results from Units 5-10 of the López de Bertodano Formation on Seymour Island, Antarctic Peninsula. 'N_{eff}' indicates the effective number of samples in the analysis, and numbers indicated like '(L, C)' give the number of individual demagnetization Lines and Circles, respectively (N_{eff} = L + ½P (McFadden and McElhinny, 1988)). NOR = Normal, REV = Reversed magnetic field direction; PLF = Present local field. R=mean resultant vector length; α95=radius of 95% confidence cone around mean ; κ=Fisher precision parameter (Fisher, 1953). dp,dm=confidence limits on pole for semiminor/semimajor axes respectively. G_r=Fisher test statistic.

LBF Units 5-10, Seymour Island, Summary of Fisherian Statistics						
	N (eff.)	**R**	**Decl.**	**Incl.**	**α95**	***κ***
NOR + REV	67.5 (60, 15)	61.5	27.8	-77.1	5.45˚	11.04
	tilt corr:	61.5	352.5	-73.1	5.45˚	11.03
NOR	32 (30, 4)	29.6	27.8	-74.7	7.31˚	13.07
	tilt corr:	29.6	356.9	-71.1	7.31˚	13.05
REV	35.5 (30, 11)	31.9	208.1	79.6	8.21˚	9.58
	tilt corr:	31.9	166.9	75.0	8.20˚	9.59
PLF	38	31.8	4.2	-72.5	10.43˚	5.94
The combined tilt-corrected pole is at 83.3˚ N, 267.5˚ E, (dp, dm) = (9.8˚, 10.7˚), paleolatitude -62˚ ± 9˚						
The hypothesis that the Normal and Reversed directions are antiparallel cannot be rejected at the 95% confidence level (Gr = 1.23, Chi^2, p. value 0.542), passing the McFadden & McElhinny reversal test in category "C" (Antiparallel angle = 4.9˚; Critical angle = 10.7˚).						

Rock magnetism- A series of rock-magnetic analyses were also performed on representative samples of each lithology, using routines implemented on the RAPID consortium magnetometers (Kirschvink et al., 2008). The NRM of these specimens was demagnetized in 3-axis alternating fields in 21 logarithmically distributed steps between 2.1 and 80 mT. This was followed by a 20-step progressive ARM acquisition in 100 mT AF fields along the vertical axis with a DC biasing field between 0 and 1 mT. The maximum ARM was then AF demagnetized in the same logarithmic sequence used on the NRM, except along the vertical axis only and up to the maximum vertical AF field of 158.4 mT (28 steps). The sample was then given a vertical-axis IRM of 100 mT and AF demagnetized in the same 28 steps. An IRM acquisition series was then run with the same logarithmic sequence, but up to the maximum IRM pulse field of 350 mT (36 steps). In turn, this saturation IRM was AF demagnetized in the 28 step sequence up to 158.4 mT. Finally, the sample was given an IRM of 350 mT, the polarity of the pulse was reversed, and it was subjected to a 36-step DC backfield demagnetization. This set of experiments allows the construction of moderately high-resolution coercivity spectra, as well as the determination of parameters, including IRM and ARM strength, coercivity of remanence, the Cisowski (1981) magnetostatic interaction parameter R, and ARM susceptibility. This total ~200-step experiment takes ~4.5 hours per specimen. MATLAB scripts used to analyze the rock magnetic data are available through links on the RAPID website (www.rapid.gps.caltech.edu).

Paleotemperature- Fossil shell carbonate from ammonites, gastropods, bivalves and echinoids was collected for isotopic analysis of $\delta^{13}C$ and $\delta^{18}O$. Carbonate material was powdered using a Merchantek Micromill for precise sampling of shell material. Powdered material was analyzed using a Kiel III Carbonate Device attached to a Delta Plus isotope ratio mass spectrometer. Samples (0.020 – 0.100 mg) were reacted at 70°C with 100% anhydrous phosphoric acid and analyzed interspersed with internal lab calcite standards calibrated to NBS-18 (-23.01‰ VPBD) and NBS-19

(-2.20‰ VPDB) for $\delta^{18}O$ and NBS-19 (+1.95‰ VPBD) and LSVEC (-46.6‰ VPBD) for $\delta^{13}C$. Fractionation factors for aragonite and calcite at 70°C follow Kim et al. (2007a).

Despite surface confirmation of visibly unaltered material in thick section, the process of drilling into a sample may still entrain adjacent, altered material. The powder aliquot from each sample was analyzed for trace element concentrations, including Fe, Mg, Mn, Sr, and Na, using an ICP-AES. These data were used to assess diagenesis, both through comparison with published ranges of accepted, unaltered values (Brand and Morrison, 1987; Morrison and Brand, 1986) and through comparison with the $\delta^{18}O$ data. Representative samples of aragonite fossil species common in the section were analyzed using X-Ray Diffraction (XRD) to confirm both primary mineralogy and diagenesis. All analyzed molluscan samples, with the exception of pycnodonte (calcite-secreting) bivalves, were confirmed as aragonite with no detectable calcite present.

The $\delta^{18}O$ values in their stratigraphic context divided taxonomically can be seen in Figure 3.8. Each taxonomic group was analyzed for covariance between $\delta^{18}O$ and concentration of Fe, Mg, Mn, Sr, and Na and compared with accepted ranges (example in Fig. 3.5). As many as half of all shells (n=168) were found to be higher than the thresholds for Fe (within limits n=83) and Mn (n=91), a third for Mg (n=127), and a fifth for Sr (n=149) and Na (n=139). Culling the data by removing shells outside the limits for each trace element does not alter the overall $\delta^{18}O$ pattern. Similarly, the $\delta^{18}O$ patterns for each taxonomic group analyzed individually are largely indistinguishable from the whole data set provided stratigraphic coverage was sufficient (e.g. echinoids have little stratigraphic coverage and ammonites are not found in the Danian). Cross plots of $\delta^{13}C$ v. $\delta^{18}O$ showed no significant statistical trends for any taxonomic group (Fig. 3.6). Values of r^2 ranged from .26 (gastropods) to .009 (bivalves). Though there were large variations in $\delta^{13}C$ for echinoids and ammonites, removal of shells with “anomalous” $\delta^{13}C$ values from the data set had no significant effect on reconstructed paleotemperature patterns. Due to the lack of significant

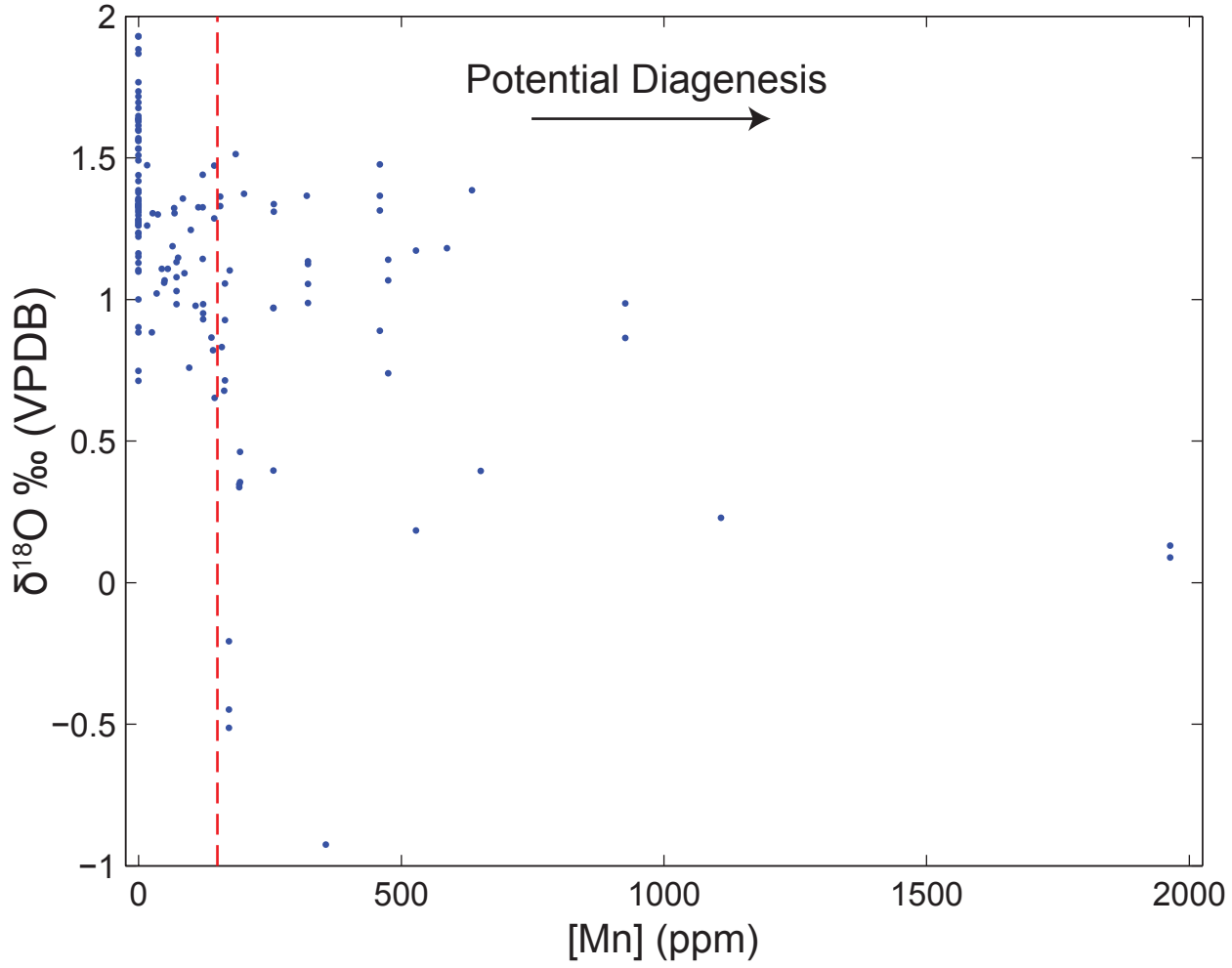

Figure 3.5. Relationship between $\delta^{18}O$ and [Mg] for aragonitic gastropods as an example of typical diagenetic assessment. The diagenesis window is as determined by Morrison and Brand (1986).

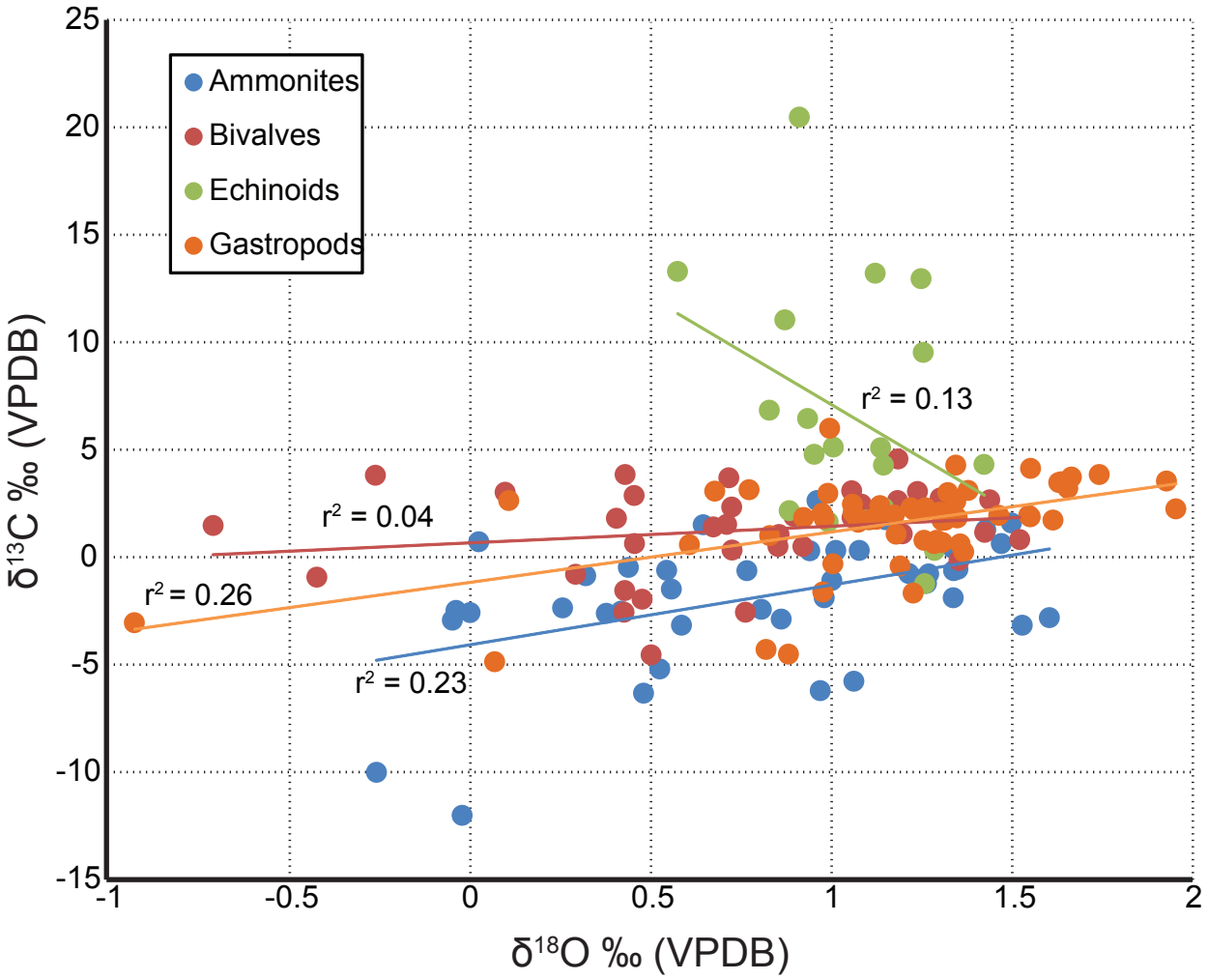

Figure 3.6. Cross plot of $\delta^{18}O$ v. $\delta^{13}C$ for the four taxonomic groups studied. No significant trends were observed in any taxonomic groups. Echinoids displayed substantially different $\delta^{13}C$ values for similar $\delta^{18}O$ values.

covariance between any individual trace element and $\delta^{18}O$ for any taxonomic group and the similarities between all versions of the culled data and the full data set, we reconstructed the paleotemperature record using the full data set, though the data set culled based on trace element concentrations is also displayed.

Paleotemperature estimates were made following the procedures of Kim et al. (2007b) and Kim and O'Neil (1997) for aragonite and calcite respectively. Organisms generally deposit carbonate under equilibrium conditions with respect to seawater (Weiner and Dove, 2003). For the Cretaceous, this seawater is assumed to be -1.0‰ (VSMOW) based on modeled ocean chemistry given a predominantly ice-free world (Shackleton and Kennett, 1975). The paleotemperature record through the section was created by taking the mean of multiple measurements on each shell, and then taking the mean of all averaged shell values in 100 kyr bins. Uncertainties are reported as 1.96 x standard error, equivalent to a 95% confidence interval (Altman and Bland, 2005). The uncertainties for time bins containing only a single shell were omitted, as the standard deviation could only be calculated for intra-shell variation, a significant underestimation of the uncertainty.

Extinctions- The molluscan units of the LBF contain a diverse array of invertebrate fauna and a smaller number of marine reptiles and other vertebrates. We analyzed 326 occurrences distributed among 77 species from Units 8-10 previously reported from Seymour Island (Zinsmeister et al., 1989). For a quantitative analysis of extinction patterns, we eliminated fauna with only one stratigraphic occurrence. The technique for assigning a confidence interval to an extinction event was first undertaken by Marshall (1995) in this locality using only ammonite species. Here we increase the sample size by utilizing other, largely molluscan, taxonomic groups as well. Extinction confidence intervals were calculated using the methods of Wang and Marshall (2004). We diverged from their methods in calculating confidence intervals without one of their recommended improvements to Marshall (1995), as we did not use the highest stratigraphic occurrence of any of

the included species as the lower bound of the extinction confidence interval. By employing this method, we could better test whether different extinction events were stratigraphically distinct.

Results

Rock Magnetism- Results support the interpretation that the NRM is carried by fine-grained magnetite of detrital origin, although some antiferromagnetic minerals from weathering might also be involved. Rock magnetic data from a suite of six representative samples are summarized in Figure 3.7. In particular, the Lowrie-Fuller test on all samples is strongly positive, indicating the magnetic mineralogy of particles with Hc values below 100 mT is dominated by interacting single-domain to pseudo-single-domain behavior. Similarly, ARM acquisition characteristics indicate dominance by strongly interacting pseudo-single-domain to multi-domain particles. However, the median destructive field of IRM acquisition tends to be about 80 to 100 mT, arguing against a large multi-domain magnetite fraction, indicating that the PSD particles must be fairly elongate. This is in agreement with the liquid nitrogen cycling, which typically would unblock only 5-20% of the NRM. Less than 5% of the IRM is gained in fields above 300 mT, suggesting a minor fraction perhaps from antiferromagnetic minerals that typically are present from surface weathering. The Fuller test of NRM origin in all cases shows that the ARM values upon demagnetization are two to three orders of magnitude greater than the values of the NRM, which strongly suggests that the NRM is either detrital or chemical in nature.

Paleomagnetism and Magnetostratigraphy- Slightly over half of the paleomagnetic samples (63/112) could be characterized as well behaved, with most having at least one specimen which possessed a component of low AF and thermal stability similar to the present magnetic field direction in Antarctica, as well as one or two additional components of higher stability. Due to the overall shallow dip of the beds on Seymour Island and the similarity of the Late Cretaceous paleogeography for Antarctica to that of the recent, the Reversed characteristic directions (South

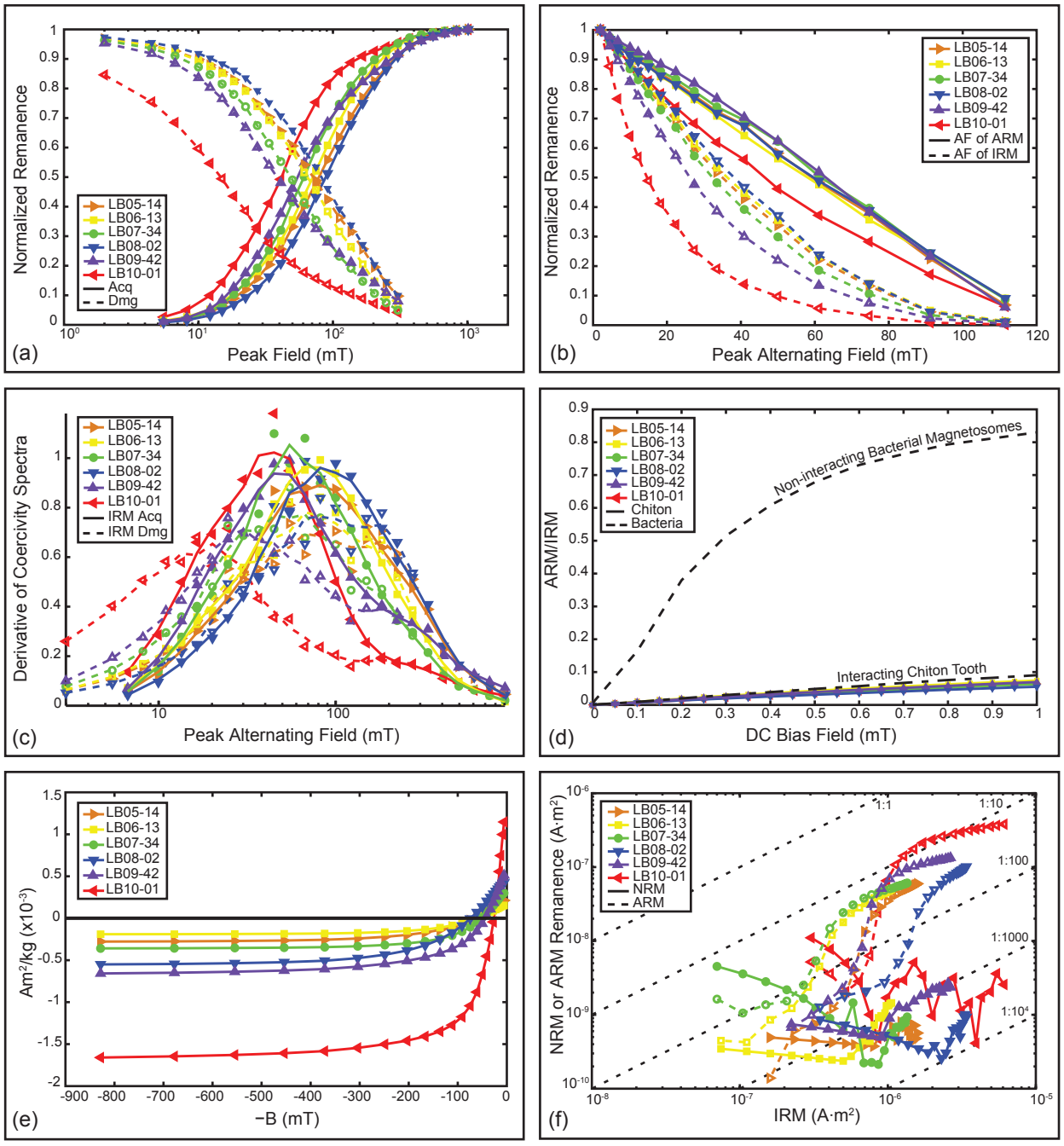

Figure 3.7. Rock magnetic characterization of representative lithological samples from concretions of the Lopéz de Bertodano Formation (LBF), members 5-10, from Seymour Island. Sample code and symbols are the same for all experiments. (A) Coercivity spectra determination of IRM acquisition and demagnetization (Cisowski, 1981). (B) Lowrie-Fuller ARM test. (C) Derivative of the IRM-based coercivity spectra. (D) ARM acquisition test for magnetostatic interactions (Kobayashi et al., 2006). (E) Backfield IRM. (F) Fuller test of the origin of NRM (Fuller et al., 1988).

and Down) are easy to separate from modern-day overprints (North and Up). However, Normal samples are difficult to distinguish from samples with strong recent overprints without using some other objective criteria. On the assumption that the intrinsic polarity of a sample does not depend on the magnetic mineralogy, we first analyzed the stability spectra of samples displaying Reversed components as a guide to the stability spectra of both the Normal and Reversed characteristic components. A Normal polarity interpretation therefore required demagnetization stability well into that displayed by the group of Reversely magnetized samples, aided sometimes by the presence of short great-circle arcs at the low demagnetization ends.

Representative orthogonal projections of the demagnetization trajectories are shown in Fig. 3.3, and all of the demagnetization data used for this paper are deposited in the Magnetic Information Consortium (MagIC) database. Below about 250 to 300°C, demagnetization trajectories generally are stable and linear, giving the character of the underlying characteristic component. Above these values, however, magnetic directions often become erratic, apparently picking up spurious directions even in the weak magnetic field (< 200 nT) of the shielded laboratory room. Monitoring of the remanence with susceptibility before each measurement suggests that we are experiencing the decomposition of iron bearing clays, and perhaps some of the pyrite, into finer-grained ferrimagnetic minerals. Nevertheless, the removal of multi-domain magnetite carriers with low temperature cycling in liquid nitrogen, followed by low-field alternating field demagnetization, and the fact that the rocks have never been heated appreciably above even 60°C, argue that we are seeing a real characteristic component of Cretaceous age before the samples become unstable. As noted below, we also find that the magnetic polarity of this characteristic component is in broad agreement with the geomagnetic reversal timescale for late Maastrichtian and early Danian time.

As a group, the mean normal and reversely magnetized directions isolated with this procedure are statistically anti-parallel, passing the reversals test (mean angular offset 4.9˚, critical

angle 10.7°, see Table 3.1) for a Category C of McFadden and McElhinny (1990). The combination of the positive reversals test and the presence of layer-bound magnetic polarity zones strongly imply that the characteristic magnetization was acquired at or shortly after the time of deposition. Given the robust number of samples yielding useable results and the excellent age constraints on the K-Pg boundary, the mean direction rates a perfect 7 on the 7-point paleomagnetic quality (Q) index of Van der Voo (1993).

The magnetostratigraphic record for the Maastrichtian through lower Danian on Seymour Island is shown in Figure 3.8. All sites from the oldest part of the sequence, Units 5, 6, and those at the bottom of 7, are reversely magnetized, whereas the upper half of Unit 7, most of 8, and the lower half of 9 are Normal. A short Reversed interval is characterized by two samples in the middle of Unit 8, and the upper half of Unit 9 and most of Unit 10 are Reversed. One Normal sample was measured at the top of Unit 10 prior to the overlying unconformity. This magnetic polarity pattern has a straightforward interpretation. The K-Pg boundary is known to occur within Magnetic Chron 29R (Alvarez et al., 1977), which identifies the Reversed zone in the top half of Unit 9, and most of Unit 10, as C29R. The reversed interval in Unit 8 is most likely the short duration C30R, while the overlying and underlying Normal zones are C30N and C31N respectively. The lowest zone is C31R, though its base is unconstrained. The uppermost point in Unit 10 is likely the beginning of C29N. A chronostratigraphic framework (Fig. 3.9) was constructed with linear interpolation between the known time points provided by these reversals and the K-Pg boundary (Gradstein et al., 2004) adopted here. The consistent sedimentation rate through the section further supports the above magnetostratigraphic interpretation.

Paleotemperature- Shown in Figure 3.10 is the paleotemperature record in 100 ka binned intervals using an age model described above. Data from all analyzed specimens, as well as a culled selection based on diagenetic indicators, are both shown and largely consistent. Overall, these

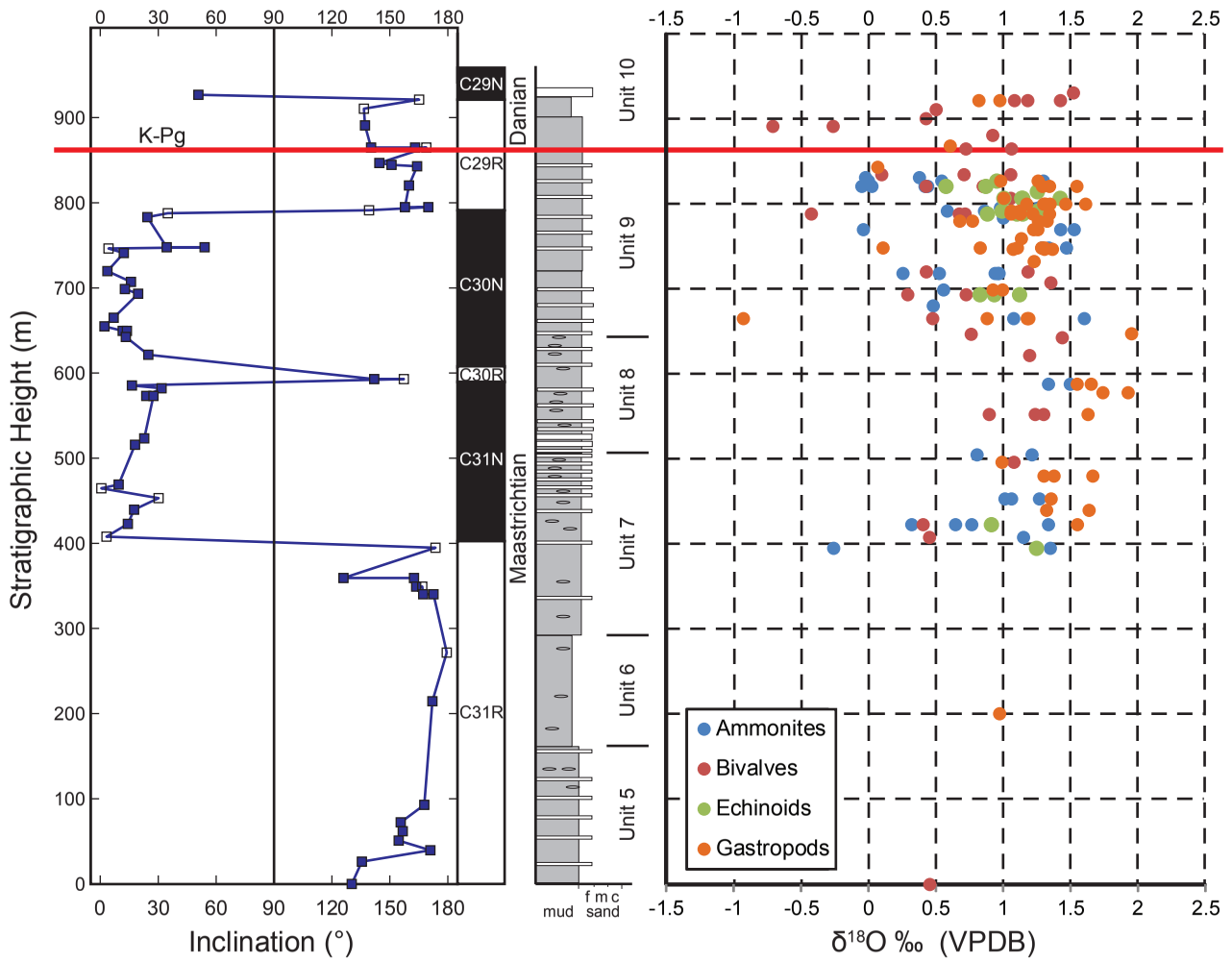

Figure 3.8. Compiled magneto-, litho-, and isotopic stratigraphic results for the upper half of the Lopéz de Bertodano Formation, representing the Maastrichtian and Lower Danian interval. Units are the informal units as described by Macellari (1986). At left is the magnetic polarity interpretation is indicated by the tilt-corrected inclination of the stable remanence vectors, with solid symbols indicating results from samples that demagnetize to a stable end position and open symbols showing the final iterative position of best directions along the demagnetization arcs. At right are the δ18O values sorted by major taxonomic group.

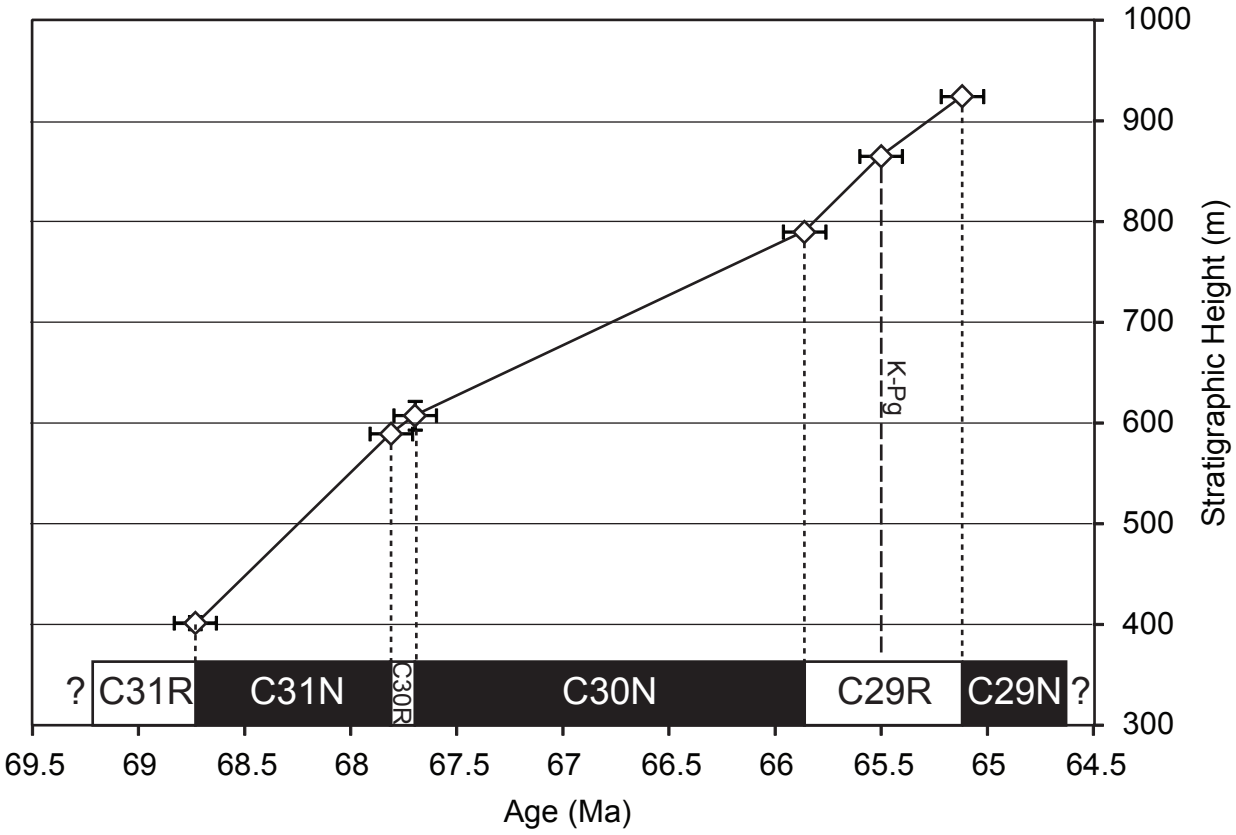

Figure 3.9. Age model assuming constant sedimentation rate between known tie points derived from magnetostratigraphy and the K-Pg boundary. Sedimentation rate is fairly constant throughout the interval (0.1-0.2 mm/a).

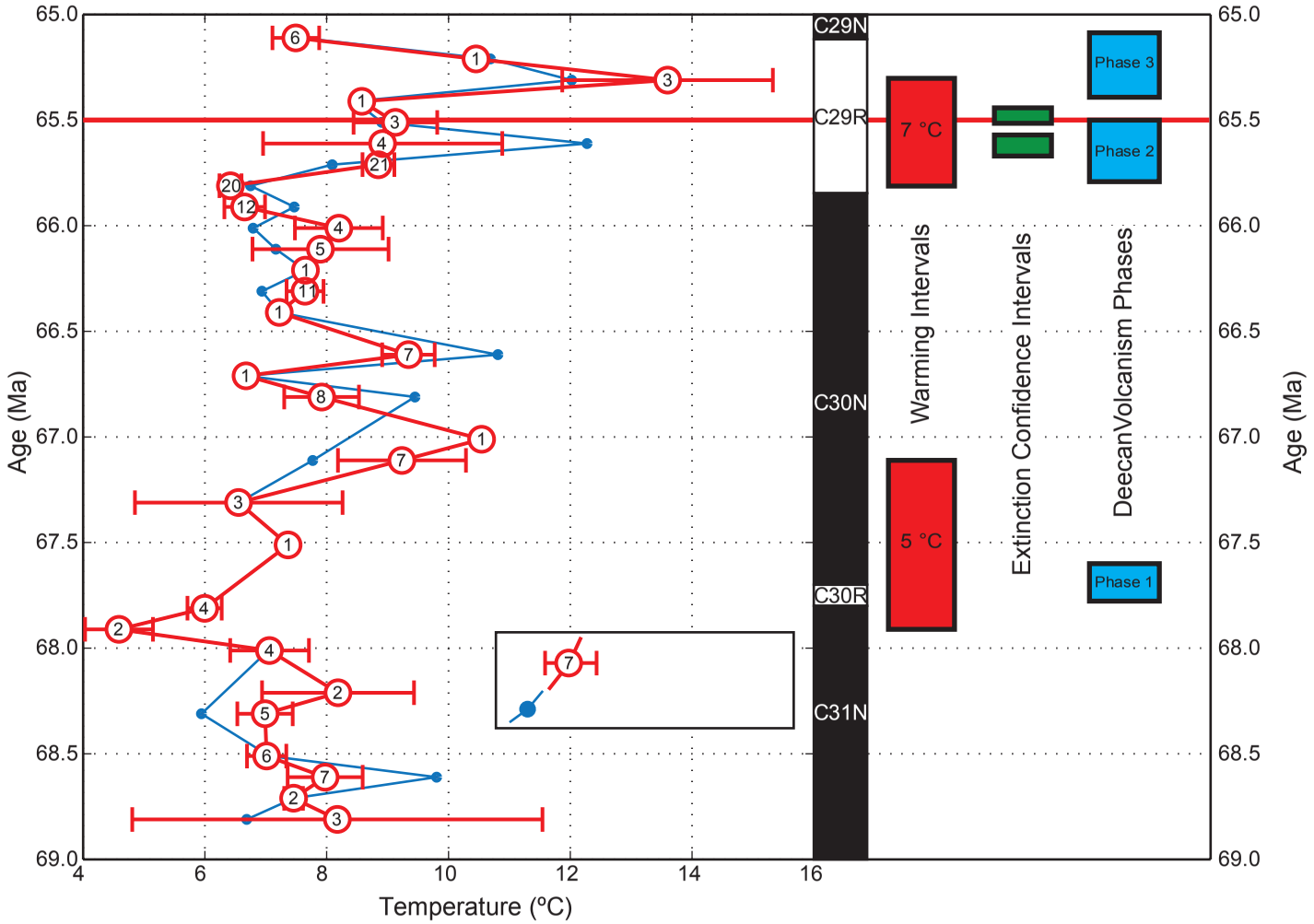

Figure 3.10. Reconstructed paleotemperature record from $\delta^{18}O$ in molluscan shell carbonate using all shells (open circles) and a culled data set where shells outside trace element bounds are not included (in blue). Data is binned in equal time bins of 100 ka, with uncertainties representing a 95% confidence interval (standard error x 1.96 (Altman and Bland, 2005)) based on multiple shells, while the circled number represents the number of shells in a given bin. Warming intervals of greater than 3°C are highlighted. At right are the extinction intervals observed in Figure 3.9, as well as the magnetostratigraphically correlated phases of Deccan Traps flood volcanism. Correlations between warming and volcanism are statistically significant ($p<0.01$).

paleotemperature results are consistent with previous macrofossil studies in this area (Ditchfield et al., 1994; Dutton et al., 2007; Elorza et al., 2001) as well as estimates from microfossils (Barrera et al., 1987), when analyzed using newly available calibrations for carbonate-temperature (Kim et al., 2007b) and carbonate-acid (Kim et al., 2007a) relationships. Warming intervals are highlighted during any continuous warming trend of at least 3°C, excluding data points comprised of a single shell, yielding two notable warming events. The first occurs between 67.9 and 67.1 Ma, the second between 65.8 and 65.3 Ma. The second warming interval could plausibly be split into two separate events 65.8-65.6 Ma and 65.5-65.3 Ma, an interpretation supported by the culled data set. The difference between these two intepretations is primarily seen in the magnitude of the warming and the decay rate of the climatic perturbation. Both possibilities are explored in a statistical analysis in section 5. Warming during the last several thousand years of the Cretaceous has been recognized in deep ocean cores from benthic foraminiferal data at both mid- (Li and Keller, 1998) and southern high latitudes (Barrera and Savin, 1999; Barrera, 1994), though at lower magnitudes. Similar patterns have also been observed in mid-latitude terrestrial and near-shore settings (Wilf et al., 2003), suggesting that temperature variability at high latitudes may reflect change on a global level.

Extinction- Figure 3.11 shows previously reported faunal data from the LBF and newly determined extinction confidence intervals, demonstrating two separate extinction events. Species with a single occurrence are included in the figure but not in the statistical evaluation. The latter of the two extinctions is synchronous with the K-Pg boundary, while the earlier occurs over a narrow interval 40 meters below the K-Pg. Using the age model described above, this event occurs approximately 150 kyr prior to the K-Pg boundary. There is a notable difference in the selectivity of the two extinctions relative to the organisms' mode of life. The precursor extinction affects 10 marine invertebrate species, 9 of which are benthic, in contrast to the K-Pg boundary extinction where only 6 of 14 total extinct species are benthic. There is no apparent selectivity to the extinction within benthic fauna relative to trophic level or sediment position in the precursor extinction. The most

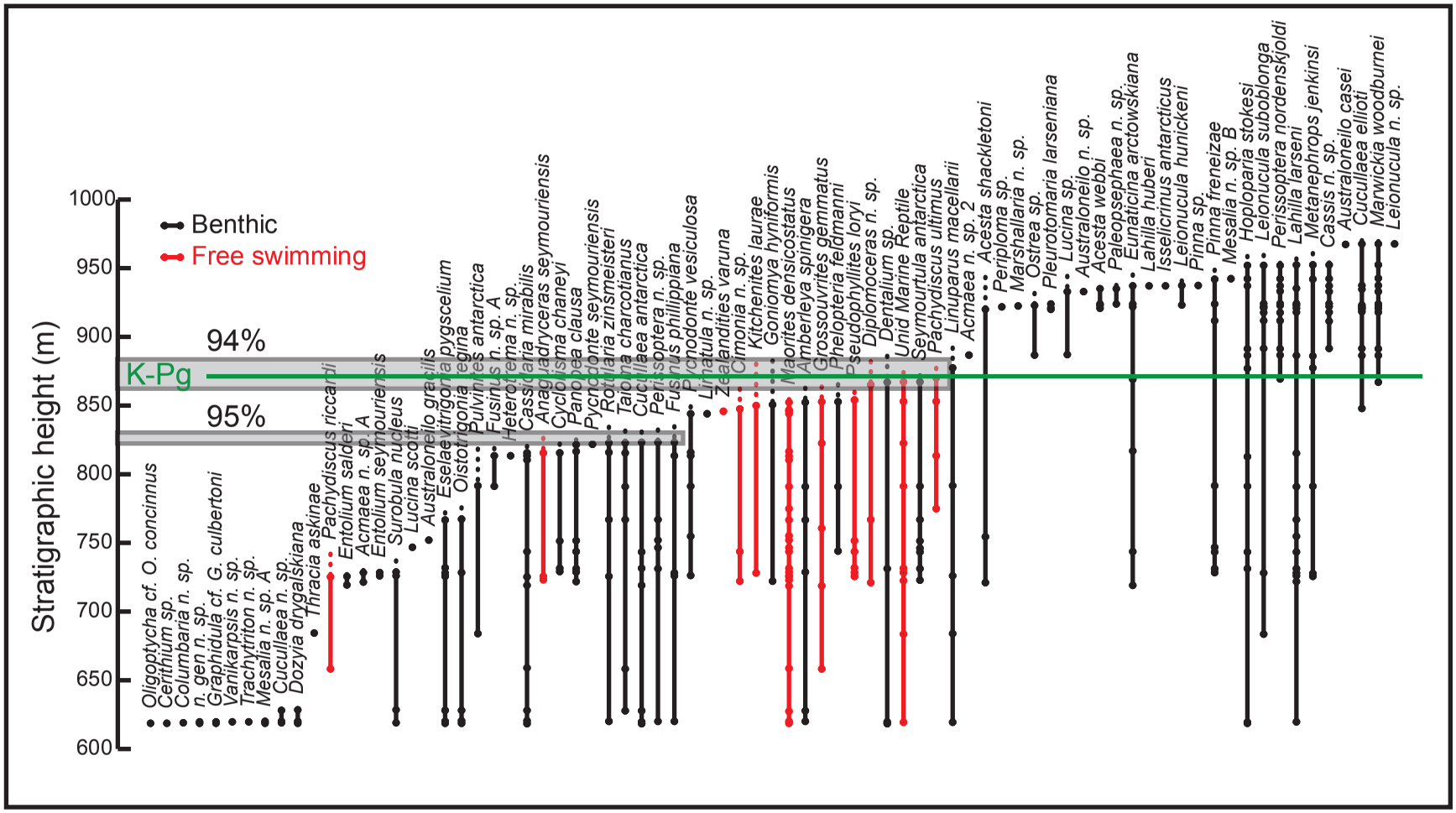

Figure 3.11. Faunal range data from Zinsmeister (Zinsmeister et al., 1989) reevaluated using modern extinction confidence interval analysis (Wang and Marshall, 2004). Individual species extinction confidence intervals (those used in the multi-species extinction analysis) are shown as dashed range extensions. Grey bars highlight multi-species extinction confidence intervals. Two extinction events were discovered to be stratigraphically resolvable, one at and one prior to the K-Pg boundary. Species with single occurrences pictured above are omitted from statistical analyses.

striking difference between these two extinctions is apparent in the fate of ammonites: only one of seven ammonites becomes extinct at the precursor extinction, whereas all six ammonites present in the latest Maastrichtian become extinct at the K-Pg boundary.

While the precursor extinction event is visible in Figure 3.11, there is a notable lack of fossil collection in the interval between the two extinction events, and the earliest extinction could plausibly be explained by artificial range terminations due to poor sampling. To test this observation, extensive collections were made during recent sampling expeditions. New fossil occurrences (n=634) were recorded and combined with species occurrences from Zinsmeister using the well-defined K-Pg boundary as a datum. While relative stratigraphic heights are well determined for a single data set (hence Figure 3.11 showing the Zinsmeister data alone), correlating two separate sections necessarily generates greater uncertainty in both species identification and stratigraphic height, particularly at greater stratigraphic distances from the K-Pg datum. Consequently, new species occurrences were only added if they were separated by greater than twenty meters stratigraphically, a very conservative approach. Several species have been renamed or combined in the past twenty years, and these changes also incorporated in the combined analysis and figure (Fig. 3.12), demonstrating the persistence of two multi-species extinction events despite thorough sampling over the previously barren interval.

Discussion

Figure 3.10 places the observed extinctions and paleotemperature record in their stratigraphic context, along with the timing of Deccan Traps flood volcanism as correlated using magnetostratigraphy (Chenet et al., 2009; Jay et al., 2009; Robinson et al., 2009). This framework reveals that warming intervals occur primarily during the phases of Deccan Traps volcanism, and the onset of the second interval is also contemporaneous with the identified precursor extinction. As discussed above, the later warming event could be subdivided into two events corresponding

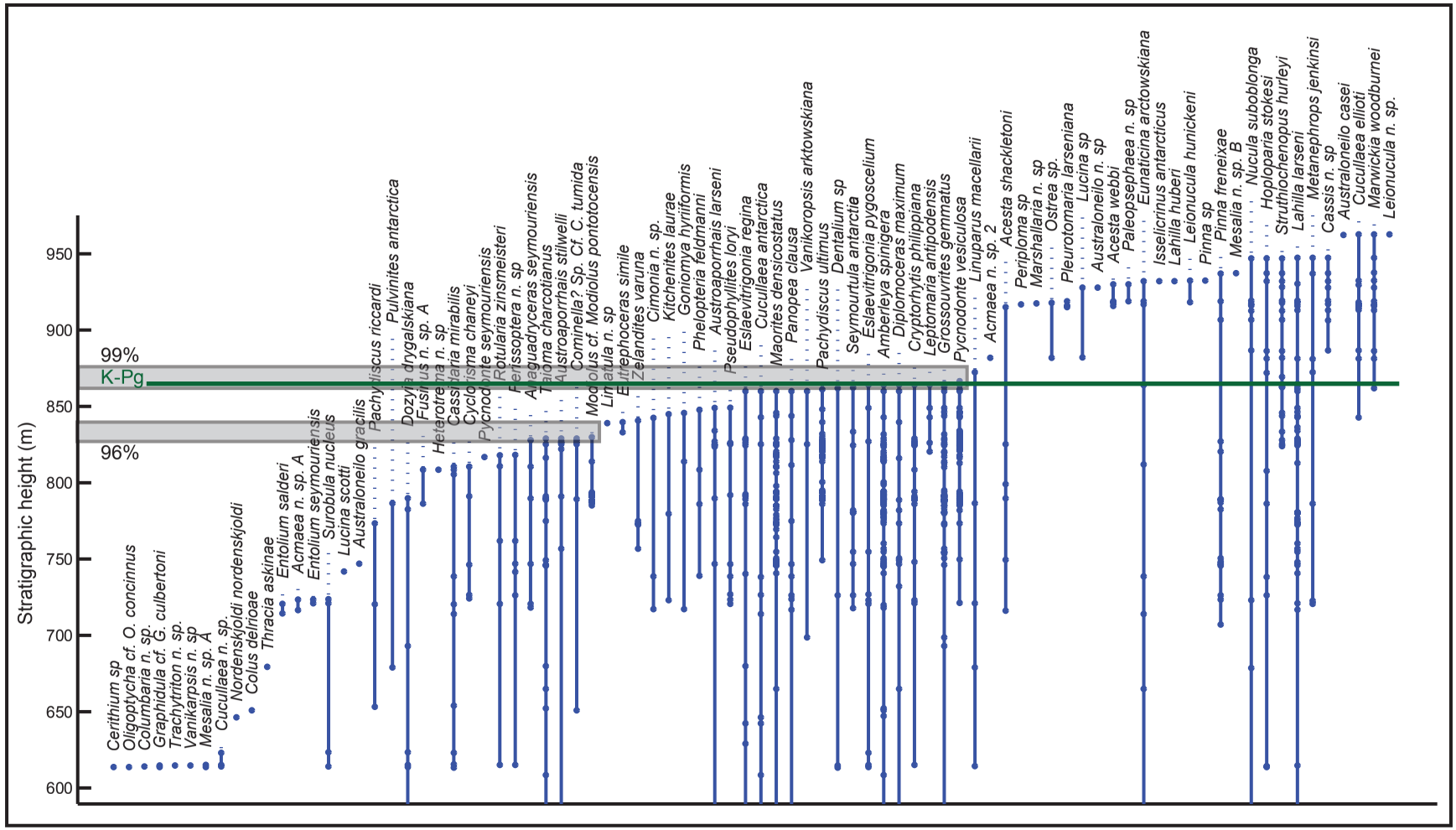

Figure 3.12. Faunal range data from Zinsmeister et al. (1989) combined with data from newly collected specimens. Correlation between the two sections was done using the well-defined K-Pg boundary layer as a datum, and species occurrences were not combined when within 20 meters of each other to conservatively underestimate the total number of horizons. Grey bars indicate extinction confidence intervals for two separate extinction events, consistent with those found from the single Zinsmeister data set.

with the two latest Deccan Traps phases. Below we evaluate both possibilities and find that both interpretations yield similar correlation coefficients.

A statistical evaluation of correlation between warming events and the timing of Deccan volcanism was performed by assigning binary values to the two variables at 100 ka intervals throughout the section as in Figure 3.10, from 68.8 Ma to 65 Ma. Each variable was assigned a value of 1 if 'active' and 0 if 'inactive' for each 100 ka interval. The timing of warming events and volcanic phases correlate with a phi correlation coefficient (φ) of 0.45, indicative of a moderately strong correlation with high statistical significance (p-value <0.01). The correlation is similar ($\varphi = 0.39$; $p<0.03$) if the diagenetically culled data set is evaluated. We were unable to perform this analysis on the extinction timing due to a lack of fossil data during the earliest warming period.

The integration of the first Upper Cretaceous magnetostratigraphy for this basin with the high resolution temperature record presented here reveals a significant destabilization in polar climate in the Late Maastrichtian caused by global warming, likely the result of Deccan volcanism. This supports the hypothesis that the primary long term effect of LIP emplacement is a global warming as a consequence of CO_2 outgassing (Wignall, 2001). Furthermore, correspondence between multi-species extinction and warming strengthen the proposed causal link between flood basalts and biotic crises (Courtillot and Renne, 2003).

Conclusion

Climatic effects on biota occur rapidly on a geologic time scale and may only be discernible in expanded sections such as those found in the James Ross Basin. In more condensed sections elsewhere, such a precursor extinction may be time-averaged with, and indistinguishable from, the boundary extinction. The preferential extinction of benthic fauna compared to nektic species during the precursor extinction, compared with primarily nektic extinction (including all ammonites) at the K-Pg boundary extinction, suggests that substantially different mechanisms were at work in

each event. Our results imply that what has been called the K-Pg mass extinction was composed of a more complicated series of separate events than any single cause can explain. Furthermore, the lack of biotic response to Deccan volcanism has been used as a reason to reject the hypothesis that large igneous provinces significantly disrupted the biosphere during the end Triassic (CAMP) and end Permian (Siberian Traps). The evidence presented here should alleviate this particular concern.

Acknowledgements

We acknowledge NSF Grants 0739541, 0739432, and PICTO 36315 and 0114 ANPCyT-DNA (Argentina). We thank two anonymous reviewers for their comments which improved the manuscript. We would also like to thank David J. Smith, Alvar Sobral, Tomás Wagener, Melissa Rider, Stian Alesandrini, John Evans, Dave Barbeau, Andrew Schauer, and Ron Sletten for assistance in the field and laboratory. Magnetostratigraphic data for this paper are available in the supplemental online material and at the MagIC portal, and the isotopic data is available as Appendix 3.2 and on the UW Isolab website (http://depts.washington.edu/isolab/data/). Fossil material is held at the University of Washington's Burke Museum of Natural History.

Chapter 4. Environmental change across a terrestrial Cretaceous-Paleogene boundary section in eastern Montana, U.S.A., constrained by carbonate clumped isotope paleothermometry (Tobin et al., 2014)

Thomas S. Tobin, Gregory P. Wilson, John M. Eiler, and Joseph H. Hartman

Abstract

The Cretaceous–Paleogene (K-Pg) mass extinction has been attributed to the impact of a large bolide at the end of the Cretaceous Period, though other potential causes have also been proposed, most notably climate change caused by Deccan Traps flood volcanism. Reconstructing paleoclimate, particularly in terrestrial settings, has been hindered by a lack of reliable proxies. The recent development of carbonate clumped isotope paleothermometry has contributed to temperature reconstructions using geochemical proxies in terrestrial settings. We employ this method, along with new stratigraphic constraints, in the Hell Creek (Cretaceous) and overlying Fort Union (Paleogene) formations to examine changes in temperature leading up to and across the K-Pg boundary. We demonstrate that ca. 66 Ma, well-preserved, aragonitic bivalves serve as suitable paleoclimate archives. Though there are limitations in the stratigraphic availability of fossil bivalves for clumped isotope analysis, we record an apparent 8 °C decrease in summer temperatures over the last 300 k.y. of the Cretaceous that corresponds broadly with patterns observed in other paleotemperature proxies. This observed decrease plausibly could be explained by an absolute temperature decrease or by other environmental stresses on the organisms, but in either case suggests changing living conditions over this interval. Previously documented declines in vertebrate and invertebrate biodiversity occur over the same stratigraphic interval at this study location. These results are consistent with published models of the end-Cretaceous mass extinction in which destabilized ecosystems become more susceptible to an abrupt event like a bolide impact.

Introduction

The relative importance of the potential causes of the Cretaceous–Paleogene (K-Pg) extinction event is the subject of intense debate (e.g. Schulte et al., 2010 and comments and reply). Although there is compelling evidence of an extraterrestrial impactor coincident with the K-Pg boundary, some hypothesize that other environmental perturbations, such as climate change, destabilized or stressed latest Cretaceous biotic communities, which became more vulnerable to the effects of a bolide impact at the K-Pg boundary in what Arens and West (2008) termed a "Press-Pulse" scenario (Arens and West, 2008; Mitchell et al., 2012; Wilson, 2005; Wilson et al., 2014). Testing the validity of the multiple-cause hypothesis is partially contingent upon determining the timing, magnitude, and rate of these perturbations over the crucial end-Cretaceous interval, and placing them in the context of well-established fossil records.

Most Cretaceous temperature estimates are from marine sections, and temperature analysis in continental environments has been limited by a lack of unambiguous proxies. Here we apply clumped isotope paleothermometry to well-preserved fossil unionid bivalves from the Hell Creek Formation (HCF) and Tullock Member of the Fort Union Formation (TUM), both of which have rich and well-studied fossil assemblages. This technique allows for the direct estimation of paleotemperature in environments where unconstrained $\delta^{18}O$ of water ($\delta^{18}O_{water}$) prohibits traditional oxygen-isotopic techniques (Eiler, 2011). A non-geochemical proxy, leaf-based paleotemperature reconstruction, has been used to document a temperature rise and fall in the ca. 300–500 k.y. immediately preceding the K-Pg boundary (Wilf et al., 2003), but the assumptions on which this method is based have been questioned (Little et al., 2010 and references therein). An independent record from clumped isotopes could improve understanding of the validity of floral proxies and climate change through this interval, as well as contributing to increased

understanding of the applicability of clumped isotopes to continental environments, which remains an open methodological question.

Abbreviated Methods

Stratigraphy- We obtained fossil shell material for this study from the HCF and TUM in central Garfield County, south of the Fort Peck Reservoir (Fig. 4.1). Stratigraphic correlation in this study area is complicated by the limited vertical exposure and lateral extent of terrestrial facies. Several previous studies have confirmed that the lithologically defined HCF-TUM contact is nearly coincident (<10 cm) with the K-Pg boundary at multiple locations using the presence of an Ir anomaly and shocked quartz (Moore et al., 2014 and references therein; more details in Appendix 4.1, and extended methods, below). We infer that the HCF-TUM contact is coeval within the limits of our field area (~8,000 km^2) and can be used as a proxy for the K-Pg boundary geochronologic datum, but we recognize that farther east the K-Pg boundary and lithologic contact can be diachronous. Using a high-resolution (±< 2 m vertical) GPS receiver, we measured the absolute elevations of the HCF-TUM contact at the localities studied above, as well as several other HCF-TUM localities as seen in Figure 4.1 (details in Appendix 4.1). The three-dimensional spatial relationship between these boundary points was analyzed, and the points were found to fit very well (R^2 = 0.999, $p < 0.001$, max error = 8m, RMSE = 3.8 m) to a simple plane with a strike/dip of 049°/0.2° SE, and described by Equation 1:

(1) $Elev_{(HT)} = (East \times -2.2947 \times 10^{-3}) + (North \times 2.6741 \times 10^{-3}) - 12435.4$

where *East* and *North* are UTM Zone 13 N coordinates, and $Elev_{(HT)}$ is the modeled height of the HCF-TUM contact at that location in meters (see extended methods). Fossil sampling localities were projected to this plane to find their stratigraphic height relative to the boundary, and thus were placed in their stratigraphic positions. A new magnetostratigraphic record from Site S in Figure 4.1 (LeCain et al., 2014) allows the assimilation of magnetic reversals into our stratigraphic framework.

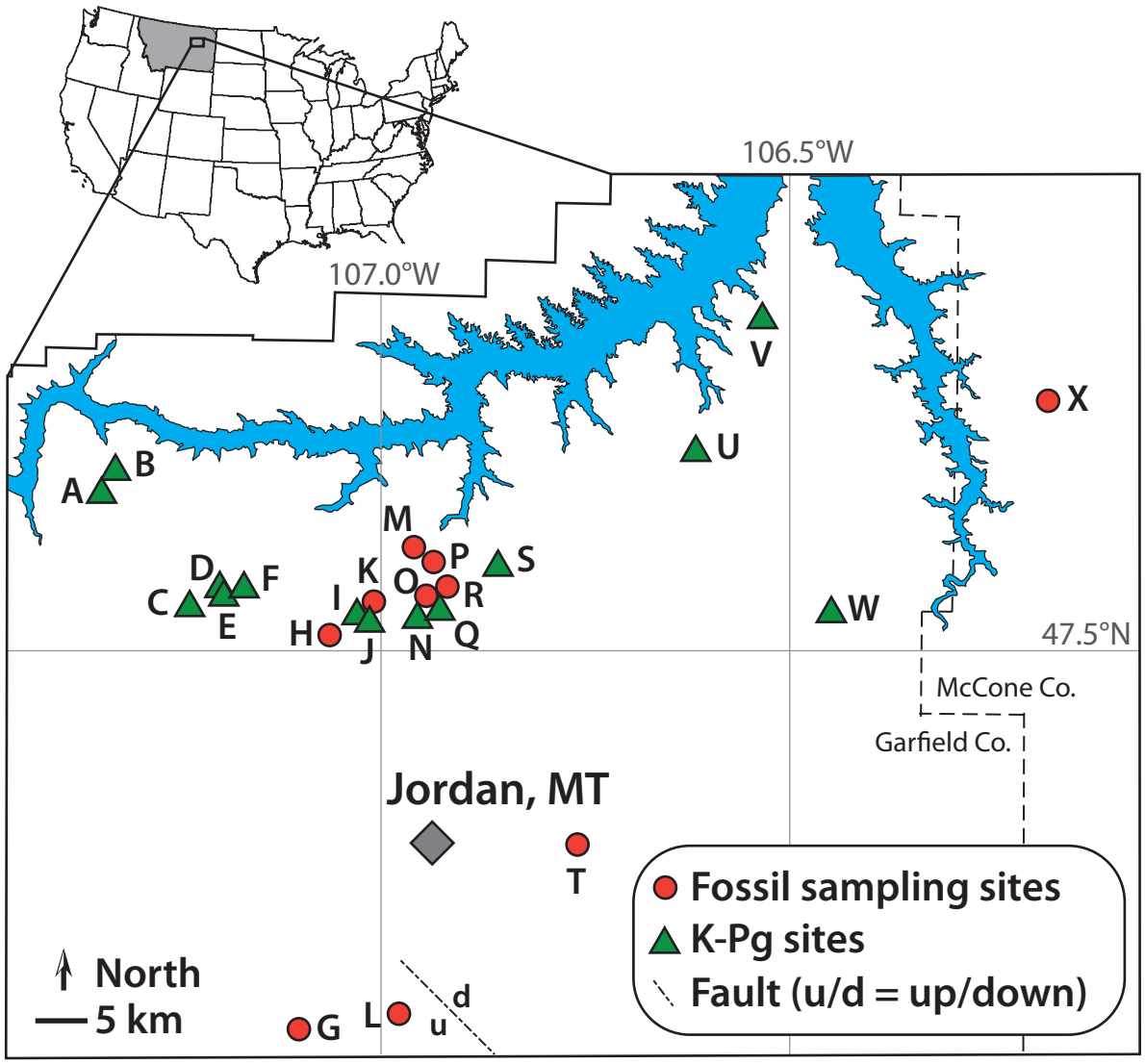

Figure 4.1. Locality map of the sampling area in Garfield and McCone counties, Montana, U.S.A., showing Fort Peck Reservoir (in blue). Triangles indicate sites of HCF-TUM boundary localities. Circles indicate mollusk fossil sites for geochemical sampling. Researchers should contact the authors for locality coordinates of the fossil sites. For other site details see Appendix 4.1.

Laboratory Methods- We collected unionid bivalve (10 localities) and gastropod (2 localities) fossils through the HCF and TUM, and we collected a carbonate vein crosscutting surrounding lithology at an additional site. To serve as a modern analog, unionids from the Amite River in Louisiana, U.S.A. were collected from a site near permanent air and water temperature recorders. Fossil shells were assessed for diagenesis using trace element concentrations (ICP-OES), X-ray diffraction (XRD), and cold cathodoluminescence microscopy. Gastropods, but not bivalves, showed indications of diagenesis, with detectable levels of calcite (XRD) and recrystallized carbonate phases (cathodoluminescence). Clumped isotope measurements were made following the methods of Huntington et al. (2009) and Passey et al. (2010), and measurements were converted to the absolute reference frame (Dennis et al., 2011) and then to temperature using the calibration from Zaarur et al. (2013 - eq. 7). Measurements and errors were derived by averaging 2–4 analyses on a shell, and averaging 3–4 shells to create a locality value. This averaging is justified here because multiple measurements from the same sites and stratigraphic horizons are consistent with random samples of a single population. See supplemental methods for a more thorough exploration of different temperature calibrations, some of which increase the magnitude of observed temperature changes due to increased Δ_{47}-temperature sensitivity.

Detailed Methods

Stratigraphy- We surveyed elevations at HCF-TUM contact localities using a high-precision Trimble 2005 GeoExplorer XT GPS receiver, and found that the contact is remarkably planar. The best-fit plane has a maximum residual of 8 m and RMSE of 3.7 m , just twice the instrumental precision of the GPS receiver (< 2 m). We used GPS receivers to acquire geographic coordinates for all fossil sampling localities, and projected those coordinates to the best-fit plane to determine the stratigraphic height of each locality relative to the HCF-TUM (≈ K-Pg boundary). These stratigraphic data were compared to previously published stratigraphic heights (Hartman, 1998; Wilson, 2005)

and geologic maps (Wilde and Bergatino, 2004a, 2004b; Wilde and Vuke, 2004a, 2004b) for compatibility. Only two sites diverged by more than 5 m from published estimates. L0010a was projected to be 10 m above the K-Pg boundary, though Hartman (1998) recorded it as 35 m above the boundary. We accept the latter value, as there is clear exposure of 20–25 m of TUM below the fossil horizon, and projection at this site requires extrapolation of the best-fit plane beyond recorded data points. A NW-SE fault in the lower center of the map offsets localities L6214/5 (Site L). Wilde and Vuke (Wilde and Vuke, 2004b) map the fault as having approximately 200 m of offset, consistent with the difference between published height estimates (Hartman, 1998) for that location and our projected height (195 m). Uncertainties on stratigraphic heights are a combination of GPS precision estimates (typically < 1.5 m) and uncertainties derived from stratigraphic projections (typically < 3.0 m). A copy of this model is available as a Matlab file (Appendix 4.2) with contained instructions that can be used to examine this surface model and find projected surface locations (and confidence intervals) for any geographical location. Details of each locality, including specific uncertainty estimates can be found in Appendix 4.1. In many cases, larger upper bounds on stratigraphic height were added to the analytical uncertainties to reflect shells being retrieved from the bottom of large channel structures that down cut into surrounding overbank deposits, and the corresponding uncertainty in the relative timing when compared to neighboring flat-lying deposits. We note that, despite large numbers of published sampling localities and considerable field exploration, bivalve fossils were absent from the lowest 30 m of the TUM.

*Laboratory Methods***-** We collected unionid bivalve fossils from ten localities in the study area with the goal of even stratigraphic sampling of the HCF and TUM, although no bivalve fossil localities are known from the lowest 30 m of the TUM. We also sampled rarer gastropod fossils from two localities and carbonate vein material from one locality. To serve as a modern analog, we collected unionid bivalves from the Amite River, near Denham Springs, Louisiana. The temperature and depositional environment at this location approximate conditions during deposition of the HCF.

Daily historical temperature records for the past 50 years are available from a USGS water-temperature monitoring station located 35 km upstream of this location and from an air temperature station located in nearby Baton Rouge, Louisiana (15 km).

We prepared three or four bivalve shells from each locality (fossil and modern) by drilling near the umbo of the shell to generate carbonate powder for analysis. The umbo is selected for two reasons, one practical, the other theoretical. Primarily the umbo serves as standardized location on each shell to minimize variations between sampled bivalves. Secondly, the umbo is selected because bivalves are likely to exhibit less seasonal bias early in their life due to the importance of constructing their initial shell for protection. Unfortunately, the results of this study revealed that seasonal bias was still present. This is particularly important because clumped isotope analysis currently requires almost two orders of magnitude more carbonate material than traditional isotopic techniques (Eiler, 2007), so our preparation technique was designed to average multiple years of growth instead of examining seasonal variability. We assessed diagenesis of visually pristine, fully aragonitic (as confirmed by XRD) material from bivalve shells using trace element concentrations (no correlations between either $\delta^{18}O$ or $\Delta 47$ with [Al], [Ba], [Fe], [Mn], [Na], [Sr] were found). Additionally, we sectioned and examined a subset of samples under cold-cathode cathodoluminescence (CL) microscopy; no bivalves were found to exhibit any signs of recrystallization. Under CL illumination, gastropod fossils showed textures and luminescence characteristic of diagenesis. Presumably recrystallized calcite was detected by XRD in primarily aragonitic gastropod sample powders, but not in primarily aragonitic bivalves.

Stable isotopic measurements were made in two batches at the California Institute of Technology (Caltech), the first in November 2010 and the second in February 2012. In both batches carbonate powders were reacted with 90 °C 100% phosphoric acid and the emitted CO_2 gas was purified through two cryogenic trap sequences separated by a He carried gas chromatograph

transit before introduction to the sample bellows of Thermo MAT 253 mass spectrometer. Measurements were interspersed with internal lab standard carbonate powders, heated gases, and in the case of the later batch, low-temperature, water-equilibrated gases. Detailed laboratory methods follow supplemental information of Passey et al. (2010)and raw mass spectrometry data was processed as in Huntington et al. (2009), modified to convert measurements to absolute reference frame (Dennis et al., 2011). Analyses (6 of 145) with Δ48 signatures indicative of methodological contamination (Δ48 anomalies) were removed from the final compilation (Huntington et al., 2009), as were samples with anomalously high Δ47 values (>1.0; n=2). Shells for which only one successful analysis (n=3) remained were excluded from the final data compilation (Appendix 4.3), but are included in the raw clumped isotope data (Appendix 4.4).

Each bivalve shell was analyzed either two or three times to generate mean shell values Δ_{47} values, which were in turn averaged to generate mean locality Δ_{47} values and uncertainty estimates. Corrected Δ_{47} values in the absolute reference frame were converted to temperature using equation 7 from Zaarur et al. (2013). Formulae from Kim et al. (2007b) and Kim and O'Neil (1997) were used to reconstruct $\delta^{18}O_{water}$ from temperature and $\delta^{18}O$ of the carbonate. The analyses and sample mean values of Δ_{47} and $\delta^{18}O_{water}$ can be found in Appendix 4.3.The net result of converting from the internal laboratory measurements to the absolute reference frame for the 2010 batch was a 1.5 °C increase in reconstructed temperature. While we use the most recent of the Δ_{47}-temperature calibrations, other recent alternative calibrations have been proposed (Eagle et al., 2013; Henkes et al., 2013; Zaarur et al., 2013, 2011). In terms of absolute temperature estimates, these calibrations agree very well around 30 °C, but all have greater temperature sensitivities than the calibration we used, and would consequently show greater temperature changes. The aragonite calibrations from Eagle et al. (2013) and Henkes et al. (2013) have temperature sensitivities greater than the Zaarur calibration. While the Zaarur calibration yielded a 8 °C temperature decline (31-23 °C) that we use in the main text, using the alternative calibrations we would reconstruct an 9 °C (34-23 °C) or a

13 °C (32-19 °C) decline using Eagle et al. (2013) or Henkes et al. (2013), respectively. We elected to use the Zaarur calibration because it is more conservative in estimated temperature changes, and the most recently published. Appendix 4.3 has the temperatures for the different calibrations identified for all analyses.

Results

Modern bivalves- We compared our results from modern unionid bivalves with instrumentally recorded water and air temperatures near their collection site (Fig. 4.2). The measured clumped isotope temperature is consistent with the mean summer temperature (May–Sept.), suggesting that the bivalves precipitate most $CaCO_3$ during summer, consistent with previous studies (Dettman et al., 1999). Several new temperature calibrations have been recently published, but they agree within error near 30 °C, so unfortunately our modern data cannot be used to discern between them (see supplemental methods for more details). This agreement suggests that controversies regarding calibrations of carbonate clumped isotope thermometry are relatively unimportant for the materials and temperature ranges relevant to this study.

Diagenesis- Figure 4.3 shows average paleotemperatures derived from Δ_{47} values and the reconstructed $\delta^{18}O_{water}$ for each locality in stratigraphic context. These data circumstantially support our direct evidence (see "Laboratory Methods,") for a lack of diagenesis in unionid bivalve fossils. First, there is no correlation between $\delta^{18}O_{water}$ and paleotemperature (Fig. 4.4). If fossils reset to higher temperature (by diffusion or recrystallization) in a closed system, the calculated $\delta^{18}O_{water}$ would correlate strongly with apparent temperature, following the slope of the carbonate-water equilibrium (e.g., Came et al., 2007). Second, the carbonate vein material records the highest temperature (45 °C) among our samples, suggesting that the fossils have been exposed to some burial depth (~ 1 km) without resetting to warmer temperatures or adopting the $\delta^{18}O_{water}$ of vein fluids. Further support is provided by the altered gastropod paleotemperatures, which are

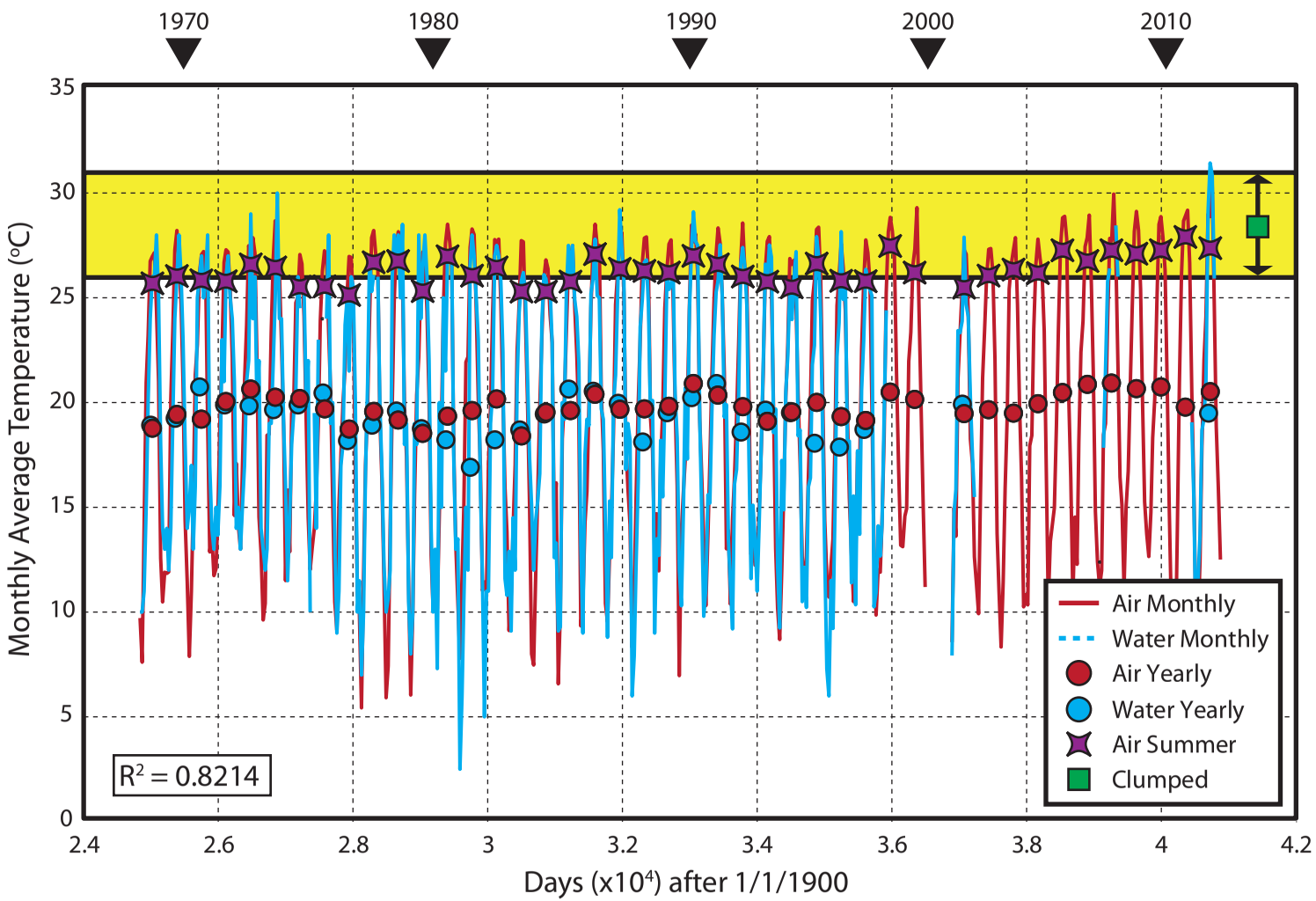

Figure 4.2. Monthly average air and water temperature records constructed from daily records for nearest monitored location to modern unionid bivalve sampling location (used as modern analog for fossil unionids). At far right: clumped isotope temperature with 95% confidence interval reconstructed for modern shells. Modern unionids grow primarily during summer months and record a summer average temperature.

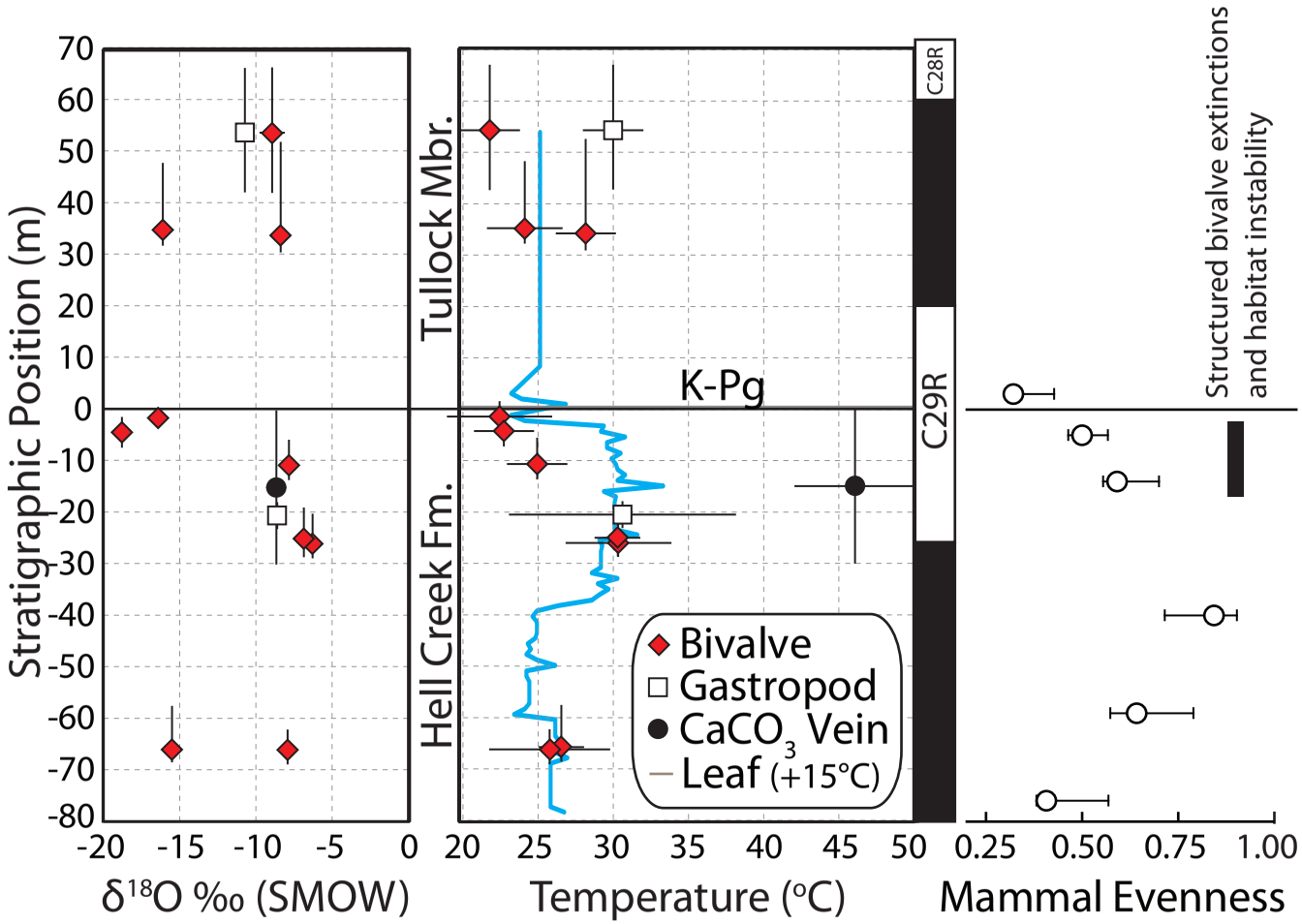

Figure 4.3. Reconstructed temperature and $\delta^{18}O_{water}$ in stratigraphic context; see full discussion in text. Note warmer recorded temperatures for diagenetically altered gastropods and carbonate vein. Measurement errors (horizontal) are 95% confidence intervals; stratigraphic errors (vertical) are calculated using geologic context and GPS receiver errors. Paleomagnetic data are from LeCain et al. (2014). Leaf range-through MAT (+15 °C to fit on scale) is from Wilf et al. (2003) using linear stretching of data set based on meters from K-Pg boundary to base C29R. Notable biological patterns from the HCF indicated at right: Open circles - mammal evenness (e^H/S), a measure of biodiversity (Wilson, 2014); Black bar – period over which documented declines in certain bivalve morphologies have been interpreted as indicative of habitat instability (Scholz and Hartman, 2007).

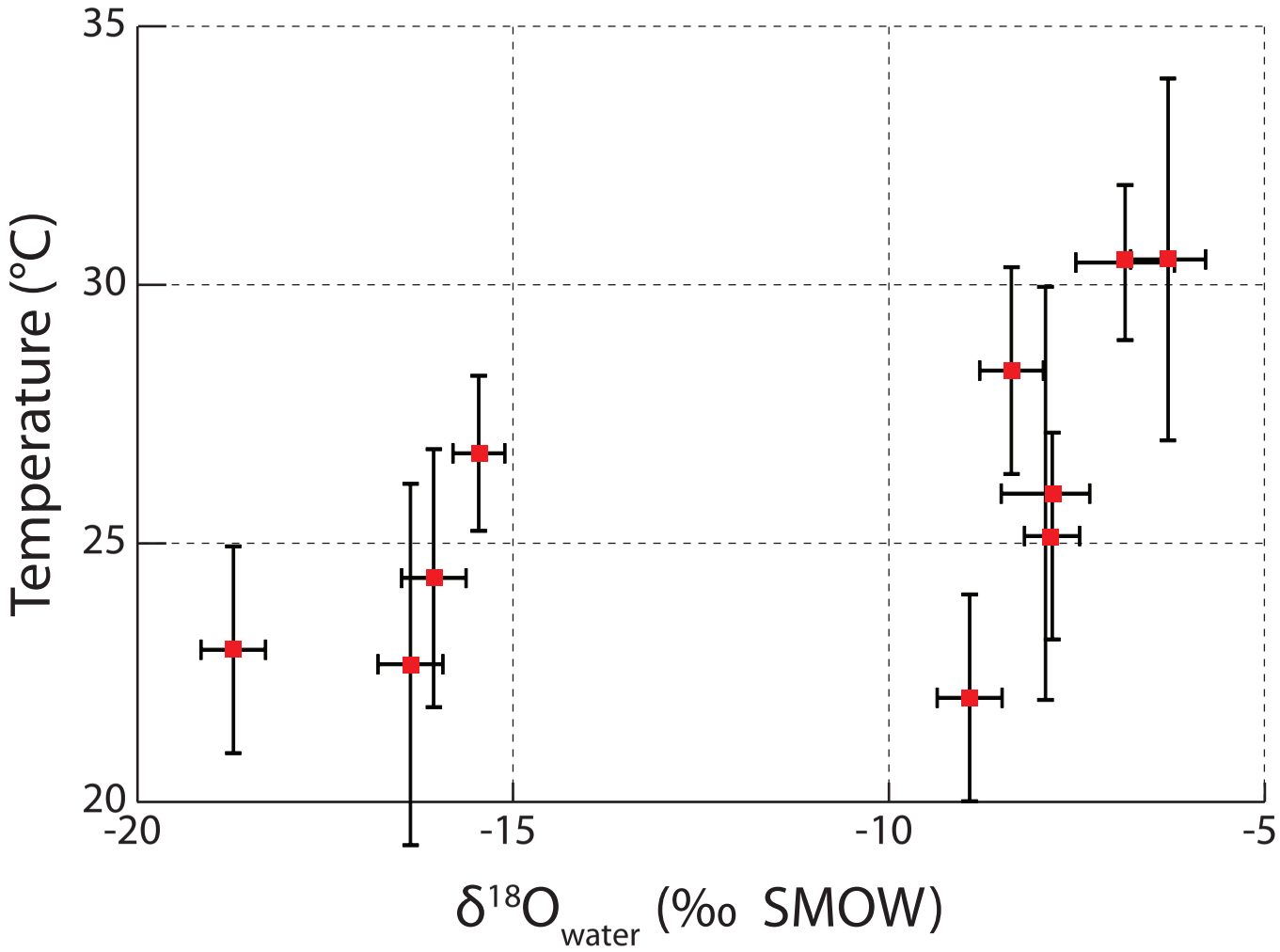

Figure 4.4. Bivalve $\delta^{18}O_{water}$ plotted against reconstructed temperature with no statistically significant relationship.

substantially warmer than bivalve paleotemperatures at the only locality where they were found together (uppermost horizon).

Bimodality of $\delta^{18}O_{water}$- We observed that the $\delta^{18}O_{water}$ was bimodally distributed, with values clustered around either -8‰ or -17‰, a pattern observed previously (Dettman and Lohmann, 2000; Fan and Dettman, 2009; Fricke et al., 2010). Several possible scenarios could explain this pattern, including differently sourced water (i.e. alpine v. lowland rainfall), different channel size, or monsoonal influence. We see no evidence in our field work for the second, and cannot differentiate between the first and last possibilities. Our primary concern is whether the different water types bias the temperature record, and there is no statistically significant relationship between temperature and $\delta^{18}O_{water}$.A *t*-test, designed to see whether two separate populations have statistically different means, was applied to the temperature values of the two $\delta^{18}O_{water}$ populations, yielding a non-statistically significant result ($p = 0.16$). There is at best a weak, non-significant, correlation ($r^2 = 0.27$, $p = 0.12$) between the two variables (Fig. 4.4) that, even if significant, would only explain 27% of the variation seen in the temperature values. Additionally, we also find for the two samples at the same stratigraphic height from different geographical localities (-66m, Fig. 4.3 of main text) that the temperatures are identical but differ in $\delta^{18}O_{water}$. The evidence suggests that there is little or no bias of temperature due to water source or channel effects.

Paleotemperature- Several features can be observed in the paleotemperature data (Appendix 4.3) despite some limitations in stratigraphic occurrences of reliable samples (Fig. 4.3). We analyzed two localities (both at 66 m), separated by a geographic distance of 2.5 km, which record nearly identical temperatures (30 °C), increasing our confidence that the temperature measurements are reliable. Temperatures at the next stratigraphically highest locality (26 m) for which we have measurements are only slightly warmer, which may indicate little paleoclimatic change over that interval. The overlying 26 m stratigraphic interval preceding the K-Pg boundary is well sampled

and shows a decrease in paleotemperature (by ~8 °C) that is statistically significant ($p < 0.005$) when compared with the null hypothesis of no temperature change over this interval. Uncertainties in our stratigraphic projection allow the initiation of this decline within either C30N or C29R, but close to the reversal, and restrict its termination to immediately below the K-Pg boundary. The interval between the C30N/C29R reversal and the K-Pg boundary represents ca. 300 k.y. (Gradstein et al., 2012) during which 80% of the Deccan Traps volume was erupted (Chenet et al., 2009). Bivalve localities in the TUM are rare and occur at the base of large, downcutting, stream-channel deposits, so their depositional ages are less well-constrained, though reconstructed temperatures are within the range observed in the HCF. The timing and nature of paleotemperature trends in the TUM are an obvious target for further testing, though aragonite bivalves are very rare or absent in much of this interval, and the depositional character of the deposits makes assigning relative stratigraphic heights difficult.

Discussion

We observed a bimodal distribution of $\delta^{18}O_{water}$, but saw no statistical correspondence between $\delta^{18}O_{water}$ and temperature in our analysis of fossil shell material (Fig. 4.4). This pattern has been previously observed (Dettman and Lohmann, 2000; Fan and Dettman, 2009), and we agree with their interpretation that the two $\delta^{18}O_{water}$ modes likely reflect different water sources supplying the area. Similar bimodality has been observed in Campanian-Maastrichtian unionid bivalves elsewhere in the Western Interior and interpreted as the result of monsoonal influence (Fricke et al., 2010). Bimodal $\delta^{18}O_{water}$ values could reflect sampling of mollusks from large versus small river channels (Fan and Dettman, 2009), but we saw no correspondence between channel size and $\delta^{18}O_{water}$. We conclude that the observed temperature changes are not biased by variations in water sources.

Dennis et al. (2013) published the only previous clumped isotope data from the HCF (Δ_{47} = 0.683 ± 0.003 (1 s.d.), n = 4), which are similar to our average clumped isotope results (Δ_{47} = 0.699 ± 0.014 (1 s.d), n = 30). Samples from Dennis et al. (2013) lack stratigraphic control beyond formational information, so it is impossible to say whether there is a real discrepancy between these two data sets or just in the location of their sampling (e.g., a single site – R – from this study has statistically identical values to those in the Dennis et al. (2013) study – Δ_{47} = 0.680 ± 0.007 (1 s.d.) n = 4). While the Δ_{47} results are comparable, Dennis et al. (2013) reconstruct temperatures that are 10 °C cooler than this study (which yields a 2.5‰ change in $\delta^{18}O_{water}$), based on "vital effect" corrections that we did not apply to our data. Given the known growth habits of unionid bivalves, we favor a summer temperature growth bias interpretation discussed above (and in supplemental text) that Dennis et al. (2013) acknowledge could also explain their "vital effect." In any event, this discrepancy does not contradict our finding of a ~8 °C temperature change through the interval sampled in this study.

Given our suggestion of a summer growth bias, the apparent pre-K-Pg cooling trend can be interpreted in two ways. A relatively parsimonious interpretation is that summer temperatures declined over this interval. Previous studies from the marine realm have recorded what apparently was a global cooling episode that followed a short-term (ca. 100–300 k.y.) warming event in the very latest Cretaceous (Li and Keller, 1998; Tobin et al., 2012). The ~8 °C decline that we observe, and the overall temperature trend, is comparable to that reported (> 5 °C, Fig. 4.3) by Wilf et al. (2003) from analysis of Hell Creek floras, but poor stratigraphic resolution in both data sets complicates comparisons in the TUM. Our absolute values are consistent with summer temperatures given the MAT and seasonality from climate models (e.g. Sellwood and Valdes, 2006).

A second environmental interpretation is also consistent with our clumped-isotopic paleotemperature record: Mean annual and seasonal temperatures could have remained constant

over the measured interval, but bivalves could have shifted the duration or timing of their growing season in response to non-temperature related environmental stresses or food availability. In this scenario, a shell sample large enough for clumped isotope analysis would record a lower average temperature by including more shell grown at lower, non-summer, temperatures. Marine bivalves have been shown to adjust growth patterns to adapt to food scarcity (Schone et al., 2005).

In either case, the recorded paleotemperature decline indicates that an environmental shift occurred during the last ca. 300 k.y. of the Cretaceous. This trend temporally correlates with declines in the biodiversity of mammalian and amphibian assemblages that occur over the same interval prior to the K-Pg mass extinction (Wilson, 2014, 2005; Wilson et al., 2014). Selective extinction of certain morphologies of unionid bivalves has also been used to infer a "major decrease in habitat stability" prior to the K-Pg boundary in the same interval (Scholz and Hartman, 2007).

Modern ecological studies demonstrate that these pre-K-Pg biodiversity drops may reflect declining population sizes, changes in community structure, and/or ecological instability and stress from environmental disturbance (Magurran, 2004). Previous studies have established that species in stressed and altered ecosystems may be more susceptible to an abrupt extinction event and have advanced the hypothesis that geologic mass extinctions may be a result of this phenomenon (e.g. Arens and West, 2008; Mitchell et al., 2012; Scheffer et al., 2001). Our evidence, correlated abiotic and biotic changes occurring immediately before a sudden, pulse extinction, is consistent with this hypothesis. However, we cannot exclude the possibility that the environmental disturbances are only coincidentally correlated in time with the mass extinction at the K-Pg boundary.

Conclusion

Here we demonstrate that Late Cretaceous freshwater bivalves can be a reliable archive for clumped isotope thermometry, though complications in potential seasonal bias remain to be determined. We document an apparent decline of ~8 °C during the Cretaceous portion of C29R that

broadly corresponds with records derived from other paleotemperature proxies. This apparent change in temperature may have stressed ecological structures and magnified the effects of the bolide impact (Arens and West, 2008; Mitchell et al., 2012), a hypothesis that is supported by biotic changes observed locally and globally in marine and terrestrial settings over the last ca. 300–500 k.y. of the Cretaceous (Gertsch et al., 2011; Samant and Mohabey, 2009; Tobin et al., 2012). While further testing of the "Press-Pulse" hypothesis is necessary, the clumped isotope data here demonstrate a changing environment over the last 300 k.y. of the Cretaceous.

Acknowledgements

The authors thank D. DeMar, Jr., L. DeBey, S. Donohue, and S. Schoepfer for assistance in the field, and W. Daniel (LSU) for collection of modern Unionidae. We also thank R. and E. Meyn, Co. and Ca. Murnion, S. Harbaugh, J. and C. McKeever, B. and J. Engdahl, and W.A. Clemens for their hospitality and guidance. We thank the C. M. Russell Wildlife Refuge, BLM, Montana Department of Natural Resources and Culture for special use permits. We thank K. Huntington and N. Kitchen for assistance and discussion. Research was supported by NSF grant 0643394, NSF IGERT, and by the University of Washington Burke Museum of Natural History and Culture, Dept. of Biology, and Dept. of Earth and Space Sciences, and Chevron.

Chapter 5. Modelling the potential effects of Deccan Traps flood basalt volcanism.

Thomas S. Tobin, Cecilia M. Bitz

Introduction

The stable isotope paleotemperature reconstructions from Seymour Island, Antarctica in Chapter 3 (Tobin et al., 2012) showed that warming intervals in the few 100 ka before and after the K-Pg boundary were temporally correlated with the timing of Deccan Traps flood basalt volcanism. Other studies from different places around the globe have found a warming event of similar timing and magnitude in the interval immediately before the boundary (Barrera and Savin, 1999; Li and Keller, 1998; Liu and Schmitt, 1996; Wilf et al., 2003). Volcanic episodes of all types are generally associated with significant carbon dioxide and sulfate emissions, which have contradictory effects on the temperature of the earth. Sulfate aerosols are effective at blocking incoming solar radiation, and cooling the earth, though their impact is generally limited to within a few years of the end of emissions. In contrast, emitted CO_2 will trap more heat by increasing the greenhouse effect, and these effects are generally thought to diminish over the course of thousands to tens of thousands of years after emission ceases (Archer and Brovkin, 2008).

As part of an astrobiology research rotation with Dr. Cecilia Bitz I wanted to assess the plausibility of the CO_2 emissions from Deccan traps volcanism being sufficient to generate the warming observed by the studies mentioned above. Additionally, the research rotation was an opportunity for me to learn some basic skills outside of my discipline, as I was previously unfamiliar with modelling. We chose to focus on modelling the effects of CO_2 for three reasons: first, because the patterns we observe from paleotemperature proxies indicate warming; second, because the effects of sulfate aerosols, even if profound, would likely be too short lived to be discoverable in the geologic record (though see Vellekoop et al., 2014); third, because the modelling

of sulfate aerosols is extremely complex computationally and is currently not well understood. Due to the time scales involved, a basic box model for the earth was used, and may in fact be the most appropriate choice given that short term complexity is unlikely to be verifiable with paleotemperature proxies. We employed a model known as GEOCARB III, which was originally developed by Berner (Berner and Kothavala, 2001; Berner, 1994). It does not involve the additional sulfur modeling complexities that were later introduced to the model (Berner, 2006).

A 'descendent' of GEOCARB III, called GEOCYC, was developed by Archer et al. (2009) and compared well with other significantly more complex models. At geologically important time scales (ie. greater than 1-10ka), this model would appear sufficient for understanding the magnitude and duration of CO_2 emission effects on global temperature. The model code was made available to Dr. Bitz and me by Dr. Archer, and the front end is available online for public use in modelling the effects of fossil fuel emissions (forecast.uchicago.edu). The model was coded and provided to us in FORTRAN, and converted to MatLab by Dr. Bitz, as the increased speed facilitated by FORTRAN was unnecessary given the simplicity of the code. I am also familiar with MatLab, but not with FORTRAN, and was thus able to better understand the code.

The code initially had little to no commenting, and I worked to comment the code to facilitate my understanding of how it functioned. As a conversion from FORTRAN, the code needed aesthetic and functional tweaking before use; additionally, I added comments citing the source of almost all of the formulae and constants, though in a few places I was unable to locate where some lines had originated from.

Model Basics

GEOCARB III (as provided to us by Dr. Archer) was originally configured to model the effects of anthropogenic climate change by introducing a sudden large increase in CO_2 over pre-industrial levels, which was the then allowed to decay away. Carbon is introduced to the

atmosphere continually at low levels by volcanic emission, and is removed from the atmosphere by both weathering of rock material and direct exchange with the ocean. The exchange of carbon species in the ocean dissolved inorganic carbon (DIC) pool is modelled, and carbon is eventually removed from the system by incorporation into calcium carbonate and burial.

In more detail, the code loops through user defined time steps, modifying the carbon in the atmospheric and oceanic reservoirs. The ocean reservoir is further divided into inorganic carbon species of CO_2 (aq), HCO_3^-, and CO_3^{2-}. Ocean chemistry is modeled in a subroutine which uses inputs of CO_2 concentration and temperature to calculate the pCO_2 and concentration of CO_3, further employing another subroutine which handles most of the alkalinity and other ocean chemistry calculations using equations based on Peng et al. (1987). Each time step calculates the ocean carbon inventory as the previous carbon inventory plus inputs from carbonate and silicate weathering, minus the burial of inorganic carbon and gas exchange with the ocean (not necessarily positive). The atmospheric inventory is calculated similarly, by adding gas exchange with the ocean and volcanic CO_2 emissions, and subtracting weathering drawdown by silicate weathering.

Model Modifications

Many modifications were necessary to employ this model in Cretaceous conditions, and to handle more complex emissions scenarios. Since our initial work with this model, some of these changes can now be made on the website interface. It was necessary to change some basic constants with the model to better represent the latest Cretaceous, a much warmer time on earth than today. The solar constant was tweaked to reflect the increasing radiation from the sun over time, which creates a very slight cooling effect. The area and latitudinal position of exposed land was also different in the Cretaceous due to plate movement and a lack of polar ice caps. The fraction of exposed land was calculated as 94.75% of the current exposed land area using equal area projections of end Cretaceous paleogeography. A similar analysis conducted by Dr. Bitz caused us to

change the mean latitude of continental area from 30° N (modern) to 10 °N (Cretaceous). These two changes have opposite effects on temperature; lower land area will reduce the ability of weathering to remove CO_2 from the atmosphere, but having more land in equatorial regions will increase weathering. Neither were substantial drivers of our end results. We also changed an additional parameter from Berner and Kothavala (2001) termed 'RUN' which reflects the relationship between weathering and temperature differing between overall cold earth climates (modern - 0.045) and warm climates (like the Cretaceous - 0.025). Finally, we found that code as used had a formula that related CO_2 and weathering that was outdated and referred to weathering before the evolution of vascular plants, and we updated to a newer formula.

More important to our modelling efforts were changes to allow for more complex volcanic emission scenarios, as flood basalt style volcanism has substantial stochasticity and uncertainty in how it develops (Chenet et al., 2009, 2008, 2007; Jay and Widdowson, 2008; Jay et al., 2009; Self et al., 2006). The abrupt CO_2 spike from the original model was removed, and the constant background CO_2 emissions from volcanism were modified. Some code was added to allow for several parameters of these emissions to be modified (see Fig. 5.1). The total duration and volume of CO_2 emission are variable, as are the number and duration of individual emission events (eruptions or flows) over the course of the total emission. These modifications are necessary as some studies have suggested that the intervals between individual eruptions would be sufficient for the CO_2 in the atmosphere to return to background levels prior to the next eruption (Self et al., 2006).

A final modification was made to create a background, or starting climate, that is comparable to our understanding of the Cretaceous. As the model is at a presumed steady state for the pre-industrial parameters, I allowed the model to spin up from this state to a background Cretaceous state. Though models have suggested atmospheric pCO_2 ranges from 400-1300 ppm, the

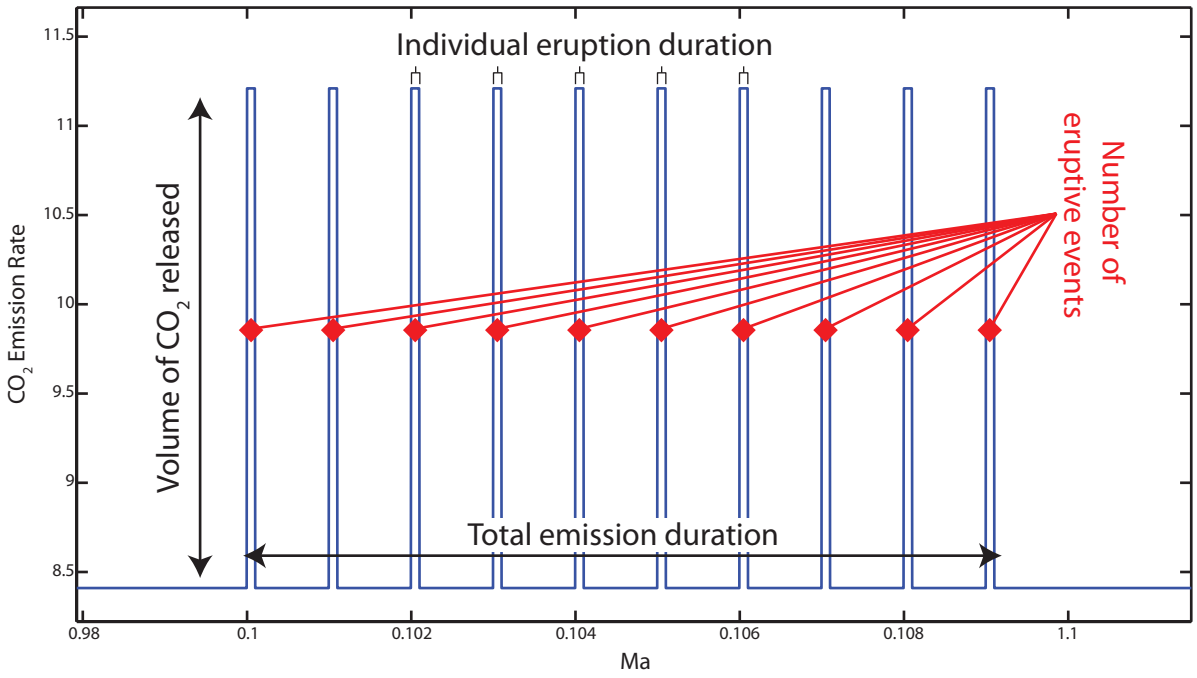

Figure 5.1. Volcanic CO_2 emission parameters that are variable in our modified GEOCARB model. The volume of CO_2 released in an individual emission is a factor of the tother modifiable parameters.

best available proxy data for this time period yields values around 450 ppm (Beerling et al., 2002; Royer et al., 2007). A Cretaceous background pCO_2 is achieved by modifying the baseline volcanic emission rate until it stabilizes at 450 ppm for the Cretaceous starting parameters. The duration of the model was also extended greatly to allow adequate time for equilibrium to be reached before Deccan Traps perturbations are added.

Model Sensitivity

Many parameters (described above), were changed to create Cretaceous starting conditions. These changes did not seem to have a significant effects on the end results, as in many cases the changes operated in opposite directions, somewhat negating their effects. The model is sensitive to the starting Cretaceous CO_2 value (see above for background starting condition), as temperature is non-linear with CO_2 (We used the provided model climate sensitivity of 3 °C for a doubling of CO_2, which corresponds well with IPCC AR4 and AR5 estimates). All the following tests are conducted with starting conditions as described above, with initial CO_2 at 450 ppm and a corresponding mean global temperature of 17 °C, in keeping with what we feel are the best CO_2 proxies employed near the K-Pg boundary (Beerling et al., 2002).

All of the parameters that were coded for adjustment of volcanic emissions (described in model modifications, above) were tested to explore their importance and potential detectability in the stratigraphic record. It was found that the number and duration of individual eruptive events, or flows, did not alter the effects on global pCO_2 and temperature when the volume of CO_2 and total eruptive duration were controlled (Fig. 5.2). Smaller numbers of flows created very short term temperature spikes that may affect biological communities, but would be too short to capture in the stratigraphic record. Similarly, the total duration of CO_2 emission was not substantially important except at very short durations (Fig. 5.3). Restricting the emission duration to 10 ka is sufficient to generate a greater temperature increase than 100 ka, but such a condensed duration is probably

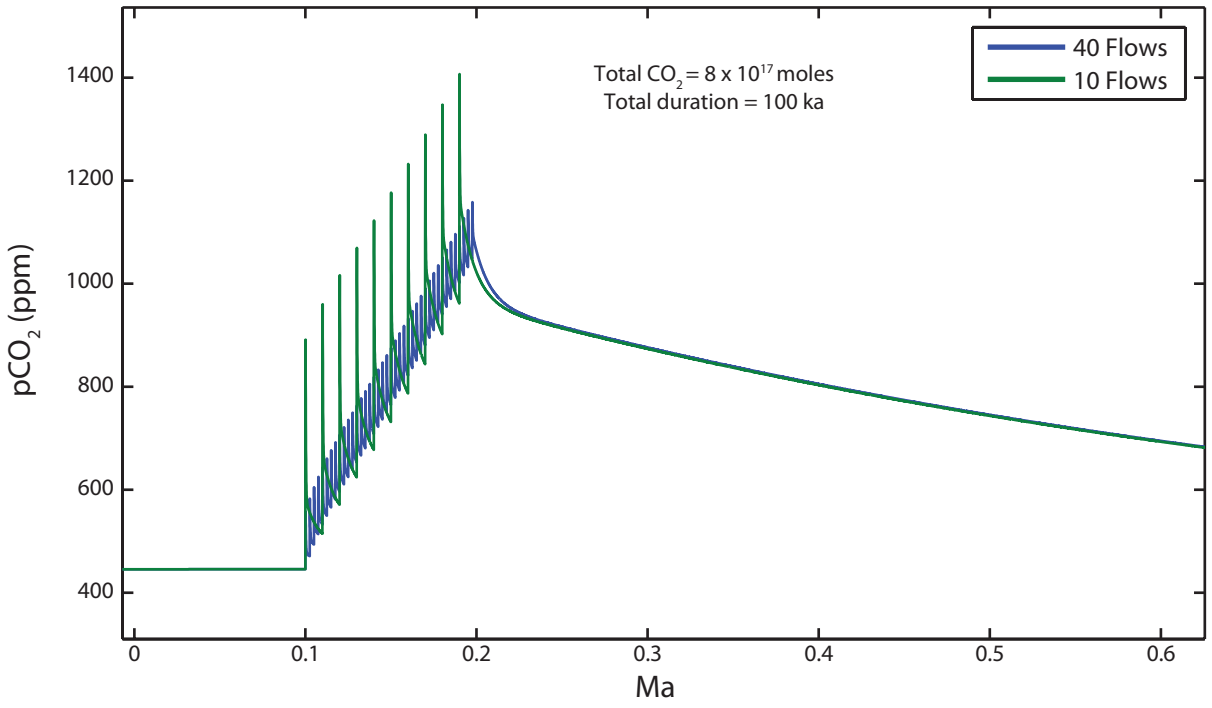

Figure 5.2. Sensitivity test for number of individual eruptive events (or flows) with total CO_2 and total emission duration held constant. Patterns are indistinguishable on all but shortest time scales, below likely threshold for discovery in geologic record.

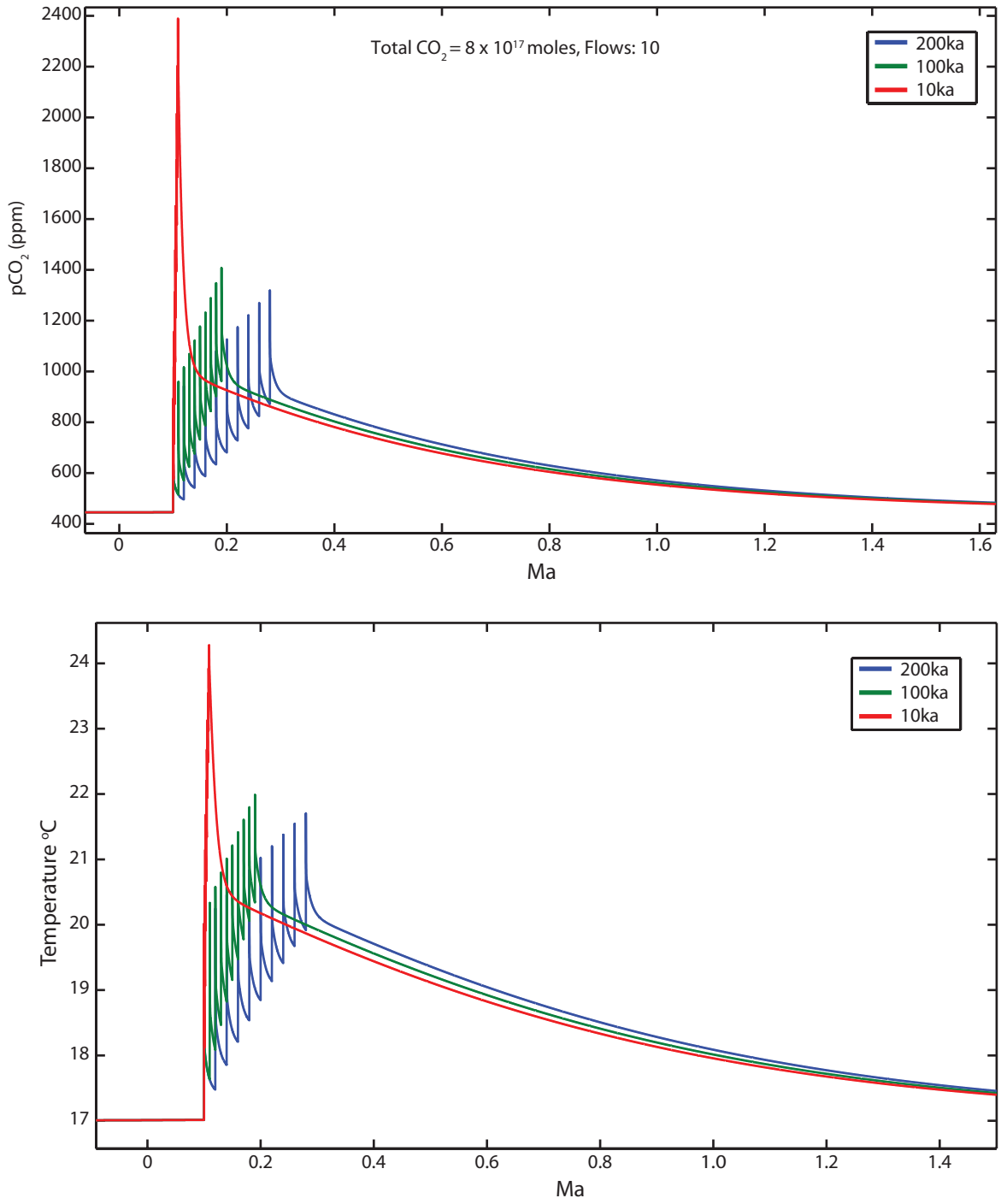

Figure 5.3. Sensitivity test for total duration of volcanic event for between 10 and 200 ka with total volume of CO_2 and number of eruptive events held constant. Modelled CO_2 concentrations (top) and global average temperature (bottom). Patterns are very simlar after 100 ka from emission start, and are almost indistinguishable after all emission in each scenario has ended.

unrealistically short. Even then the duration over which differences occur would be challenging to resolve with paleotemperature proxies.

However, the total volume of CO_2 emitted was found to be a very important variable. Estimating the volume of CO_2 released from the Deccan Traps is challenging due to a number of factors, the two most important of which are estimating the original un-eroded or un-exposed basalt volume, and estimating the original CO_2 percent by weight in the lava. Published CO_2 releases range over almost two orders of magnitude (Chenet et al., 2009; Javoy and Michard, 1989; Self et al., 2006). The largest of these volumes produces global warming of about 7°C, much higher than any paleotemperature proxy data would suggest, while the lowest volumes produce less than 0.25°C of warming (Fig. 5.4). The warming observed in Tobin et al. (2012) was 2-7°C (with uncertainties) at a high latitude location for each phase of Deccan volcanism. Given the increased temperature sensitivity of polar locations to overall global temperature change (Holland and Bitz, 2003), the Deccan traps are at least plausibly capable of generating the warming event recorded, but this plausibility hinges strongly on the published estimates for released CO_2 volumes.

Model Comparison

This model compares reasonably well with similar models. When compared with other direct attempts to model Deccan climate (Caldeira and Rampino, 1990a, 1990b), our model generates the same order of magnitude increases in atmospheric CO_2 given the same emission scenarios, as well as similar CO_2 decay rates. Had these studies employed our model they would have reached similar conclusions. Additionally, this model (when configured for the right initial conditions) also generates similar results to the more complex carbon cycle model employed by Walker and Kasting (1992) to model modern fossil fuel emissions. This in particular increases my confidence in this simpler model, as does the comparison made by Archer et al. (2009) demonstrating that on timescales that are potentially useful to geologists (10 ka) the unmodified

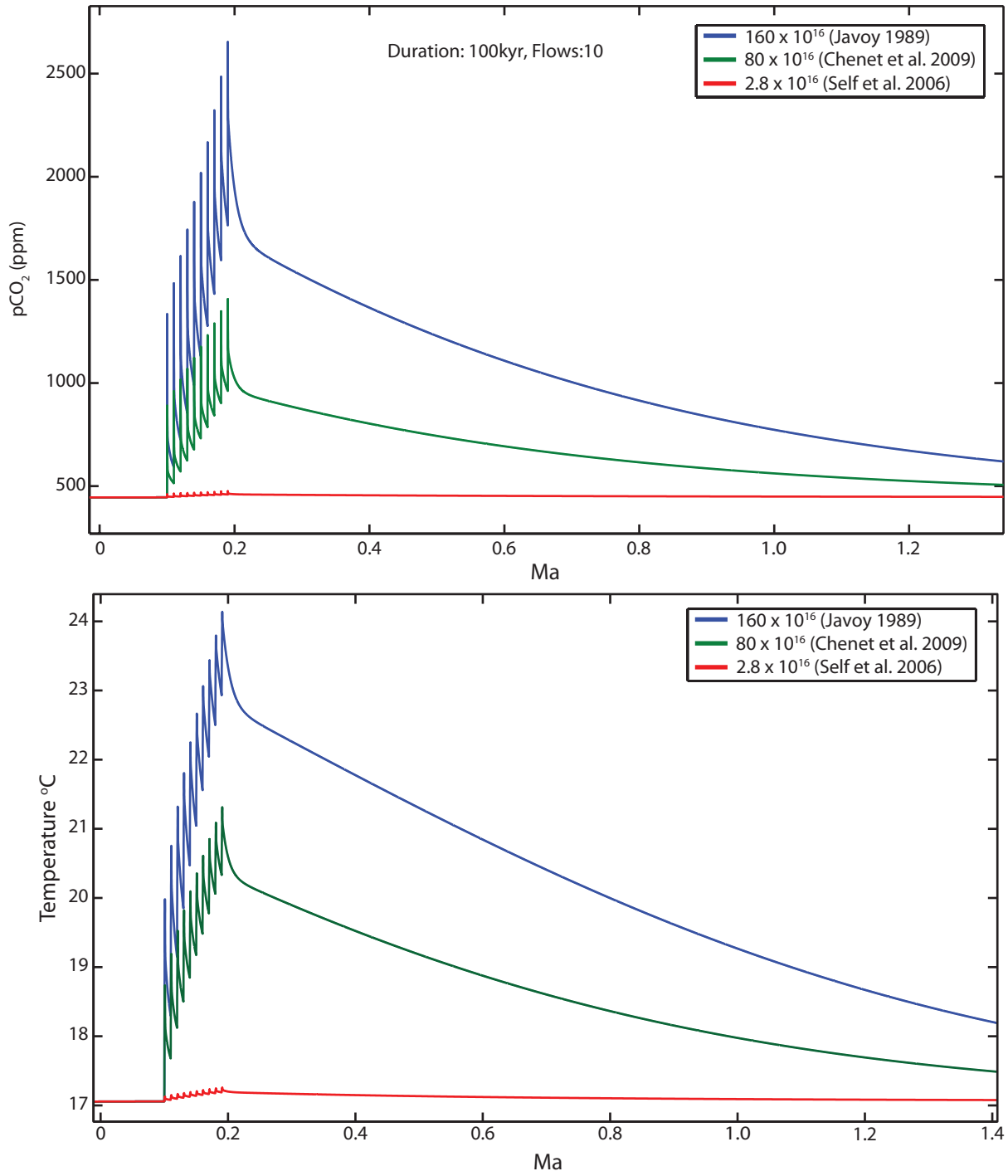

Figure 5.4. Model sensitivity test to published estimates of CO_2 release from Deccan traps volcanism with total duration and number of eruptive episodes held constant. Range of published values result in negligible to severe warming, and this uncertainty is the primary uncertainty in any temperature increase. Published high latitude warming estimates of 4-5°C (Tobin et al. 2012) are consistent with a global temperature increase of 2 °C assuming polar amplification (Holland and Bitz 2003).

GEOCARB model compares well with much more complex general circulation models. However, it would be preferable in the future to employ more complex models, particularly general circulation models, to examine finer spatial scales. Given the potential differences we observe between Antarctica and North America in Chapters 3 and 4, it would be valuable to know if such differences are compatible with a single warming event being different in either terrestrial or marine settings.

Conclusion and Future Work

Despite decades of study, there is still a considerable amount of research that needs to be completed on mass extinctions in general, and the K-Pg mass extinction specifically. This dissertation has helped illuminate some of the paleoclimatic conditions that are changing around the end Cretaceous extinction, which appear to be correlated with paleobiological disturbances (Chapters 3 and 4). Chapter 2 has potentially shed some light on why ammonites, which were so abundant and diverse prior to the end Cretaceous, were completely exterminated when other less common but morphologically similar groups, like *Nautilus*, survived the extinction. This work, like much scientific research, has also led to further questions.

It is difficult to compare the two K-Pg temperature records (Chapter 3 and 4) with each other. Given the stratigraphic uncertainties that are unavoidable in the Hell Creek area, it is unlikely that these issues will ever fully be resolved using just these field sites. We cannot currently determine if the cooling trend observed over the last 25 meters of the Cretaceous in Montana is equivalent to the entire period of warming and subsequent cooling on Seymour Island, in which case the temperature records are contradictory. It is also possible that the cooling in Montana is just capturing the same cooling, post-warming event, than that observed in Seymour Island. If these records are contradictory, they could both may still be correct for their local area, as the local responses to global climatic shifts are not necessarily identical. Future high resolution studies of other terrestrial and marine depositional environments with more global spatial coverage would be ideal, though areas where simultaneous detailed geochemical and paleobiological studies are possible are not common.

The advent and application of clumped isotope paleothermometry may also allow other terrestrial sites to produce temperature records, but additional and more robust geochemical reservoirs would broaden the potential areas in which this method can be applied. I am currently

reworking an NSF proposal to investigate gar (ganoid) scales as one potential target. Ganoid scales are made of apatite, into which minor amounts of carbonate substitute, and can be analyzed using clumped isotopic techniques. This approach was pioneered on apatite in teeth material (REF Eagle11,12) to look at animal body temperature. Fish like gar, however, will preserve the water temperature. Gar scales can be very common in the vertebrate record, as each organism will produce hundreds, and they have limited paleobiological value once the presence of gar has been noted. As apatite is a very robust mineral, these fossils have the potential to allow more reliable and more common paleotemperature estimates to be made, providing the proxy relationship can be established.

Detailed isotopic sampling of single fossil samples may help to solve some of the questions arising from Chapters 2 and 4. In finding the $\delta^{13}C$ anomaly in ammonites, one potential cause of the pattern might be that ammonites are older than bivalves. Though many ammonite shells are too thin or damaged to generate an ontogenetic series of samples, some could be sampled, and I hope to soon investigate whether ammonites start at similar $\delta^{13}C$ values to the benthic mollusks, or whether they spend their whole life fractionating carbon differently. If it is their whole life, it would support the hypothesis that a more active metabolism is responsible for lower $\delta^{13}C$ values, while an ontogenetic decrease would suggest it more likely a consequence of body size and/or age. Detailed sampling can also help resolve one of the questions raised in Chapter 4, which is whether the decrease in temperature observed is a consequence of a true climatic temperature shift, or of a change in the growth season(s) of the mussels. We may be able to see if different portions of the seasonal cycle are present in the cold and warm temperature mussels.

While not specific to the K-Pg boundary, isotopic study of other ammonite populations can be used as another test of the hypothesis outlined in Chapter 2, that ammonites are incorporating increased respired CO_2 due to active swimming habits. There are a range of ammonite

morphologies, some of which are interpreted as active swimming, others as floating filter feeders. If a sufficiently diverse assemblage of likely coeval deposition can be found, I hope to complete a comparative study of $\delta^{13}C$ and morphology, ideally in conjunction with the ontogenetic sampling described above. I hope to continue to advance the scientific understanding of both the causes and effects of the K-Pg extinction, and if these methods continue to be successful to apply them to other mass extinctions.

References

Alberti, M., Fürsich, F.T., Pandey, D.K., 2012. The Oxfordian stable isotope record (δ18O, δ13C) of belemnites, brachiopods, and oysters from the Kachchh Basin (western India) and its potential for palaeoecologic, palaeoclimatic, and palaeogeographic reconstructions. Palaeogeogr. Palaeoclimatol. Palaeoecol. 344-345, 49–68.

Altman, D.G., Bland, J.M., 2005. Standard deviations and standard errors. Br. Med. J. 331, 903.

Alvarez, L.W., Alvarez, W., Asaro, F., Michel, H.V., 1980. Extraterrestrial cause for the Cretaceous-Tertiary extinction. Science 208, 1095.

Alvarez, W., 2003. Comparing the evidence relevant to impact and flood basalt at times of major mass extinctions. Astrobiology 3, 153–161.

Alvarez, W., Arthur, M.A., Fischer, A.G., Lowrie, W., Napoleone, G., Silva, I.P., Roggenthen, W.M., 1977. Upper Cretaceous–Paleocene magnetic stratigraphy at Gubbio, Italy V. Type section for the Late Cretaceous-Paleocene geomagnetic reversal time scale. Geol. Soc. Am. Bull. 88, 383.

Archer, D., Brovkin, V., 2008. The millennial atmospheric lifetime of anthropogenic CO2. Clim. Change 90, 283–297.

Archer, D., Eby, M., Brovkin, V., Ridgwell, A., Cao, L., Mikolajewicz, U., Caldeira, K., Matsumoto, K., Munhoven, G., Montenegro, A., Tokos, K., 2009. Atmospheric Lifetime of Fossil Fuel Carbon Dioxide. Annu. Rev. Earth Planet. Sci. 37, 117–134.

Archibald, J.D., Clemens, W.A., Padian, K., Rowe, T., Macleod, N., Barrett, P.M., Gale, A., Holroyd, P., Sues, H.D., Arens, N.C., Horner, J.R., Wilson, G.P., Goodwin, M.B., Brochu, C.A., Lofgren, D.L., Hurlbert, S.H., Hartman, J.H., Ebreth, D.A., Wignall, P.B., Currie, P.J., Weil, A., Prasad, G.V.R., Dingus, L., Courtillot, V., Milner, A., Milner, A., Bajpai, S., Ward, D.J., Sahni, A., 2010. Cretaceous Extinctions: Multiple Causes. Science 328, 973.

Arens, N.C., West, I.D., 2008. Press-pulse: a general theory of mass extinction? Paleobiology 34, 456–471.

Auclair, A.C., Lecuyer, C., Bucher, H., Sheppard, S.M.F., 2004. Carbon and oxygen isotope composition of Nautilus macromphalus: a record of thermocline waters off New Caledonia. Chem. Geol. 207, 91–100.

Banner, J.L., Hanson, G.N., 1990. Calculation of simultaneous isotopic and trace element variations during water-rock interaction with applications to carbonate diagenesis. Geochim. Cosmochim. Acta 54, 3123–3137.

Barrera, E., 1994. Global environmental changes preceding the Cretaceous-Tertiary boundary: Early-late Maastrichtian transition. Geology 22, 877.

Barrera, E., Huber, B.T., Savin, S.M., Webb, P.-N., 1987. Antarctic Marine Temperatures: Late Campanian through Early Paleocene. Paleoceanography 2, 21–47.

Barrera, E., Savin, S.M., 1999. Evolution of late Campanian-Maastrichtian marine climates and oceans. Geol. Soc. Am. Spec. Pap. 332, 245–282.

Becker, L., Poreda, R.J., Hunt, A.G., Bunch, T.E., Rampino, M., 2001. Impact Event at the Permian-Triassic Boundary: Evidence from Extraterrestrial Noble Gases in Fullerenes. Science 291, 1530–1533.

Beerling, D.J., Lomax, B.H., Royer, D.L., Upchurch, G.R., Kump, L.R., 2002. An atmospheric pCO2 reconstruction across the Cretaceous-Tertiary boundary from leaf megafossils. Proc. Natl. Acad. Sci. U. S. A. 99, 7836.

Berner, R.A., 1994. GEOCARB II; a revised model of atmospheric CO 2 over Phanerozoic time. Am. J. Sci. 294, 56.

Berner, R.A., 2006. Inclusion of the weathering of volcanic rocks in the GEOCARBSULF model. Am. J. Sci. 306, 295–302.

Berner, R.A., Kothavala, Z., 2001. GEOCARB III: A revised model of atmospheric CO2 over Phanerozoic time. Am. J. Sci. 301, 182–204.

Boutilier, R.G., West, T.G., Pogson, G.H., Mesa, K.A., Wells, J., Wells, M.J., 1996. Nautilus and the art of metabolic maintenance. Nature 382, 534–536.

Bowman, V.C., Francis, J.E., Riding, J.B., Hunter, S.J., Haywood, A.M., 2012. A latest Cretaceous to earliest Paleogene dinoflagellate cyst zonation of Antarctica, and implications for phytoprovincialism in the high southern latitudes. Rev. Palaeobot. Palynol.

Brand, U., Morrison, J.O., 1987. PALEOSCENE# 6. Biogeochemistry of Fossil Marine Invertebrates. Geosci. Can. 14.

Caldeira, K.G., Rampino, M.R., 1990a. Carbon dioxide emissions from Deccan volcanism and a K/T boundary greenhouse effect. Geophys. Res. Lett. 17, 1299–1302.

Caldeira, K.G., Rampino, M.R., 1990b. Deccan volcanism, greenhouse warming, and the Cretaceous/Tertiary boundary. Geol. Soc. Am. Spec. Pap. 247, 117–123.

Came, R.E., Eiler, J.M., Veizer, J., Azmy, K., Brand, U., Weidman, C.R., 2007. Coupling of surface temperatures and atmospheric CO2 concentrations during the Palaeozoic Era. Nature 449, 198–201.

Chenet, A.L., Courtillot, V., Fluteau, F., Gérard, M., Quidelleur, X., Khadri, S.F.R., Subbarao, K.V., Thordarson, T., 2009. Determination of rapid Deccan eruptions across the Cretaceous-Tertiary boundary using paleomagnetic secular variation: 2. Constraints from analysis of eight new sections and synthesis for a 3500-m-thick composite section. J. Geophys. Res. 114, B06103.

Chenet, A.L., Fluteau, F., Courtillot, V.E., Gerard, M., Subbarao, K.V., 2008. Determination of rapid Deccan eruptions across the Cretaceous-Tertiary boundary using paleomagnetic secular varation: Results from a 1200-m-thick section in the Mahabaleshwar escarpment. J. Geophys. Res. 113.

Chenet, A.L., Quidelleur, X., Fluteau, F., Courtillot, V., Bajpai, S., 2007. 40K-40Ar dating of the Main Deccan large igneous province: Further evidence of KTB age and short duration. Earth Planet. Sci. Lett. 263, 1–15.

Cisowski, S., 1981. Interacting vs. non-interacting single domain behavior in natural and synthetic samples. Phys. Earth Planet. Inter. 26, 56–62.

Coplen, T.B., Kendall, C., Hopple, J., 1983. Comparison of stable isotope reference samples. Nature 302, 236–238.

Correa, M.L., Montagna, P., Vendrell-Simon, B., McCulloch, M., Taviani, M., 2010. Stable isotopes (d18O and d13C), trace and minor element compositions of Recent scleractinians and Last Glacial bivalves at the Santa Maria di Leuca deep-water coral province, Ionian Sea. Deep-Sea Reasearch II 57, 471–486.

Courtillot, V.E., Fluteau, F., 2010. Cretacous Extinctions: The Volcanic Hypothesis. Science 328, 973–974.

Courtillot, V.E., Renne, P.R., 2003. On the ages of flood basalt events. Geodynamics 335, 113–140.

Crame, J.A., Francis, J.E., Cantrill, D.J., Pirrie, D., 2004. Maastrichtian stratigraphy of Antarctica. Cretac. Res. 25, 411–423.

Crocker, K.C., Deniro, M.J., Ward, P.D., 1985. Stable isotopic investigations of early development in extant and fossil chambered cephalopods I. Oxygen isotopic composition of eggwater and carbon isotopic composition of siphuncle organic matter in Nautilus. Geochim. Cosmochim. Acta 49, 2527–2532.

D'Hondt, S., 2005. Consequences of the Cretaceous/Paleogene Mass Extinction for Marine Ecosystems. Annu. Rev. Ecol. Evol. Syst. 36, 295–317.

Da Silva, A., 2006. Investigation of Cretaceous Molluscan Shell Material for Isotopic Integrity: Examples and Implications from the Baculites compressus/cuneatus Biozones (Campanian) of the Western Interior Seaway. University of South Florida.

Dennis, K.J., Affek, H.P., Passey, B.H., Schrag, D.P., Eiler, J.M., 2011. Defining an absolute reference frame for “clumped” isotope studies of CO2. Geochim. Cosmochim. Acta 75, 7117–7131.

Dennis, K.J., Cochran, J.K., Landman, N.H., Schrag, D.P., 2013. The climate of the Late Cretaceous: New insights from the application of the carbonate clumped isotope thermometer to Western Interior Seaway macrofossil. Earth Planet. Sci. Lett. 362, 51–65.

Dettman, D.L., Lohmann, K.C., 2000. Oxygen isotope evidence for high-altitude snow in the Laramide Rocky Mountains of North America during the Late Cretaceous and Paleogene. Geology 28, 243–246.

Dettman, D.L., Reische, A.K., Lohmann, K.C., 1999. Controls on the stable isotope composition of seasonal growth bands in aragonitic fresh-water bivalves (Unionidae). Geochim. Cosmochim. Acta 63, 1049–1057.

Ditchfield, P.W., Marshall, J.D., Pirrie, F., 1994. High latitude palaeotemperature variation: New data from the Tithonian to Eocene of James Ross Island, Antarctica. Palaeogeogr. Palaeoclimatol. Palaeoecol. 107, 79–101.

Dunlop, D.J., Ozdemir, O., 1997. Rock Magnetism. Cambridge University Press.

Dutton, A., Huber, B.T., Lohmann, K.C., Zinsmeister, W.J., 2007. High-resolution stable isotope profiles of a dimitobelid belemnite: implications for paleodepth habitat and Late Maastrichtian climate seasonality. Palaios 22, 642.

Eagle, R.A., Eiler, J.M., Tripati, A.K., Ries, J.B., Freitas, P.S., Hiebenthal, C., Wanamaker Jr., A.D., Taviani, M., Elliot, M., Marenssi, S.A., Nakamura, K., Ramirez, P., Roy, K., 2013. The influence of temperature and seawater carbonate saturation state on 13C-18O bond ordering in bivalve mollusks. Biogeosciences Discuss. 10, 157–194.

Eiler, J.M., 2007. “Clumped-isotope” geochemistry—The study of naturally-occurring, multiply-substituted isotopologues. Earth Planet. Sci. Lett. 262, 309–327.

Eiler, J.M., 2011. Paleoclimate reconstruction using carbonate clumped isotope thermometry. Quat. Sci. Rev. 30, 3575–3588.

Elliot, D.H., Askin, R.A., Kyte, F.T., Zinsmeister, W.J., 1994. Iridium and dinocysts at the Cretaceous-Tertiary boundary on Seymour Island, Antarctica: implications for the KT event. Geology 22, 675.

Elorza, J., Gomez Alday, J.J., Olivero, E.B., 2001. Environmental Stress and Diagenetic Modifications in Inoceramids and Belemnites from the Upper Cretaceous James Ross basin, Antarctica. Facies 44, 227–242.

Epstein, S., Buchsbaum, R., Lowenstam, H.A., Urey, H.C., 1953. Revised Carbonate-Water Isotopic Temperature Scale. Geol. Soc. Am. Bull. 64, 1315.

Fan, M., Dettman, D.L., 2009. Late Paleocene high Laramide ranges in northeast Wyoming: Oxygen isotope study of ancient river water. Earth Planet. Sci. Lett. 286, 110–121.

Farley, K.A., Ward, P., Garrison, G., Mukhopadhyay, S., 2005. Absence of extraterrestrial ^{3}He in Permian–Triassic age sedimentary rocks. Earth Planet. Sci. Lett. 240, 265–275.

Fatherree, J.W., Harries, P.J., Quinn, T.M., 1998. Oxygen and Carbon Isotopic "Dissection" of Baculites compressus (Mollusca: Cephalopoda) from the Pierre Shale (Upper Campanian) of South Dakota: Implications for Paleoenvironmental Reconstructions. Palaios 13, 376–385.

Filmer, P.E., Kirschvink, J.L., 1989. A Paleomagnetic Constaint on the Late Cretaceous Paleoposition of Northwestern Baja California, Mexico. J. Geophys. Res. 94, 7332–7342.

Fisher, C.G., Arthur, M.A., 2002. Water mass characteristics in the Cenomanian US Western Interior seaway as indicated by stable isotopes of calcareous organisms. Palaeogeogr. Palaeoclimatol. Palaeoecol. 188, 189–213.

Fisher, R., 1953. Dispersion on a sphere. Proc. R. Soc. Lond. Ser. Math. Phys. Sci. 217, 295.

Forester, R.W., Caldwell, W.G.E., Oro, F.H., 1977. Oxygen and carbon isotopic study of ammonites from the Late Cretaceous Bearpaw Formation in southwestern Saskatchewan. Can. J. Earth Sci. 14, 2086–2100.

Foster, L.C., Andersson, C., Høie, H., Allison, N., Finch, A.A., Johansen, T., 2008. Effects of micromilling on δ18O in biogenic aragonite. Geochem. Geophys. Geosystems 9.

Fricke, H.C., Foreman, B.Z., Sewall, J.O., 2010. Integrated climate model-oxygen isotope evidence for a North American monsoon during the Late Cretaceous. Earth Planet. Sci. Lett. 289, 11–21.

Friedman, I., O'NEIL, J., Cebula, G., 1982. Two New Carbonate Stable-Isotope Standards. Geostand. Geoanalytical Res. 6, 11–12.

Gertsch, B., Keller, G., Adatte, T., Garg, R., Prasad, V., Berner, Z., Fleitmann, D., 2011. Environmental effects of Deccan volcanism across the Cretaceous–Tertiary transition in Meghalaya, India. Earth Planet. Sci. Lett. 310, 272–285.

Gill, I., Olson, J.J., Hubbard, D.K., 1995. Corals, paleotemperature records, and the aragonite-calcite transformation. Geology 23, 333.

Gillikin, D.P., De Ridder, F., Ulens, H., Elskens, M., Keppens, E., Baeyens, W., Dehairs, F., 2005. Assessing the reproducibility and reliability of estuarine bivalve shells (*Saxidomus giganteus*) for sea surface temperature reconstruction: Implications for paleoclimate studies. Palaeogeogr. Palaeoclimatol. Palaeoecol. 228, 70–85.

Gillikin, D.P., Farley, K.A., Kumai, Y., 2009. Ontogenic increase of metabolic carbon in freshwater mussel shells (Pyganodon cataracta). J Geophys Res 114, G01007.

Gillikin, D.P., Lorrain, A., Meng, L., Dehairs, F., 2007. A large metabolic carbon contribution to the $\delta^{13}C$ record in marine aragonitic bivalve shells. Geochim. Cosmochim. Acta 71, 2936–2946.

Gradstein, F.M., Ogg, J.G., Schmitz, M., Ogg, G., 2012. The Geologic Time Scale 2012 2-Volume Set. Elsevier.

Gradstein, F.M., Ogg, J.G., Smith, A.G., 2004. A geologic time scale 2004. Cambridge University Press.

Halgedahl, S.L., 1993. Experiments to Investigate the Origin of Anomalously Elevated Unblocking Temperatures. J. Geophys. Res. 98, 22443–22460.

Hartman, J.H., 1998. The biostratigraphy and paleontology of latest Cretaceous and Paleocene freshwater bivalves from the Western Williston Basin, Montana, USA, in: Bivalves: An Eon of Evolution: Paleobiological Studies Honoring Norman D. Newell. University of Calgary Press, Calgary, pp. 317–345.

He, S., Kyser, T.K., Caldwell, W.G.E., 2005. Paleoenvironment of the Western Interior Seaway inferred from δ18O and δ13C values of molluscs from the Cretaceous Bearpaw marine cyclothem. Palaeogeogr. Palaeoclimatol. Palaeoecol. 217, 67–85.

Henderson, R.A., Price, G.D., 2012. Paleoenvironment and paleoecology inferred from oxygen and carbon isotopes of subtropical mollusks from the Late Cretaceous (Cenomanian) of Bathurst Island, Australia. Palaios 27, 617–626.

Henkes, G.A., Passey, B.H., Wanamaker, A.D., Grossman, E.L., Ambrose, W.G., Carroll, M.L., 2013. Carbonate clumped isotope compositions of modern marine mollusk and brachiopod shells. Geochim. Cosmochim. Acta.

Hildebrand, A.R., Penfield, G.T., Kring, D.A., Pilkington, M., Camargo Z., A., Jacobsen, S.B., Boynton, W.V., 1991. Chicxulub Crater: A possible Cretaceous/Tertiary boundary impact crater on the Yucatán Peninsula, Mexico. Geology 19, 867.

Hodell, D.A., Venz, K.A., Charles, C.D., Ninnemann, U.S., 2003. Pleistocene vertical carbon isotope and carbonate gradients in the South Atlantic sector of the Southern Ocean. Geochem. Geophys. Geosystems 4, 1–19.

Holland, M.M., Bitz, C.M., 2003. Polar amplification of climate change in coupled models. Clim. Dyn. 21, 221–232.

Huntington, K.W., Eiler, J.M., Affek, H.P., Guo, W., Bonifacie, M., Yeung, L.Y., Thiagarajan, N., Passey, B., Tripati, A., Daëron, M., Came, R., 2009. Methods and limitations of “clumped” CO2 isotope

(D47) analysis by as-source isotope ratio mass spectrometry. J. Mass Spectrom. 44, 1318–1329.

Jacobs, D.K., Landman, N.H., 1993. Nautilus - a poor model for the function and behavior of ammonoids? Lethaia 26, 101–111.

Javoy, M., Michard, G., 1989. Global catastrophes and volcanic events: a comparison of volcanic and industrial outgassings under normal and catastrophic conditions. AGU EOS Trans. 70, 1421.

Jay, A.E., Niocaill, C.M., Widdowson, M., Self, S., Turner, W., 2009. New palaeomagnetic data from the Mahabaleshwar Plateau, Deccan Flood Basalt Province, India: implications for the volcanostratigraphic architecture of continental flood basalt provinces. J. Geol. Soc. 166, 13–24.

Jay, A.E., Widdowson, M., 2008. Stratigraphy, structure and volcanology of the SE Deccan continental flood basalt province: implications for eruptive extent and volumes. J. Geol. Soc. 165, 177–188.

Keller, G., Adatte, T., Pardo, A., Bajpai, S., Khosla, A., Samant, B., 2010. Cretaceous Extinctions: Evidence Overlooked. Science 328, 974–975.

Kim, S.T., Mucci, A., Taylor, B.E., 2007a. Phosphoric acid fractionation factors for calcite and aragonite between 25 and 75 C: revisited. Chem. Geol. 246, 135–146.

Kim, S.T., O'Neil, J.R., 1997. Equilibrium and nonequilibrium oxygen isotope effects in synthetic carbonates. Geochim. Cosmochim. Acta 61, 3461–3475.

Kim, S.T., Oneil, J., Hillairemarcel, C., Mucci, A., 2007b. Oxygen isotope fractionation between synthetic aragonite and water: Influence of temperature and Mg2+ concentration. Geochim. Cosmochim. Acta 71, 4704–4715.

Kirschvink, J.L., 1980. The least-squares line and plane and the analysis of palaeomagnetic data. Geophys. J. R. Astron. Soc. 62, 699–718.

Kirschvink, J.L., Kopp, R.E., Raub, T.D., Baumgartner, C., Holt, J.W., 2008. Rapid, precise, and high-sensitivity acquisition of paleomagnetic and rock-magnetic data: Development of a low-noise automatic sample changing system for superconducting rock magnetometers. Geochem. Geophys. Geosystems 9.

Kump, L.R., Pavlov, A., Arthur, M.A., 2005. Massive release of hydrogen sulfide to the surface ocean and atmosphere during intervals of oceanic anoxia. Geology 33, 397.

Landman, N.H., Cochran, J.K., Larson, N.L., Brezina, J., Garb, M.P., Harries, P.J., 2012. Methane seeps as ammonite habitats in the U.S. Western Interior Seaway revealed by isotopic analyses of well-preserved shell material. Geology 40, 507–510.

LeCain, R., Clyde, W.C., Wilson, G.P., Reidel, J., 2014. Magnetostratigraphy of the Hell Creek and Lower Fort Union Formations in northeastern Montana. Geol. Soc. Am. Spec. Pap. 503, 137–148.

Li, L., Keller, G., 1998. Abrupt deep-sea warming at the end of the Cretaceous. Geology 26, 995–998.

Little, S.A., Kembel, S.W., Wilf, P., 2010. Paleotemperature proxies from leaf fossils reinterpreted in light of evolutionary history. PLoS ONE 5, e15161.

Liu, Y.-G., Schmitt, R.A., 1996. Cretaceous Tertiary phenomena in the context of seafloor rearrangements and P(CO2) fluctuations over the past 100 m.y. Geochim. Cosmochim. Acta 60, 973–994.

Lowenstam, H.A., Weiner, S., 1989. On biomineralization. Oxford University Press, New York.

Lukeneder, A., Harzhauser, M., Müllegger, S., Piller, W.E., 2010. Ontogeny and habitat change in Mesozoic cephalopods revealed by stable isotopes ($\delta^{18}O$, $\delta^{13}C$). Earth Planet. Sci. Lett. 296, 103–114.

Macellari, C.E., 1986. Late Campanian-Maastrichtian ammonite fauna from Seymour Island (Antarctic Peninsula). Mem. Paleontol. Soc. 18, 1–55.

Macellari, C.E., 1987. Progressive endemism in the Late Cretaceous ammonite family Kossmaticeratidea and the breakup of Gondwanaland. Gondwana Six Stratigr. Sedimentol. Paleontol. 85–92.

Macellari, C.E., 1988. Stratigraphy, sedimentology, and paleoecology of Upper Cretaceous/Paleocene shelf-deltaic sediments of Seymour Island. Geol. Paleontol. Seymour Isl. Antarct. Penins. 169, 25–54.

Magurran, A.E., 2004. Measuring Biological Diversity. Blackwell Publishing, Oxford.

Malchus, N., Steuber, T., 2002. Stable isotope records (O, C) of Jurassic aragonitic shells from England and NW Poland: palaeoecologic and environmental implications. Geobios 35, 29–39.

Manabe, S., Stouffer, R.J., 1980. Sensitivity of a global climate model to an increase of CO 2 concentration in the atmosphere. J. Geophys. Res. 85, 5529–54.

Marshall, C.R., 1995. Distinguishing between sudden and gradual extinctions in the fossil record: Predicting the position of the Cretaceous-Tertiary iridium anomaly using the ammonite fossil record on Seymour Island, Antarctica. Geology 23, 731.

Marshall, C.R., Ward, P.D., 1996. Sudden and gradual molluscan extinctions in the latest Cretaceous of western European Tethys. Science 274, 1360–1363.

McArthur, J.M., Crame, J.A., Thirlwall, M.F., 2000. Definition of Late Cretaceous stage boundaries in Antarctica using strontium isotope stratigraphy. J. Geol. 108, 623–640.

McConnaughey, T., 1989a. 13C and 18O isotopic disequilibrium in biological carbonates: I. Patterns. Geochim. Cosmochim. Acta 53, 151–162.

McConnaughey, T., 1989b. 13C 18O isotopic disequilibrium in biological carbonates II. In vitro simulation of kinetic isotope effect. Geochim. Cosmochim. Acta 53, 163–171.

McConnaughey, T.A., Burdett, J., Whelan, J.F., Paull, C.K., 1997. Carbon isotopes in biological carbonates: respiration and photosynthesis. Geochim. Cosmochim. Acta 61, 611–622.

McConnaughey, T.A., Gillikin, D.P., 2008. Carbon isotopes in mollusk shell carbonates. Geo-Mar. Lett. 28, 287–299.

McCrea, J.M., 1950. On the Isotopic Chemistry of carbonates and a Paleotemperature Scale. J. Chem. Phys. 18, 849–857.

McFadden, P.L., McElhinny, M.W., 1988. The combined analysis of remagnetization circles and direct observations in palaeomagnetism. Earth Planet. Sci. Lett. 87, 161–172.

McFadden, P.L., McElhinny, M.W., 1990. Classification of the reversal test in palaeomagnetism. Geophys. J. Int. 103, 725–729.

McLaren, D.J., 1985. Mass extinction and iridium anomaly in the Upper Devonian of Western Australia: A commentary. Geology 13, 170.

Mitchell, J.S., Roopnarine, P.D., Angielczyk, K.D., 2012. Late Cretaceous restructuring of terrestrial communities facilitated the end-Cretaceous mass extinction in North America. Proc. Natl. Acad. Sci. 109, 18857–18861.

Molina, E., Alegret, L., Arenillas, I., Arz, J.A., Gallala, N., Hardenbol, J., Salis, K., Steurbaut, E., Vandenberghe, N., Zaghbib-Turki, D., 2006. The Global Boundary Stratotype Section and Point for the base of the Danian Stage (Paleocene, Paleogene," Tertiary", Cenozoic) at El Kef, Tunisia-Original definition and revision. Episodes 29, 263.

Moore, J.R., Wilson, G.P., Sharma, M., Hallock, H.R., Braman, D.R., 2014. Assessing the relationships of the Hell Creek–Fort Union contact, Cretaceous-Paleogene boundary, and Chicxulub impact ejecta horizon at the Hell Creek Formation lectostratotype, Montana, US. Geol. Soc. Am. Spec. Pap. 503, 123–136.

Moriya, K., Nishi, H., Kawahata, H., Tanabe, K., Takayanagi, Y., 2003. Demersal habitat of Late Cretaceous ammonoids: Evidence from oxygen isotopes for the Campanian (Late Cretaceous) northwestern Pacific thermal structure. Geology 31, 167.

Morrison, J.O., Brand, U., 1986. PALEOSCENE# 5. Geochemistry of Recent Marine Invertebrates. Geosci. Can. 13.

Olivero, E.B., 2012. Sedimentary cycles, ammonite diversity and palaeoenvironmental changes in the Upper Cretaceous Marambio Group, Antarctica. Cretac. Res.

Olivero, E.B., Medina, F.A., 2000. Patterns of Late Cretaceous ammonite biogeography in souther high latitudes: the family Kossmaticeratidae in Antarctica. Cretac. Res. 21, 269–279.

Olivero, E.B., Ponce, J.J., Marsicano, C.A., Martinioni, D.R., 2007. Depositional Settings of the basal López de Bertodano Formation, Maastrichtian, Antarctica. Rev. Asoc. Geológica Argent. 62, 521–529.

Olsen, P.E., Kent, D.V., Sues, H.D., Koeberl, C., Huber, H., Montanari, A., Rainforth, E.C., Fowell, S.J., Szajna, M.J., Hartline, B.W., 2002. Ascent of dinosaurs linked to an iridium anomaly at the Triassic-Jurassic boundary. Science 296, 1305.

Passey, B.H., Levin, N.E., Cerling, T.E., Brown, F.H., Eiler, J.M., 2010. High-temperature environments of human evolution in East Africa based on bond ordering in paleosol carbonates. Proc. Natl. Acad. Sci. 107, 11245–11249.

Paull, C.K., Martens, C.S., Chanton, J.P., Neumann, A.C., Coston, J., Jull, A.J.T., Toolin, L.J., 1989. Old carbon in living organisms and young CaCO3 cements from abyssal brine seeps. Nature 342, 166–168.

Peng, T.H., Takahashi, T., Broecker, W.S., Olafsson, J., 1987. Seasonal variability of carbon dioxide, nutrients and oxygen in the northern North Atlantic surface water: observations and a model*. Tellus B 39, 439–458.

Pirrie, D., 1994. Petrography and provenance of the Marambio Group, Vega Island, Antarctica. Antarct. Sci. 6, 517–527.

Playford, P.E., McLaren, D.J., Orth, C.J., Gilmore, J.S., Goodfellow, W.D., 1984. Iridium anomaly in the Upper Devonian of the Canning Basin, western Australia. Science 226, 437.

Price, G.D., Wilkinson, D., Hart, M.B., Page, K.N., Grimes, S.T., 2009. Isotopic analysis of coexisting Late Jurassic fish otoliths and molluscs: Implications for upper-ocean water temperature estimates. Geology 37, 215–218.

Purvis, A., 2000. Nonrandom Extinction and the Loss of Evolutionary History. Science 288, 328–330.

Raup, D.M., Sepkoski, J.J., 1982. Mass extinctions in the marine fossil record. Science 215, 1501–1503.

Rexfort, A., Mutterlose, J., 2006. Stable isotope records from Sepia officinalis—a key to understanding the ecology of belemnites? Earth Planet. Sci. Lett. 247, 212–221.

Ritterbush, K.A., Bottjer, D.J., 2012. Westermann Morphospace displays ammonoid shell shape and hypothetical paleoecology. Paleobiology 38, 424–446.

Ritterbush, K.A., Hoffmann, R., Lukeneder, A., De Baets, K., 2014. Pelagic palaeoecology: the importance of recent constraints on ammonoid palaeobiology and life history: Pelagic palaeoecology of ammonoids. J. Zool. 292, 229–241.

Robinson, N., Ravizza, G., Coccioni, R., Peucker-Ehrenbrink, B., Norris, R., 2009. A high-resolution marine 187Os/188Os record for the late Maastrichtian: Distinguishing the chemical fingerprints of Deccan volcanism and the KP impact event. Earth Planet. Sci. Lett. 281, 159–168.

Rohde, R.A., Muller, R.A., 2005. Cycles in fossil diversity. Nature 434, 208–210.

Romanek, C.S., Grossman, E.L., Morse, J.W., 1992. Carbon isotopic fractionation in synthetic aragonite and calcite: Effects of temperature and precipitation rate. Geochim. Cosmochim. Acta 56, 419–430.

Royer, D.L., Berner, R.A., Park, J., 2007. Climate sensitivity constrained by CO_2 concentrations over the past 420 million years. Nature 446, 530–532.

Samant, B., Mohabey, D.M., 2009. Palynoflora from Deccan volcano-sedimentary sequence (Cretaceous-Palaeogene transition) of central India: implications for spatio-temporal correlation. J. Biosci. 34, 811–823.

Scheffer, M., Carpenter, S., Foley, J.A., Folke, C., Walker, B., 2001. Catastrophic shifts in ecosystems. Nature 413, 591–596.

Scholz, H., Hartman, J.H., 2007. Fourier analysis and the extinction of unionoid bivalves near the Cretaceous-Tertiary boundary of the Western Interior, USA: Pattern, causes, and ecological significance. Palaeogeogr. Palaeoclimatol. Palaeoecol. 255, 48–63.

Schone, B.R., Houk, S.D., Castro, A.D.F., Fiebig, J., Oschmann, W., Kroncke, I., Dreyer, W., Gosselck, F., 2005. Daily growth gates in shells of Arctica islandica: Assessing sub-seasonal environmental controls on a long-lived bivalve mollusk. Palaios 20, 78–92.

Schulte, P., Alegret, L., Arenillas, I., Arz, J.A., Barton, P.J., Bown, P.R., Bralower, T.J., Christeson, G.L., Claeys, P., Cockell, C.S., Collins, G.S., Deutsch, A., Goldin, T.J., Goto, K., Grajales-Nishimura, J.M., Grieve, R.A.F., Gulick, S.P.S., Johnson, K.R., Kiessling, W., Koeberl, C., Kring, D.A., MacLeod, K.G., Matsui, T., Melosh, J., Montanari, A., Morgan, J.V., Neal, C.R., Nichols, D.J., Norris, R.D., Pierazzo, E., Ravizza, G., Rebolledo-Vieyra, M., Reimold, W.U., Robin, E., Salge, T., Speijer, R.P., Sweet, A.R., Urrutia-Fucugauchi, J., Vajda, V., Whalen, M.T., Willumsen, P.S., 2010. The Chicxulub asteroid impact and mass extinction at the Cretaceous-Paleogene boundary. Science 327, 1214–1218.

Self, S., Widdowson, M., Thordarson, T., Jay, A.E., 2006. Volatile fluxes during flood basalt eruptions and potential effects on the global environment: A Deccan perspective. Earth Planet. Sci. Lett. 248, 518–532.

Sellwood, B.W., Valdes, P.J., 2006. Mesozoic climates: General circulation models and the rock record. Sediment. Geol. 190, 269–287.

Sepkoski Jr., J.J., 1997. Biodiversity: past, present, and future. J. Paleontol. 71, 533–539.

Shackleton, N.J., Kennett, J.P., 1975. Late Cenozoic Oxygen and Carbon Isotopic Changes at DSPDP Site 284: Implications For Glacial History of the Northern Hemisphere and Antarctica. Initial Rep. Deep Sea Drill. Proj. 29, 801–807.

Song, H., Tong, J., Algeo, T.J., Horacek, M., Qiu, H., Song, H., Tian, L., Chen, Z.-Q., 2013. Large vertical δ13CDIC gradients in Early Triassic seas of the South China craton: Implications for oceanographic changes related to Siberian Traps volcanism. Glob. Planet. Change 105, 7–20.

Spötl, C., Mattey, D., 2006. Stable isotope microsampling of speleothems for palaeoenvironmental studies: A comparison of microdrill, micromill and laser ablation techniques. Chem. Geol. 235, 48–58.

Swart, P.K., Leder, J., Gill, I., Olson, J.J., Hubbard, D.K., 1996. Corals, paleotemperature records, and the aragonite-calcite transformation: Comment and Reply. Geology 24, 91.

Tanner, L.H., Kyte, F.T., Walker, A.E., 2008. Multiple Ir anomalies in uppermost Triassic to Jurassic-age strata of the Blomidon Formation, Fundy basin, eastern Canada. Earth Planet. Sci. Lett. 274, 103–111.

Taylor, B., Ward, P., 1983. Stable isotopic studies of Nautilus macromphalus Sowerby (New Caledonia) and Nautilus pompilius L. (Fiji). Palaeogeogr. Palaeoclimatol. Palaeoecol. 41, 1–16.

Tobin, T.S., Schauer, A.J., Lewarch, E., 2011. Alteration of micromilled carbonate $\delta^{18}O$ during Kiel Device analysis. Rapid Commun. Mass Spectrom. 25, 2149–2152.

Tobin, T.S., Ward, P.D., submitted. Carbon isotope ($\delta^{13}C$) discrepancies between Late Cretaceous ammonites and benthic mollusks from Antarctica. Palaeogeogr. Palaeoclimatol. Palaeoecol.

Tobin, T.S., Ward, P.D., Steig, E.J., Olivero, E.B., Hilburn, I.A., Mitchell, R.N., Diamond, M.R., Raub, T.D., Kirschvink, J.L., 2012. Extinction patterns, δ18O trends, and magnetostratigraphy from a southern high-latitude Cretaceous–Paleogene section: Links with Deccan volcanism. Palaeogeogr. Palaeoclimatol. Palaeoecol. 350-352, 180–188.

Tobin, T.S., Wilson, G.P., Eiler, J.M., Hartman, J.H., 2014. Environmental change across a terrestrial Cretaceous-Paleogene boundary section in eastern Montana, USA, constrained by carbonate clumped isotope paleothermometry. Geology 42, 351–354.

Torsvik, T.H., Müller, R.D., Van der Voo, R., Steinberger, B., Gaina, C., 2008. Global plate motion frames: toward a unified model. Rev Geophys 46.

Van der Voo, R., 1993. Paleomagnetism of the Atlantic, Tethys, and Iapetus oceans. Cambridge University Press.

Vellekoop, J., Sluijs, A., Smit, J., Schouten, S., Weijers, J.W.H., Damsté, J.S.S., Brinkhuis, H., 2014. Rapid short-term cooling following the Chicxulub impact at the Cretaceous–Paleogene boundary. Proc. Natl. Acad. Sci. 201319253.

Walker, J.C.G., Kasting, J.F., 1992. Effects of fuel and forest conservation on future levels of atmospheric carbon dioxide. Glob. Planet. Change 5, 151–189.

Wang, S.C., Marshall, C.R., 2004. Improved confidence intervals for estimating the position of a mass extinction boundary. Paleobiology 30, 5–18.

Wani, R., Kase, T., Shigeta, Y., Ocampo, R.D., 2005. New look at ammonoid taphonomy, based on field experiments with modern chambered nautilus. Geology 33, 849.

Ward, P.D., 1996. Ammonoid Extinction, in: Ammonoid Paleobiology, Topics in Geobiology. Plenum Press, New York, pp. 815–823.

Ward, P.D., Hurtado, J.M., Kirschvink, J.L., Verosub, K.L., 1997. Measurements of the Cretaceous paleolatitude of Vancouver Island: consistent with the Baja-British Columbia hypothesis. Science 277, 1642.

Warnke, K., Oppelt, A., Hoffmann, R., 2010. Stable isotopes during ontogeny of Spirula and derived hatching temperatures. Ferrantia 59, 191–201.

Weiner, S., Dove, P.M., 2003. An overview of biomineralization processes and the problem of the vital effect. Rev. Mineral. Geochem. 54, 1.

Westermann, G.E.G., 1996. Ammonoid Life and Habitat, in: Ammonoid Paleobiology, Topics in Geobiology. Plenum Press, New York, pp. 607–707.

White, R.V., Saunders, A.D., 2005. Volcanism, impact and mass extinctions: incredible or credible coincidences? Lithos 79, 299–316.

Whiteside, J.H., Olsen, P.E., Eglinton, T., Brookfield, M.E., Sambrotto, R.N., 2010. Compound-specific carbon isotopes from Earth's largest flood basalt eruptions directly linked to the end-Triassic mass extinction. Proc. Natl. Acad. Sci. 107, 6721.

Wierzbowski, H., 2002. Detailed oxygen and carbon isotope stratigraphy of the Oxfordian in Central Poland. Int. J. Earth Sci. 91, 304–314.

Wierzbowski, H., Joachimski, M., 2007. Reconstruction of late Bajocian–Bathonian marine palaeoenvironments using carbon and oxygen isotope ratios of calcareous fossils from the Polish Jura Chain (central Poland). Palaeogeogr. Palaeoclimatol. Palaeoecol. 254, 523–540.

Wignall, P.B., 2001. Large igneous provinces and mass extinctions. Earth-Sci. Rev. 53, 1–33.

Wilde, E.M., Bergatino, R.N., 2004a. Geologic map of the Fort Peck Lake East 30' x 60' quadrangle, eastern Montana. Mont. Bur. Mines Geol. Open-File Report 498.

Wilde, E.M., Bergatino, R.N., 2004b. Geologic map of the Fort Peck Lake West 30' x 60' quadrangle, eastern Montana. Mont. Bur. Mines Geol. Open-File Report 499.

Wilde, E.M., Vuke, S.M., 2004a. Geologic map of the Jordan 30' x 60' quadrangle, eastern Montana. Mont. Bur. Mines Geol. Open-File Report 514.

Wilde, E.M., Vuke, S.M., 2004b. Geologic map of the Sand Springs 30' x 60' quadrangle, eastern Montana. Mont. Bur. Mines Geol. Open-File Report 515.

Wilf, P., Johnson, K.R., Huber, B.T., 2003. Correlated terrestrial and marine evidence for global climate changes before mass extinction at the Cretaceous–Paleogene boundary. Proc. Natl. Acad. Sci. U. S. A. 100, 599–604.

Wilson, G.P., 2005. Mammalian faunal dynamics during the last 1.8 million years of the Cretaceous in Garfield County, Montana. J. Mamm. Evol. 12, 53–76.

Wilson, G.P., 2014. Mammalian extinction, survival, and recovery dynamics across the Cretaceous-Paleogene boundary in northeastern Montana, U.S.A. Geol. Soc. Am. Spec. Pap. 503, 365–390.

Wilson, G.P., DeMar, D., Carter, G., 2014. Extinction and survival of salamander and salamander-like amphibians across the Cretaceous-Paleogene boundary in northeastern Montana USA. Geol. Soc. Am. Spec. Pap. 503, 271–298.

Zaarur, S., Affek, H.P., Brandon, M.T., 2013. A revised calibration of the clumped isotope thermometer. Earth Planet. Sci. Lett. 382, 47–57.

Zaarur, S., Olack, G., Affek, H.P., 2011. Paleo-environmental implication of clumped isotopes in land snail shells. Geochim. Cosmochim. Acta 75, 6859–6869.

Zakharov, Y.D., Shigeta, Y., Smyshlyaeva, O.P., Popov, A.M., Ignatiev, A.V., 2006. Relationship between d13C and d18O values of the Recent Nautilus and brachiopod shells in the whild and the problem of reconstruction of fossil cephalopod habitat. Geosci. J. 10, 331–345.

Zinsmeister, W.J., 1998. Discovery of fish mortality horizon at the KT boundary on Seymour Island: re-evaluation of events at the end of the Cretaceous. J. Paleontol. 72, 556–571.

Zinsmeister, W.J., 2001. Late Maastrichtian short-term biotic events on Seymour Island, Antarctic Peninsula. J. Geol. 109, 213–229.

Zinsmeister, W.J., Feldmann, R.M., Woodburne, M.O., Elliot, D.H., 1989. Latest Cretaceous/earliest Tertiary transition on Seymour Island, Antarctica. J. Paleontol. 63, 731–738.

Appendix 2.1

Sample Number	Group	Strat	Analysis#	Mineralogy	Preparation	Flags	δ13C_VPDB	StdDev_d13C	δ18O_CorrAcid	StdDev_d18O
LB05-01B	Bivalve	0	8241	Aragonite	Micromill	0	0.10248	0.026	0.224697512	0.028
LB05-01B	Bivalve	0	8242	Aragonite	Micromill	0	0.56815	0.015	0.568969606	0.025
LB05-01B	Bivalve	0	8243	Aragonite	Micromill	0	1.2732	0.007	0.576971229	0.026
LB05-01C	Rotularia	0	8298	Calcite	Micromill	0	1.408	0.022	0.474236335	0.044
LB05-01C	Rotularia	0	8367	Calcite	Micromill	0	1.3829	0.016	0.194790369	0.036
LB05-01C	Rotularia	0	8299	Calcite	Micromill	0	1.0402	0.03	0.598232374	0.044
LB05-01C	Rotularia	0	8368	Calcite	Micromill	0	0.89666	0.013	0.334544723	0.038
LB05-01C	Rotularia	0	8300	Calcite	Micromill	1000	0.25826	0.028	-0.265752758	0.05
LB06-04A	Gastropod	200.5	2929	Aragonite	Dremel	0	2.441	0.016	0.883996831	0.032
LB06-04A	Gastropod	200.5	8307	Aragonite	Micromill	0	1.3869	0.007	0.757751254	0.022
LB06-04A	Gastropod	200.5	8308	Aragonite	Micromill	0	2.3025	0.015	1.06658759	0.014
LB06-04A	Gastropod	200.5	8309	Aragonite	Micromill	0	2.9186	0.019	1.079637013	0.038
LB06-04A	Gastropod	200.5	2892	Aragonite	Dremel	0	0.68143	0.029	0.900991428	0.035
LB06-04A	Gastropod	200.5	7266	Aragonite	Micromill	0	2.6173	0.014	1.163294939	0.032
LB07-401-ALT	Ammonite	394.9	11836	Aragonite	Crush	0	-10.0052	0.022	-0.256547838	0.048
LB07-401-ALT	Ammonite	394.9	11837	Aragonite	Crush	10	-10.0634	0.077	-0.345656225	0.066
LB07-402	Ammonite	394.9	11838	Aragonite	Crush	0	-0.54764	0.028	1.356373744	0.028
LB07-402	Ammonite	394.9	11839	Aragonite	Crush	0	-0.53058	0.012	1.347377138	0.033
LB07-403	Echinoid	394.9	11871	Calcite	Crush	0	13.0459	0.019	1.0935	0.027
LB07-403	Echinoid	394.9	11872	Calcite	Crush	0	12.9324	0.039	1.4048	0.018
LB07-400	Ammonite	407.9	11831	Aragonite	Crush	0	1.8657	0.021	1.271305833	0.033
LB07-400	Ammonite	407.9	11835	Aragonite	Crush	0	1.6478	0.033	1.030996481	0.032
LB07-404	Bivalve	407.9	11873	Calcite	Crush	0	2.8056	0.045	0.45605	0.035
LB07-404	Bivalve	407.9	11874	Calcite	Crush	0	2.9784	0.043	0.45505	0.029
LB07-405	Gastropod	422.9	11875	Aragonite	Crush	0	4.02	0.023	1.508316429	0.021
LB07-405	Gastropod	422.9	11876	Aragonite	Crush	0	4.2892	0.036	1.596783058	0.039
LB07-406	Echinoid	422.9	11877	Calcite	Crush	0	20.6466	0.013	0.93638	0.01
LB07-406	Echinoid	422.9	11881	Calcite	Crush	1000	20.3523	0.021	0.88964	0.027
LB07-407	Ammonite	422.9	11882	Aragonite	Crush	0	0.37486	0.031	1.338380532	0.031
LB07-407	Ammonite	422.9	11883	Aragonite	Crush	0	0.46828	0.015	1.337380909	0.016
LB07-408	Ammonite	422.9	11884	Aragonite	Crush	0	2.9834	0.029	0.676230304	0.026
LB07-408	Ammonite	422.9	11885	Aragonite	Crush	0	0.060472	0.039	0.618602043	0.015

LB07-409	Bivalve	422.9	11886	Calcite	Crush	0	1.8886	0.031	0.52566	0.028
LB07-409	Bivalve	422.9	11887	Calcite	Crush	0	1.7731	0.024	0.28898	0.022
LB07-410-BD	Ammonite	422.9	11888	Aragonite	Crush	0	-0.64867	0.022	0.782590184	0.03
LB07-410-BD	Ammonite	422.9	11892	Aragonite	Crush	0	-0.57434	0.024	0.752801421	0.033
LB07-411	Ammonite	422.9	11893	Aragonite	Crush	0	-0.89576	0.019	0.356161039	0.023
LB07-411	Ammonite	422.9	11894	Aragonite	Crush	0	-0.80938	0.027	0.288556541	0.028
LB07-412-ALT	Gastropod	439.6	11895	Aragonite	Crush	0	2.9653	0.024	1.310491052	0.026
LB07-412-ALT	Gastropod	439.6	11896	Aragonite	Crush	0	3.0889	0.025	1.337380909	0.03
LB07-413	Gastropod	439.6	11896	Aragonite	Crush	0	3.4414	0.03	1.638567297	0.031
LB07-413	Gastropod	439.6	11896	Aragonite	Crush	0	3.6202	0.011	1.638567297	0.023
LB07-414	Ammonite	453.1	11906	Aragonite	Crush	0	0.16942	0.031	0.832271443	0.04
LB07-414	Ammonite	453.1	11907	Aragonite	Crush	0	0.47946	0.023	1.195634378	0.02
LB07-415	Gastropod	453.1	11908	Aragonite	Crush	0	0.76636	0.022	1.386462395	0.013
LB07-415	Gastropod	453.1	11909	Aragonite	Crush	0	0.50866	0.01	1.327884491	0.013
LB07-416	Ammonite	453.1	11910	Aragonite	Crush	0	-0.74361	0.025	1.30169437	0.04
LB07-416	Ammonite	453.1	11911	Aragonite	Crush	0	-0.78689	0.017	1.239117975	0.024
LB07-417	Ammonite	453.1	11912	Aragonite	Crush	0	-5.8382	0.024	1.034195275	0.024
LB07-417	Ammonite	453.1	11916	Aragonite	Crush	0	-5.6731	0.03	1.093772801	0.027
LB07-31A	Gastropod	479.9	2936	Aragonite	Dremel	0	2.1522	0.016	1.440772198	0.023
LB07-31A	Gastropod	479.9	2957	Aragonite	Dremel	0	1.9011	0.015	1.325856352	0.049
LB07-31A	Gastropod	479.9	7267	Aragonite	Micromill	0	2.1085	0.036	1.143467909	0.067
LB07-31B	Gastropod	479.9	2939	Aragonite	Dremel	0	3.6047	0.024	1.472738225	0.053
LB07-31B	Gastropod	479.9	2958	Aragonite	Dremel	0	2.6525	0.039	1.285898817	0.036
LB07-418	Gastropod	479.9	11917	Aragonite	Crush	0	3.7782	0.016	1.694346256	0.031
LB07-418	Gastropod	479.9	11918	Aragonite	Crush	0	3.7188	0.023	1.636767976	0.031
LB07-33A	Gastropod	496.1	2933	Aragonite	Dremel	0	2.9468	0.024	0.926179849	0.039
LB07-33A	Gastropod	496.1	2946	Aragonite	Dremel	0	3.0342	0.038	1.057078708	0.021
LB07-33B	Bivalve	496.1	2940	Aragonite	Dremel	0	1.7705	0.018	1.149031617	0.071
LB07-33B	Bivalve	496.1	2956	Aragonite	Dremel	0	0.37935	0.01	0.98313198	0.03
LB07-33B	Bivalve	496.1	7268	Aragonite	Micromill	0	3.2584	0.017	1.110692615	0.025
LB07-34A	Ammonite	504.9	2847	Aragonite	Dremel	0	-2.8699	0.017	1.343154424	0.016
LB07-34A	Ammonite	504.9	9308	Aragonite	Micromill	0	-0.40302	0.036	1.125158254	0.061
LB07-34A	Ammonite	504.9	9309	Aragonite	Micromill	0	0.09821	0.043	1.221663287	0.008
LB07-34A	Ammonite	504.9	9310	Aragonite	Micromill	0	0.16564	0.03	1.170881813	0.043

LB07-34B	Ammonite	504.9	2853	Aragonite	Dremel	0	-2.4139	0.033	0.808229253	0.046
LB08-400	Gastropod	552.2	11919	Aragonite	Crush	0	3.5075	0.017	1.646864167	0.023
LB08-400	Gastropod	552.2	11920	Aragonite	Crush	0	3.4813	0.017	1.613576724	0.026
LB08-401	Bivalve	552.2	11921	Aragonite	Crush	0	2.7243	0.028	1.281501987	0.035
LB08-401	Bivalve	552.2	11922	Aragonite	Crush	0	2.8179	0.03	1.322886376	0.019
LB08-402	Bivalve	552.2	11923	Aragonite	Crush	0	3.0806	0.04	1.260309981	0.026
LB08-402	Bivalve	552.2	11927	Aragonite	Crush	0	3.0474	0.029	1.218925592	0.022
LB08-403	Bivalve	552.2	11928	Aragonite	Crush	0	1.8787	0.018	0.899945916	0.005
LB08-403	Bivalve	552.2	11929	Aragonite	Crush	0	1.9331	0.016	0.894847839	0.012
LB08-405	Gastropod	577.7	11930	Aragonite	Crush	0	3.5135	0.019	1.927458323	0.025
LB08-405	Gastropod	577.7	11931	Aragonite	Crush	0	3.597	0.026	1.929457569	0.03
LB08-406	Gastropod	577.7	11932	Aragonite	Crush	0	3.8376	0.035	1.767018843	0.028
LB08-406	Gastropod	577.7	11933	Aragonite	Crush	0	3.8779	0.016	1.716537885	0.043
LB08-407σ	Ammonite	587.9	11934	Aragonite	Crush	0	1.772	0.033	1.829595238	0.025
LB08-407σ	Ammonite	587.9	11938	Aragonite	Crush	0	1.4458	0.008	1.169444257	0.034
LB08-408	Ammonite	587.9	11952	Aragonite	Crush	0	-1.9836	0.019	1.342778873	0.025
LB08-408	Ammonite	587.9	11953	Aragonite	Crush	0	-1.7717	0.027	1.333882229	0.034
LB08-409	Gastropod	587.9	11939	Aragonite	Crush	0	1.9039	0.024	1.569193466	0.021
LB08-409	Gastropod	587.9	11940	Aragonite	Crush	0	1.8908	0.023	1.532807191	0.027
LB08-410	Gastropod	587.9	11941	Aragonite	Crush	0	3.2518	0.012	1.635768353	0.036
LB08-410	Gastropod	587.9	11942	Aragonite	Crush	0	3.2045	0.018	1.675153496	0.029
SI11110	Bivalve	621.55	21450	Aragonite	Micromill	0	-15.7836	0.017	-1.160286934	0.029
SI11110	Bivalve	621.55	21451	Aragonite	Micromill	0	-15.8519	0.004	-1.433473884	0.025
SI11110	Bivalve	621.55	21452	Aragonite	Micromill	0	-16.2055	0.014	-1.229670762	0.048
SI11055	Bivalve	621.55	21453	Aragonite	Micromill	0	-0.17184	0.01	1.039493276	0.022
SI11055	Bivalve	621.55	21454	Aragonite	Micromill	1000	2.371	0.024	1.35487431	0.104
SI11101	Bivalve	642.35	21461	Aragonite	Micromill	0	3.0944	0.02	1.451737772	0.029
SI11101	Bivalve	642.35	21462	Aragonite	Micromill	0	2.3087	0.011	1.365270388	0.025
SI11101	Bivalve	642.35	21463	Aragonite	Micromill	0	2.6734	0.016	1.502018805	0.025
SI11077	Bivalve	646.35	21455	Aragonite	Micromill	0	-2.5379	0.021	0.761897989	0.015
SI11077	Bivalve	646.35	21456	Aragonite	Micromill	0	-2.5489	0.013	0.756300101	0.028
SI11077	Bivalve	646.35	21457	Aragonite	Micromill	0	-2.5449	0.011	0.774293314	0.021
SI11072	Gastropod	647.2	21464	Aragonite	Micromill	0	2.0817	0.016	1.883374952	0.031
SI11072	Gastropod	647.2	21465	Aragonite	Micromill	0	2.2605	0.013	1.868380608	0.019

SI11072	Gastropod	647.2	21466	Aragonite	Micromill	0	2.4403	0.022	2.109189771	0.04
LB09-02A	Ammonite	664.9	2848	Aragonite	Dremel	0	0.3248	0.033	1.079131221	0.03
LB09-02B	Gastropod	664.9	2839	Aragonite	Dremel	0	-3.0376	0.019	-0.92557369	0.031
LB09-02C	Gastropod	664.9	2840	Aragonite	Dremel	0	1.0931	0.024	1.180188378	0.03
LB09-02D	Ammonite	664.9	2858	Aragonite	Dremel	0	-2.8046	0.014	1.604142877	0.019
LB09-02E	Gastropod	664.9	2857	Aragonite	Dremel	0	-4.5029	0.007	0.883187565	0.038
LB09-02F	Bivalve	664.9	9305	Aragonite	Micromill	0	-1.9027	0.017	0.458413683	0.041
LB09-02F	Bivalve	664.9	9306	Aragonite	Micromill	0	-1.9741	0.028	0.497228129	0.023
LB09-02F	Bivalve	664.9	9307	Aragonite	Micromill	101	-3.5342	0.037	-0.61730384	0.143
LB09-02K	Gastropod	664.9	8284	Aragonite	Micromill	0	0.4271	0.007	1.365510411	0.018
LB09-02K	Gastropod	664.9	8285	Aragonite	Micromill	0	-0.12466	0.031	1.020661715	0.027
LB09-02K	Gastropod	664.9	8286	Aragonite	Micromill	0	-1.5076	0.015	1.188584518	0.029
LB09-03A	Ammonite	679.9	2886	Aragonite	Dremel	0	-1.1353	0.026	-3.296674018	0.046
LB09-03B	Ammonite	679.9	2869	Aragonite	Dremel	0	-6.3247	0.013	0.482246582	0.024
LB09-04A	Rotularia	693.1	2868	Calcite	Dremel	0	1.2267	0.017	-2.785302078	0.022
LB09-04B	Rotularia	693.1	2877	Calcite	Dremel	0	1.8574	0.015	1.2557767	0.023
LB09-04B	Rotularia	693.1	2897	Calcite	Dremel	0	0.87805	0.03	0.787105472	0.04
LB09-04C	Rotularia	693.1	2867	Calcite	Dremel	0	1.8142	0.016	1.546817758	0.022
LB09-04D	Rotularia	693.1	2924	Calcite	Dremel	0	1.8963	0.017	1.04027881	0.018
LB09-04F	Bivalve	693.1	9378	Aragonite	Micromill	0	-0.63937	0.024	0.279798446	0.062
LB09-04F	Bivalve	693.1	9380	Aragonite	Micromill	0	-1.1306	0.023	0.247002921	0.055
LB09-04F	Bivalve	693.1	9408	Aragonite	Micromill	0	-0.57106	0.018	0.35533336	0.029
LB09-04G	Bivalve	693.1	9287	Aragonite	Micromill	0	0.63668	0.017	0.769890252	0.022
LB09-04G	Bivalve	693.1	9288	Aragonite	Micromill	0	0.11834	0.044	0.733068625	0.044
LB09-04G	Bivalve	693.1	9289	Aragonite	Micromill	0	0.30051	0.02	0.678331861	0.029
LB09-04H	Echinoid	693.1	8810	Calcite	Micromill	0	6.9541	0.016	0.725446461	0.008
LB09-04H	Echinoid	693.1	8811	Calcite	Micromill	0	7.4083	0.029	0.734392229	0.024
LB09-04H	Echinoid	693.1	8812	Calcite	Micromill	0	7.3519	0.018	0.712513552	0.031
LB09-04HH	Echinoid	693.1	8813	Calcite	Micromill	0	6.6429	0.022	1.007926297	0.041
LB09-04HH	Echinoid	693.1	8814	Calcite	Micromill	0	6.5745	0.038	0.922384918	0.042
LB09-04HH	Echinoid	693.1	8815	Calcite	Micromill	0	6.1858	0.019	0.876623873	0.015
LB09-04I	Echinoid	693.1	8804	Calcite	Micromill	0	13.1512	0.019	1.024826108	0.047
LB09-04I	Echinoid	693.1	8805	Calcite	Micromill	0	13.4835	0.012	1.245657053	0.028
LB09-04I	Echinoid	693.1	8806	Calcite	Micromill	0	13.0857	0.025	1.098436423	0.026

LB09-05A	Ammonite	698.6	9387	Aragonite	Micromill	0	-1.7795	0.021	0.211223224	0.07
LB09-05A	Ammonite	698.6	9388	Aragonite	Micromill	0	-1.1286	0.023	0.837362848	0.015
LB09-05A	Ammonite	698.6	9389	Aragonite	Micromill	0	-1.5213	0.024	0.627641429	0.056
LB09-05C	Gastropod	698.6	7258	Aragonite	Micromill	0	5.969	0.02	1.179176795	0.037
LB09-05C	Gastropod	698.6	8385	Aragonite	Micromill	0	6.0626	0.025	0.813489485	0.048
LB09-05D	Gastropod	698.6	9402	Aragonite	Micromill	0	1.9925	0.019	0.985458621	0.016
LB09-05D	Gastropod	698.6	9403	Aragonite	Micromill	0	1.7243	0.021	0.864169801	0.058
LB09-05D	Gastropod	698.6	9404	Aragonite	Micromill	1	1.6439	0.031	0.43781785	0.066
LB09-06A	Bivalve	707.1	2889	Aragonite	Dremel	0	-0.13515	0.027	1.354281838	0.017
LB09-06B	Bivalve	707.1	2948	Aragonite	Dremel	101	-2.2945	0.05	-3.206036167	0.108
LB09-07A	Ammonite	718.1	2911	Aragonite	Dremel	0	2.6446	0.014	0.961686417	0.011
LB09-07B	Ammonite	718.1	2859	Aragonite	Dremel	0	-2.3507	0.027	0.258282073	0.025
LB09-07C	Ammonite	718.1	2906	Aragonite	Dremel	0	-6.1963	0.032	0.970689507	0.027
LB09-07D	Ammonite	718.1	2918	Aragonite	Dremel	111	9.7421	9.359	24.65609973	7.711
LB09-07D	Ammonite	718.1	2950	Aragonite	Dremel	0	0.31406	0.026	0.941252437	0.027
LB09-07D	Ammonite	718.1	7257	Aragonite	Micromill	11	-1.8904	0.055	0.698512944	0.077
LB09-07D	Ammonite	718.1	8386	Aragonite	Micromill	101	-1.7858	0.033	0.402402324	0.116
LB09-07E	Ammonite	718.1	2903	Aragonite	Dremel	0	-11.787	0.026	0.58708706	0.018
LB09-07E	Ammonite	718.1	2904	Aragonite	Dremel	0	1.4067	0.019	0.466536696	0.029
LB09-08A	Bivalve	719.8	2875	Aragonite	Dremel	0	7.2344	0.015	-0.232658451	0.019
LB09-08A	Bivalve	719.8	2927	Aragonite	Dremel	0	0.50287	0.017	1.09420381	0.015
LB09-08B	Bivalve	719.8	2843	Aragonite	Dremel	0	4.5891	0.007	1.30613048	0.012
LB09-08B	Bivalve	719.8	2935	Aragonite	Dremel	0	6.3057	0.015	0.674447381	0.027
LB09-08B	Bivalve	719.8	2961	Aragonite	Dremel	0	2.8554	0.019	1.575616232	0.02
LB09-09A	Gastropod	732.1	8310	Aragonite	Micromill	0	2.398	0.028	1.107556708	0.034
LB09-09A	Gastropod	732.1	2881	Aragonite	Dremel	0	1.8754	0.019	1.73605332	0.026
LB09-09A	Gastropod	732.1	7254	Aragonite	Micromill	0	1.8995	0.012	1.297329707	0.033
LB09-09A	Gastropod	732.1	8311	Aragonite	Micromill	0	2.0774	0.01	0.865687176	0.022
LB09-09A	Gastropod	732.1	8312	Aragonite	Micromill	0	2.7437	0.023	1.1476154	0.021
LB09-13A	Gastropod	746.2	2856	Aragonite	Dremel	0	1.2467	0.025	0.988189896	0.039
LB09-13A	Gastropod	746.2	9296	Aragonite	Micromill	0	1.8646	0.023	1.134060186	0.037
LB09-13A	Gastropod	746.2	9297	Aragonite	Micromill	0	1.5012	0.039	1.055460175	0.031
LB09-13A	Gastropod	746.2	9298	Aragonite	Micromill	0	1.9511	0.035	1.125158254	0.025
LB09-13B	Gastropod	746.2	2846	Aragonite	Dremel	0	1.8152	0.012	1.475166025	0.03

LB09-13B	Gastropod	746.2	2888	Aragonite	Dremel	0	-1.2828	0.039	1.260609238	0.02
LB09-13C	Gastropod	746.2	2959	Aragonite	Dremel	0	-4.7595	0.018	1.324844769	0.028
LB09-13C	Gastropod	746.2	8287	Aragonite	Micromill	0	2.4492	0.015	1.304511947	0.021
LB09-13C	Gastropod	746.2	8288	Aragonite	Micromill	0	2.4502	0.023	1.304511947	0.051
LB09-13C	Gastropod	746.2	8289	Aragonite	Micromill	0	2.6302	0.012	1.300465615	0.024
LB09-14A	Gastropod	747.8	2864	Aragonite	Dremel	0	1.6234	0.016	1.513100393	0.041
LB09-14A	Gastropod	747.8	9293	Aragonite	Micromill	1	-1.0723	0.025	0.195705539	0.065
LB09-14A	Gastropod	747.8	9294	Aragonite	Micromill	111	-0.89317	0.064	-0.055065924	0.128
LB09-14A	Gastropod	747.8	9295	Aragonite	Micromill	0	-0.31545	0.028	1.058494925	0.056
LB09-14B	Gastropod	747.8	2919	Aragonite	Dremel	0	1.0135	0.02	0.831192191	0.042
LB09-14C	Gastropod	747.8	2852	Aragonite	Dremel	0	1.7569	0.025	1.107152074	0.024
LB09-400	Gastropod	747.8	11693	Aragonite	Crush	0	2.6981	0.04	0.129796427	0.029
LB09-400	Gastropod	747.8	11694	Aragonite	Crush	0	2.5946	0.014	0.088871865	0.02
LB09-401	Ammonite	747.8	11695	Aragonite	Crush	0	-0.60671	0.019	1.339780004	0.026
LB09-401	Ammonite	747.8	11696	Aragonite	Crush	10	-0.79863	0.062	1.268906738	0.031
LB09-402	Ammonite	747.8	11697	Aragonite	Crush	0	0.55885	0.018	1.302793955	0.021
LB09-402	Ammonite	747.8	11698	Aragonite	Crush	0	0.5498	0.026	1.275904099	0.034
LB09-403	Ammonite	747.8	11699	Aragonite	Crush	0	0.59502	0.049	1.481526535	0.026
LB09-403	Ammonite	747.8	11703	Aragonite	Crush	0	0.69851	0.044	1.461534076	0.014
LB09-404	Gastropod	747.8	11704	Aragonite	Crush	0	1.6953	0.031	1.332782643	0.026
LB09-404	Gastropod	747.8	11705	Aragonite	Crush	0	1.7726	0.04	1.281901836	0.034
LB09-405	Gastropod	747.8	11706	Aragonite	Crush	0	6.0119	0.012	-2.166297453	0.031
LB09-405	Gastropod	747.8	11707	Aragonite	Crush	0	5.9918	0.02	-2.138407973	0.028
LB09-406	Gastropod	758.8	11708	Aragonite	Crush	0	2.264	0.017	0.711816881	0.014
LB09-406	Gastropod	758.8	11709	Aragonite	Crush	0	2.5534	0.053	1.559397161	0.035
LB09-17A	Ammonite	769.4	2900	Aragonite	Dremel	0	-4.2963	0.014	-0.07648114	0.017
LB09-17A	Ammonite	769.4	9299	Aragonite	Micromill	0	-1.8604	0.046	0.095194637	0.05
LB09-17A	Ammonite	769.4	9300	Aragonite	Micromill	0	-1.2807	0.017	0.082256488	0.051
LB09-17A	Ammonite	769.4	9301	Aragonite	Micromill	0	-2.4271	0.033	-0.247122067	0.054
LB09-407	Ammonite	769.4	11710	Aragonite	Crush	0	1.2853	0.035	1.464532945	0.025
LB09-407	Ammonite	769.4	11714	Aragonite	Crush	0	1.2843	0.036	1.392660057	0.027
LB09-408	Ammonite	769.4	11715	Aragonite	Crush	0	-1.5583	0.03	1.524410359	0.04
LB09-408	Ammonite	769.4	11716	Aragonite	Crush	0	-4.7374	0.019	1.534406588	0.021
LB09-409	Gastropod	769.4	11717	Aragonite	Crush	0	0.74875	0.036	1.27990259	0.02

LB09-409	Gastropod	769.4	11718	Aragonite	Crush	0	0.85828	0.048	1.235919182	0.016
LB09-410	Gastropod	769.4	11719	Aragonite	Crush	0	-1.5512	0.028	1.23192069	0.025
LB09-410	Gastropod	769.4	11720	Aragonite	Crush	0	-1.7552	0.034	1.222924084	0.022
LB09-18A	Gastropod	779.4	2844	Aragonite	Dremel	0	2.1034	0.025	1.31513357	0.025
LB09-18A	Gastropod	779.4	2942	Aragonite	Dremel	0	2.3401	0.006	1.477694983	0.026
LB09-18A	Gastropod	779.4	2962	Aragonite	Dremel	0	2.2276	0.01	1.365813886	0.026
LB09-18A	Gastropod	779.4	7255	Aragonite	Micromill	0	2.5497	0.021	0.889155905	0.059
LB09-18B	Gastropod	779.4	2866	Aragonite	Dremel	1000	2.6899	0.004	1.173208454	0.026
LB09-18B	Gastropod	779.4	2963	Aragonite	Dremel	0	3.4982	0.044	0.183880132	0.062
LB09-18C	Gastropod	779.4	2934	Aragonite	Dremel	0	3.1537	0.049	0.774341217	0.049
LB09-18D	Gastropod	779.4	2885	Aragonite	Dremel	0	1.9615	0.024	1.327373726	0.018
LB09-19A	Ammonite	783.1	2905	Aragonite	Dremel	0	-1.0641	0.012	1.002554376	0.056
LB09-20A	Gastropod	787.7	2901	Aragonite	Dremel	0	3.0078	0.016	1.373198443	0.017
LB09-20A	Gastropod	787.7	9381	Aragonite	Micromill	0	2.338	0.012	0.950660161	0.031
LB09-20A	Gastropod	787.7	9382	Aragonite	Micromill	0	2.318	0.027	0.930731973	0.031
LB09-20A	Gastropod	787.7	9383	Aragonite	Micromill	0	2.2959	0.025	0.983435455	0.022
LB09-20B	Gastropod	787.7	2845	Aragonite	Dremel	0	1.9508	0.011	1.129204587	0.021
LB09-411	Echinoid	787.7	11721	Calcite	Crush	0	2.264	0.029	1.2002	0.016
LB09-411	Echinoid	787.7	11725	Calcite	Crush	0	2.3604	0.039	1.0913	0.022
LB09-412	Echinoid	787.7	11726	Calcite	Crush	0	2.1957	0.018	0.84362	0.029
LB09-412	Echinoid	787.7	11727	Calcite	Crush	0	2.1806	0.033	0.92552	0.013
LB09-413	Echinoid	787.7	11728	Calcite	Crush	0	1.7003	0.022	1.0743	0.023
LB09-413	Echinoid	787.7	11729	Calcite	Crush	0	1.8028	0.037	1.1322	0.031
LB09-414	Bivalve	787.7	11730	Calcite	Crush	0	3.7732	0.021	0.68783	0.022
LB09-414	Bivalve	787.7	11731	Calcite	Crush	0	3.6576	0.035	0.74775	0.011
LB09-415	Bivalve	787.7	11783	Calcite	Crush	0	-0.69723	0.02	-0.36586	0.02
LB09-415	Bivalve	787.7	11784	Calcite	Crush	0	-1.1275	0.024	-0.47733	0.035
LB09-416	Bivalve	787.7	11785	Calcite	Crush	0	1.595	0.041	0.69762	0.025
LB09-416	Bivalve	787.7	11786	Calcite	Crush	0	1.2341	0.045	0.65243	0.033
LB09-417	Gastropod	787.7	11787	Aragonite	Crush	0	4.2763	0.018	1.334182115	0.027
LB09-417	Gastropod	787.7	11788	Aragonite	Crush	0	4.3105	0.028	1.356273782	0.015
LB09-418	Gastropod	787.7	11789	Aragonite	Crush	0	2.1691	0.04	1.338180607	0.031
LB09-418	Gastropod	787.7	11793	Aragonite	Crush	0	2.4657	0.037	1.104268842	0.044
LB09-419	Echinoid	787.7	11794	Calcite	Crush	0	0.23676	0.022	1.3293	0.02

LB09-419	Echinoid	787.7	11795	Calcite	Crush	0	0.40867	0.018	1.2429	0.036
LB09-21A	Gastropod	791.2	2870	Aragonite	Dremel	0	2.2932	0.02	1.1032069	0.026
LB09-21A	Gastropod	791.2	9311	Aragonite	Micromill	0	1.9592	0.026	1.029563647	0.069
LB09-21A	Gastropod	791.2	9312	Aragonite	Micromill	0	2.1061	0.022	1.131126595	0.038
LB09-21A	Gastropod	791.2	9313	Aragonite	Micromill	0	1.9401	0.016	0.982828505	0.033
LB09-21B	Ammonite	791.2	2926	Aragonite	Dremel	0	-2.8688	0.011	0.86305706	0.04
LB09-420	Echinoid	791.2	11796	Calcite	Crush	10	-1.1326	0.066	1.3263	0.025
LB09-420	Echinoid	791.2	11797	Calcite	Crush	0	-1.225	0.026	1.26	0.019
LB09-421	Echinoid	791.2	11798	Calcite	Crush	0	1.6402	0.025	1.0059	0.012
LB09-421	Echinoid	791.2	11799	Calcite	Crush	0	1.6805	0.033	0.97981	0.034
LB09-422	Gastropod	791.2	11800	Aragonite	Crush	0	1.7227	0.036	1.098271104	0.021
LB09-422	Gastropod	791.2	11804	Aragonite	Crush	0	1.8393	0.025	1.152450667	0.036
LB09-423	Ammonite	791.2	11805	Aragonite	Crush	0	-3.0397	0.014	0.787088487	0.025
LB09-423	Ammonite	791.2	11806	Aragonite	Crush	0	-3.2619	0.037	0.38653958	0.037
LB09-22A	Ammonite	794.9	2909	Aragonite	Dremel	0	-1.8767	0.012	0.981614605	0.045
LB09-22B	Ammonite	794.9	2880	Aragonite	Dremel	0	-1.2027	0.024	1.264149779	0.024
LB09-23A	Gastropod	799.4	2910	Aragonite	Dremel	0	0.86902	0.02	1.357316588	0.051
LB09-23A	Gastropod	799.4	7252	Aragonite	Micromill	0	1.8864	0.023	1.000430052	0.018
LB09-23A	Gastropod	799.4	8378	Aragonite	Micromill	0	1.9586	0.027	0.748647005	0.027
LB09-23A	Gastropod	799.4	8780	Aragonite	Micromill	0	2.3793	0.01	1.377143617	0.036
LB09-23A	Gastropod	799.4	8781	Aragonite	Micromill	0	2.4146	0.016	1.30855828	0.02
LB09-23A	Gastropod	799.4	8782	Aragonite	Micromill	0	2.3521	0.031	1.262834721	0.011
LB09-424	Gastropod	799.4	11807	Aragonite	Crush	0	1.974	0.03	1.490823028	0.029
LB09-424	Gastropod	799.4	11808	Aragonite	Crush	0	1.9509	0.024	1.438542749	0.033
LB09-425	Gastropod	799.4	11840	Aragonite	Crush	0	1.8667	0.021	1.348376761	0.044
LB09-425	Gastropod	799.4	11841	Aragonite	Crush	0	1.8295	0.033	1.35137563	0.011
LB09-426	Gastropod	799.4	11842	Aragonite	Crush	1000	1.7472	0.012	1.316288865	0.041
LB09-426	Gastropod	799.4	11843	Aragonite	Crush	1000	2.5072	0.019	-0.736126934	0.038
LB09-427	Gastropod	799.4	11847	Aragonite	Crush	0	1.7834	0.024	1.627671407	0.016
LB09-427	Gastropod	799.4	11848	Aragonite	Crush	0	1.7171	0.036	1.600681588	0.024
LB09-428	Gastropod	799.4	11849	Aragonite	Crush	0	2.1458	0.024	1.332382794	0.036
LB09-428	Gastropod	799.4	11850	Aragonite	Crush	0	2.0946	0.015	1.27030621	0.012
LB09-24A	Echinoid	806.4	2941	Calcite	Dremel	100	1.9021	0.04	0.425237003	0.12
LB09-24A	Echinoid	806.4	2954	Calcite	Dremel	111	0.13225	0.108	-6.578145907	0.15

LB09-24A	Echinoid	806.4	8795	Calcite	Micromill	0	4.93	0.042	1.006924452	0.034
LB09-24A	Echinoid	806.4	8796	Calcite	Micromill	0	5.0499	0.017	1.1352517	0.021
LB09-24A	Echinoid	806.4	8797	Calcite	Micromill	0	5.3701	0.02	1.271462154	0.036
LB09-24B	Bivalve	806.4	2871	Calcite	Dremel	0	3.1067	0.008	1.057694723	0.022
LB09-24C	Gastropod	806.4	2887	Aragonite	Dremel	0	-0.38093	0.019	1.329396893	0.045
LB09-24C	Gastropod	806.4	2955	Aragonite	Dremel	0	0.059925	0.031	1.36379072	0.041
LB09-24C	Gastropod	806.4	9320	Aragonite	Micromill	0	-0.20575	0.04	0.969880241	0.011
LB09-24C	Gastropod	806.4	9321	Aragonite	Micromill	0	-0.57009	0.029	0.395725876	0.043
LB09-24C	Gastropod	806.4	9322	Aragonite	Micromill	0	-0.34967	0.015	0.968868658	0.034
LB09-24D	Echinoid	806.4	2842	Calcite	Dremel	0	4.3008	0.016	1.145674937	0.023
LB09-24E	Echinoid	806.4	2938	Calcite	Dremel	100	1.7143	0.041	0.56017238	0.108
LB09-24E	Echinoid	806.4	8792	Calcite	Micromill	0	5.1707	0.034	1.006924452	0.029
LB09-24E	Echinoid	806.4	8793	Calcite	Micromill	0	5.075	0.029	1.057654244	0.033
LB09-24E	Echinoid	806.4	8794	Calcite	Micromill	0	5.1627	0.022	0.95620478	0.047
LB09-24G	Echinoid	806.4	8789	Calcite	Micromill	0	4.1516	0.017	1.320238854	0.043
LB09-24G	Echinoid	806.4	8790	Calcite	Micromill	0	4.3178	0.015	1.527084446	0.027
LB09-24G	Echinoid	806.4	8791	Calcite	Micromill	0	4.5423	0.038	1.42366165	0.018
LB09-429	Echinoid	813.9	11851	Calcite	Crush	0	10.0915	0.016	1.2543	0.012
LB09-429	Echinoid	813.9	11852	Calcite	Crush	0	9.0173	0.025	1.2564	0.021
LB09-26A	Ammonite	820.4	7256	Aragonite	Micromill	0	-3.0261	0.027	0.122507382	0.062
LB09-26A	Ammonite	820.4	8383	Aragonite	Micromill	0	-2.8075	0.012	-0.216282943	0.009
LB09-26C	Ammonite	820.4	7251	Aragonite	Micromill	0	0.73447	0.026	0.026174319	0.046
LB09-430	Gastropod	820.4	11814	Aragonite	Crush	0	2.5925	0.035	1.273305079	0.043
LB09-430	Gastropod	820.4	11815	Aragonite	Crush	0	2.6497	0.036	1.418450328	0.026
LB09-431-BD	Ammonite	820.4	11816	Aragonite	Crush	0	-0.44123	0.025	0.454304018	0.019
LB09-431-BD	Ammonite	820.4	11817	Aragonite	Crush	0	-0.46733	0.027	0.426264595	0.041
LB09-432	Echinoid	820.4	11818	Calcite	Crush	0	10.9598	0.028	0.84571	0.04
LB09-432	Echinoid	820.4	11819	Calcite	Crush	0	11.1747	0.04	0.89979	0.02
LB09-27A	Bivalve	820.4	2876	Aragonite	Dremel	0	-10.3158	0.014	-0.765591814	0.018
LB09-27A	Bivalve	820.4	9284	Aragonite	Micromill	0	0.56019	0.033	0.742071715	0.031
LB09-27A	Bivalve	820.4	9285	Aragonite	Micromill	0	0.29045	0.031	0.671372168	0.049
LB09-27A	Bivalve	820.4	9286	Aragonite	Micromill	0	0.92353	0.018	0.799731955	0.021
LB09-27A	Bivalve	820.4	9323	Aragonite	Micromill	0	0.88629	0.02	0.702215339	0.029
LB09-27B	Bivalve	820.4	2920	Aragonite	Dremel	0	-0.29766	0.012	0.818243926	0.036

LB09-27B	Bivalve	820.4	8293	Aragonite	Micromill	0	1.407	0.014	0.728739049	0.032
LB09-27B	Bivalve	820.4	8294	Aragonite	Micromill	0	-0.17693	0.017	0.901699536	0.035
LB09-27B	Bivalve	820.4	8295	Aragonite	Micromill	0	1.1326	0.014	0.965631591	0.018
LB09-27C	Bivalve	820.4	8262	Aragonite	Micromill	0	1.4271	0.03	0.871250883	0.025
LB09-27C	Bivalve	820.4	8263	Aragonite	Micromill	0	1.072	0.023	0.820165934	0.04
LB09-27C	Bivalve	820.4	8264	Aragonite	Micromill	0	0.69789	0.021	0.880253973	0.053
LB09-433	Ammonite	820.4	11820	Aragonite	Crush	0	-2.4992	0.034	0.451295153	0.033
LB09-433	Ammonite	820.4	11824	Aragonite	Crush	0	-2.4811	0.023	0.389218569	0.034
LB09-434	Echinoid	820.4	11825	Calcite	Crush	0	13.3189	0.015	0.57628	0.027
LB09-434	Echinoid	820.4	11826	Calcite	Crush	1	12.7819	0.035	-0.52044	0.12
LB09-435	Gastropod	820.4	11827	Aragonite	Crush	0	2.0273	0.027	1.563595577	0.027
LB09-435	Gastropod	820.4	11828	Aragonite	Crush	0	1.9058	0.017	1.531607644	0.023
LB09-436	Gastropod	820.4	11829	Aragonite	Crush	0	0.79354	0.016	1.261309604	0.017
LB09-436	Gastropod	820.4	11830	Aragonite	Crush	0	0.81362	0.015	1.323386188	0.026
LB09-28A	Ammonite	826.4	2890	Aragonite	Dremel	0	0.65936	0.014	1.299454031	0.028
LB09-28B	Ammonite	826.4	2860	Aragonite	Dremel	0	-0.24464	0.027	-1.177538821	0.031
LB09-28B	Ammonite	826.4	9317	Aragonite	Micromill	0	-0.23091	0.026	1.151054783	0.024
LB09-28B	Ammonite	826.4	9318	Aragonite	Micromill	0	-0.53084	0.007	1.163901889	0.036
LB09-28B	Ammonite	826.4	9319	Aragonite	Micromill	0	-1.3974	0.036	1.046558244	0.054
LB09-28C	Gastropod	826.4	2893	Aragonite	Dremel	0	2.3999	0.015	1.140028527	0.028
LB09-28C	Gastropod	826.4	7265	Aragonite	Micromill	0	1.4876	0.013	1.067902648	0.039
LB09-28C	Gastropod	826.4	8379	Aragonite	Micromill	0	1.5216	0.029	0.738632332	0.03
LB09-28D	Gastropod	826.4	2878	Aragonite	Dremel	0	2.5664	0.029	1.386146708	0.028
LB09-28D	Gastropod	826.4	8232	Aragonite	Micromill	0	2.1723	0.03	1.245536649	0.035
LB09-28D	Gastropod	826.4	8233	Aragonite	Micromill	0	2.2548	0.015	1.09238296	0.035
LB09-28D	Gastropod	826.4	8234	Aragonite	Micromill	0	2.2649	0.024	1.321607702	0.043
LB09-28E	Ammonite	826.4	8278	Aragonite	Micromill	0	-3.573	0.007	-0.487780733	0.043
LB09-28E	Ammonite	826.4	8350	Aragonite	Micromill	0	-3.4515	0.021	-0.641379519	0.03
LB09-28E	Ammonite	826.4	8279	Aragonite	Micromill	0	-2.7398	0.029	0.143963061	0.093
LB09-28E	Ammonite	826.4	8351	Aragonite	Micromill	0	-3.2255	0.016	0.300616828	0.018
LB09-28E	Ammonite	826.4	8280	Aragonite	Micromill	0	-1.1136	0.011	0.449845574	0.018
LB09-28E	Ammonite	826.4	8352	Aragonite	Micromill	0	-1.2845	0.017	0.246729793	0.028
LB09-28G	Echinoid	826.4	8801	Calcite	Micromill	0	4.7568	0.046	0.887573331	0.037
LB09-28G	Echinoid	826.4	8802	Calcite	Micromill	0	4.8142	0.033	0.953219484	0.028

LB09-28G	Echinoid	826.4	8803	Calcite	Micromill	0	4.8454	0.036	1.020849087	0.033
LB09-28J	Rotularia	826.4	7269	Calcite	Micromill	0	1.6471	0.015	0.569310422	0.027
LB09-29A	Ammonite	830.6	2841	Aragonite	Dremel	0	-2.6007	0.02	0.379267418	0.039
LB09-29B	Ammonite	830.6	2928	Aragonite	Dremel	0	-11.9996	0.033	-0.019690862	0.081
LB09-30A	Bivalve	834	2899	Calcite	Dremel	0	1.5361	0.019	0.711359912	0.027
LB09-30A	Bivalve	834	8281	Calcite	Micromill	111	-19.3481	3.323	-23.15837853	7.831
LB09-30A	Bivalve	834	8366	Calcite	Micromill	111	-21.1999	3.633	-19.33193747	2.988
LB09-30A	Bivalve	834	8282	Calcite	Micromill	111	-4.4815	0.274	-12.16753073	0.286
LB09-30A	Bivalve	834	8283	Calcite	Micromill	111	-20.6767	2.534	-33.29522928	3.836
LB09-30B	Bivalve	834	2902	Calcite	Dremel	0	1.8581	0.011	1.058220945	0.02
LB09-30C	Rotularia	834	2930	Calcite	Dremel	0	1.2131	0.036	-0.093010378	0.049
LB09-30D	Rotularia	834	2863	Calcite	Dremel	0	1.3251	0.021	0.436540649	0.04
LB09-30E	Rotularia	834	2891	Calcite	Dremel	11	-2.4575	0.098	-6.502046159	0.067
LB09-30E	Rotularia	834	2949	Calcite	Dremel	111	-5.9126	0.287	-12.69800264	0.387
LB09-30F	Bivalve	834	7253	Aragonite	Micromill	0	3.0191	0.028	0.119533328	0.036
LB09-30F	Bivalve	834	8377	Aragonite	Micromill	0	3.0627	0.029	0.080081585	0.045
LB09-31B	Rotularia	836.4	8301	Calcite	Micromill	0	0.69143	0.027	-0.946764547	0.044
LB09-31B	Rotularia	836.4	8369	Calcite	Micromill	0	0.73491	0.024	-0.891308879	0.03
LB09-31B	Rotularia	836.4	8302	Calcite	Micromill	0	-1.8976	0.033	-3.443686335	0.025
LB09-31B	Rotularia	836.4	8374	Calcite	Micromill	0	-1.8531	0.016	-3.686456675	0.019
LB09-31B	Rotularia	836.4	8303	Calcite	Micromill	0	-2.4041	0.013	-4.205695781	0.031
LB09-31B	Rotularia	836.4	8316	Calcite	Micromill	0	-2.2262	0.026	-3.939650252	0.021
LB09-31B	Rotularia	836.4	8370	Calcite	Micromill	0	-2.3293	0.016	-4.162586083	0.027
LB09-32A	Gastropod	842.9	2923	Aragonite	Dremel	0	-4.8852	0.009	0.228399906	0.026
LB09-32A	Gastropod	842.9	8250	Aragonite	Micromill	0	-3.2588	0.019	0.336780925	0.042
LB09-32A	Gastropod	842.9	8359	Aragonite	Micromill	0	-2.8537	0.018	0.347513823	0.018
LB09-32A	Gastropod	842.9	8251	Aragonite	Micromill	0	-0.51003	0.022	0.461883414	0.061
LB09-32A	Gastropod	842.9	8360	Aragonite	Micromill	0	-0.52193	0.018	0.355495214	0.037
LB09-32A	Gastropod	842.9	8252	Aragonite	Micromill	0	-8.9625	0.018	-0.206640532	0.037
LB09-32A	Gastropod	842.9	8361	Aragonite	Micromill	0	-8.8888	0.012	-0.448784203	0.012
LB09-32A	Gastropod	842.9	8365	Aragonite	Micromill	0	-8.8988	0.007	-0.512655563	0.023
LB09-43A	Bivalve	864.25	8259	Aragonite	Micromill	0	2.7577	0.026	0.561959335	0.031
LB09-43A	Bivalve	864.25	8260	Aragonite	Micromill	0	2.6963	0.013	0.801148171	0.014
LB09-43A	Bivalve	864.25	8261	Aragonite	Micromill	0	1.6141	0.016	0.81318601	0.051

LB09-43B	Bivalve	864.25	8253	Aragonite	Micromill	0	3.681	0.016	1.134363661	0.025
LB09-43B	Bivalve	864.25	8254	Aragonite	Micromill	0	0.44444	0.027	0.847175204	0.033
LB09-43B	Bivalve	864.25	8255	Aragonite	Micromill	0	3.688	0.015	1.211446297	0.027
LB10-10A	Bivalve	867.7	2925	Aragonite	Dremel	111	-0.50532	0.055	-1.082804059	0.108
LB10-10A	Bivalve	867.7	2951	Aragonite	Dremel	111	-5.4707	0.319	-11.13796082	0.348
LB10-10B	Gastropod	867.7	2947	Aragonite	Dremel	0	0.69877	0.04	0.393692593	0.044
LB10-10B	Gastropod	867.7	8244	Aragonite	Micromill	0	0.85881	0.039	0.652030699	0.035
LB10-10B	Gastropod	867.7	8245	Aragonite	Micromill	0	0.27647	0.009	0.714081209	0.031
LB10-10B	Gastropod	867.7	8246	Aragonite	Micromill	0	0.52892	0.033	0.677057266	0.029
LB10-11A	Bivalve	880.2	2855	Aragonite	Dremel	0	-10.2104	0.023	0.828157441	0.015
LB10-11A	Bivalve	880.2	8268	Aragonite	Micromill	0	3.0433	0.023	0.967250124	0.021
LB10-11A	Bivalve	880.2	8271	Aragonite	Micromill	0	3.1369	0.029	0.866192968	0.037
LB10-11A	Bivalve	880.2	8269	Aragonite	Micromill	0	3.3531	0.025	0.901193745	0.027
LB10-11A	Bivalve	880.2	8270	Aragonite	Micromill	0	3.2877	0.02	1.051312684	0.043
LB10-12A	Bivalve	890.9	2937	Aragonite	Dremel	0	-1.5954	0.03	-0.040913876	0.043
LB10-12A	Bivalve	890.9	2960	Aragonite	Dremel	0	4.57	0.031	-1.375677613	0.017
LB10-12B	Bivalve	890.9	2894	Aragonite	Dremel	0	1.6906	0.013	0.268256283	0.038
LB10-12B	Bivalve	890.9	8235	Aragonite	Micromill	1000	4.041	0.015	0.418850666	0.028
LB10-12B	Bivalve	890.9	8356	Aragonite	Micromill	0	3.9096	0.017	-0.186346151	0.043
LB10-12B	Bivalve	890.9	8236	Aragonite	Micromill	0	6.2758	0.027	-1.214431259	0.022
LB10-12B	Bivalve	890.9	8357	Aragonite	Micromill	0	6.2224	0.032	-1.501518557	0.021
LB10-12B	Bivalve	890.9	8237	Aragonite	Micromill	0	2.3685	0.014	0.407844642	0.008
LB10-12B	Bivalve	890.9	8358	Aragonite	Micromill	0	2.3243	0.019	-0.010718119	0.026
LB10-13A	Bivalve	899.9	2854	Aragonite	Dremel	0	-2.5445	0.017	0.42825839	0.048
LB10-14E	Bivalve	910.5	7264	Aragonite	Micromill	0	-7.549	0.01	0.414480627	0.034
LB10-14E	Bivalve	910.5	8376	Aragonite	Micromill	1000	-7.1497	0.011	0.169889937	0.025
LB10-14E	Bivalve	910.5	8313	Aragonite	Micromill	0	-5.2423	0.011	0.593793857	0.024
LB10-14E	Bivalve	910.5	8314	Aragonite	Micromill	0	-4.1107	0.02	0.712745919	0.016
LB10-14E	Bivalve	910.5	8315	Aragonite	Micromill	0	1.412	0.02	0.625780116	0.028
LB10-15A	Bivalve	921.1	2865	Aragonite	Dremel	0	1.1724	0.023	1.425092659	0.037
LB10-15B	Gastropod	921.1	2898	Aragonite	Dremel	0	-1.6058	0.009	0.977669431	0.025
LB10-15C	Bivalve	921.1	2851	Aragonite	Dremel	0	2.7361	0.012	1.281144376	0.065
LB10-15C	Bivalve	921.1	7263	Aragonite	Micromill	0	2.6526	0.037	1.246750549	0.022
LB10-15C	Bivalve	921.1	8375	Aragonite	Micromill	0	2.5755	0.007	1.026023106	0.037

LB10-15D	Bivalve	921.1	2879	Aragonite	Dremel	0	3.2714	0.007	1.579156773	0.023
LB10-15D	Bivalve	921.1	7262	Aragonite	Micromill	0	3.0655	0.02	1.257675647	0.027
LB10-15D	Bivalve	921.1	8384	Aragonite	Micromill	0	3.122	0.019	0.892392971	0.036
LB10-15D	Bivalve	921.1	8296	Aragonite	Micromill	0	3.5045	0.04	1.288528933	0.014
LB10-15D	Bivalve	921.1	8347	Aragonite	Micromill	0	3.5912	0.025	1.137803044	0.031
LB10-15D	Bivalve	921.1	8297	Aragonite	Micromill	0	0.78289	0.029	0.791740448	0.019
LB10-15D	Bivalve	921.1	8348	Aragonite	Micromill	0	0.74897	0.028	0.577031924	0.04
LB10-15D	Bivalve	921.1	8317	Aragonite	Micromill	0	2.0502	0.016	1.165520422	0.01
LB10-15D	Bivalve	921.1	8349	Aragonite	Micromill	0	2.1505	0.02	1.070937398	0.044
LB10-15E	Gastropod	921.1	2882	Aragonite	Dremel	0	-4.2759	0.023	0.821177517	0.027
LB10-17A	Bivalve	930	2872	Aragonite	Dremel	0	0.84101	0.017	1.522103483	0.044

flagged samples (except just 1000, removed)

Appendix 2.2

Sample	PRI#	Group	Strat	Analysis #	Mineralogy	Preparation	Flags	d13C_VPDB	StdDev_d13C	d18O_VPDB	StdDev_d18O
TT1	65708	Gastropod	897	24799	aragonite	crushed	0	2.5308	0.023	1.2602	0.029
TT1	65708	Gastropod	897	25708	aragonite	crushed	0	2.5946	0.015	1.2361	0.046
TT1	65708	Gastropod	897	25954	aragonite	crushed	0	2.5749	0.049	1.2968	0.041
TT2	65709	Bivalve	897	24968	aragonite	micromilled	0	-1.0502	0.028	0.64722	0.015
TT2	65709	Bivalve	897	25776	aragonite	micromilled	10	-1.0078	0.062	0.6495	0.044
TT3	65708	Gastropod	897	24843	aragonite	crushed	0	1.975	0.013	1.4331	0.025
TT3	65708	Gastropod	897	25730	aragonite	crushed	0	1.7586	0.049	1.4299	0.032
TT3	65708	Gastropod	897	25867	aragonite	crushed	0	1.8393	0.047	1.4622	0.025
TT4	65742	Gastropod	897	24825	aragonite	crushed	0	0.96558	0.022	1.3018	0.019
TT4	65742	Gastropod	897	25809	aragonite	crushed	0	1.2208	0.058	1.4223	0.02
TT5	65712	Ammonite	897	24902	aragonite	micromilled	10	-7.2345	0.071	-1.1779	0.076
TT5	65712	Ammonite	897	25962	aragonite	micromilled	10	-7.1836	0.071	-1.2646	0.032
TT6	65761	Ammonite	885	24904	aragonite	crushed	1000	-2.2905	0.052	0.41258	0.068
TT6	65761	Ammonite	885	25940	aragonite	crushed	0	-2.3811	0.012	0.24758	0.03
TT7	60565	Gastropod	1011	25004	aragonite	micromilled	0	2.8449	0.013	0.1778	0.026
TT7	60565	Gastropod	1011	25868	aragonite	micromilled	0	2.8374	0.037	0.014175	0.018
TT8	65714	Gastropod	885	24802	aragonite	crushed	0	1.837	0.057	1.3722	0.055
TT8	65714	Gastropod	885	25810	aragonite	crushed	10	2.1358	0.062	1.4498	0.031
TT8	65714	Gastropod	885	26340	aragonite	crushed	10	2.1132	0.075	1.6028	0.044
TT9	60522	Ammonite	885	24808	aragonite	crushed	0	-4.3805	0.009	0.51834	0.036
TT9	60522	Ammonite	885	25770	aragonite	crushed	10	-3.2461	0.069	0.46002	0.063
TT9	60522	Ammonite	885	26364	aragonite	crushed	10	-2.8713	0.092	1.1096	0.029
TT10	60536	Bivalve	983	24912	aragonite	micromilled	0	2.6918	0.014	1.09	0.016
TT10	60536	Bivalve	983	25850	aragonite	micromilled	0	2.6848	0.046	0.77048	0.043
TT11	65715	Bivalve	659	24911	aragonite	micromilled	0	1.9591	0.02	0.73997	0.016
TT11	65715	Bivalve	659	25862	aragonite	micromilled	0	1.9748	0.05	0.56758	0.038
TT12	58323	Ammonite	862	24949	aragonite	crushed	0	-2.6482	0.041	1.4449	0.043
TT12	58323	Ammonite	862	25792	aragonite	crushed	0	-2.4694	0.049	1.4961	0.08
TT13	65716	Gastropod	997	24969	aragonite	micromilled	0	-1.5602	0.025	1.0493	0.026
TT13	65716	Gastropod	997	25790	aragonite	micromilled	0	-1.5242	0.032	0.9401	0.111
TT14	65717	Bivalve	838	24848	aragonite	micromilled	0	2.165	0.024	0.90513	0.011
TT14	65717	Bivalve	838	25700	aragonite	micromilled	10	2.1319	0.069	0.73267	0.061

TT14	65717	Bivalve	838	25844	aragonite	micromilled	0	2.0361	0.057	0.74452	0.047
TT15	58309	Ammonite	883	24831	aragonite	crushed	0	-1.1598	0.01	1.5845	0.036
TT15	58309	Ammonite	883	25823	aragonite	crushed	0	-1.254	0.024	1.5975	0.011
TT16	60541	Bivalve	975	24868	aragonite	micromilled	0	1.4957	0.027	1.1695	0.018
TT16	60541	Bivalve	975	25723	aragonite	micromilled	10	1.3933	0.068	0.89999	0.014
TT16	60541	Bivalve	975	25903	aragonite	micromilled	0	1.2898	0.024	0.80737	0.049
TT16	60541	Bivalve	975	26339	aragonite	micromilled	10	1.7369	0.127	1.1813	0.052
TT17	60644	Ammonite	975	24958	aragonite	crushed	0	-2.9604	0.018	0.60147	0.011
TT17	60644	Ammonite	975	25777	aragonite	crushed	0	-3.218	0.026	0.61987	0.035
TT18	65718	Bivalve	1046	24823	aragonite	micromilled	0	-0.31247	0.021	0.17314	0.031
TT18	65718	Bivalve	1046	25789	aragonite	micromilled	0	-0.19639	0.046	0.20956	0.034
TT19	65719	Bivalve	883	24803	aragonite	micromilled	0	0.59913	0.015	1.6565	0.029
TT19	65719	Bivalve	883	25816	aragonite	micromilled	0	0.88836	0.026	1.7157	0.051
TT19	65719	Bivalve	883	26350	aragonite	micromilled	0	1.0015	0.047	2.2395	0.046
TT20	60503	Ammonite	883	24957	aragonite	micromilled	0	-7.907	0.022	1.4186	0.028
TT20	60503	Ammonite	883	25758	aragonite	micromilled	0	-7.8567	0.052	1.4049	0.041
TT21	65720	Gastropod	883	24959	aragonite	micromilled	0	2.5262	0.004	0.5009	0.014
TT21	65720	Gastropod	883	25804	aragonite	micromilled	0	2.411	0.042	0.28945	0.023
TT22	60557	Bivalve	1013	24846	aragonite	micromilled	0	3.1046	0.013	1.1231	0.036
TT22	60557	Bivalve	1013	25699	aragonite	micromilled	0	2.998	0.019	0.91662	0.011
TT22	60557	Bivalve	1013	25881	aragonite	micromilled	0	3.0106	0.043	0.98016	0.025
TT23	60562	Bivalve	1013	24937	aragonite	micromilled	0	2.4529	0.042	0.77801	0.042
TT23	60562	Bivalve	1013	25821	aragonite	micromilled	0	2.5165	0.025	0.78203	0.041
TT24	60530	Gastropod	1016	24869	aragonite	micromilled	1000	0.63351	0.017	0.86673	0.028
TT24	60530	Gastropod	1016	25825	aragonite	micromilled	0	0.63324	0.046	0.69644	0.042
TT25	65721	Bivalve	1116	24855	aragonite	micromilled	0	4.5004	0.028	-0.79866	0.034
TT25	65721	Bivalve	1116	25701	aragonite	micromilled	0	4.398	0.032	-0.9943	0.023
TT25	65721	Bivalve	1116	25960	aragonite	micromilled	10	4.4831	0.095	-0.98495	0.057
TT26	65722	Bivalve	1201	24847	aragonite	micromilled	0	-1.1753	0.026	0.95681	0.027
TT26	65722	Bivalve	1201	25698	aragonite	micromilled	0	-1.2772	0.04	0.83427	0.04
TT26	65722	Bivalve	1201	25929	aragonite	micromilled	0	-1.1991	0.044	0.83943	0.037
TT27	65723	Bivalve	1011	25028	aragonite	micromilled	0	0.93279	0.03	1.1653	0.036
TT27	65723	Bivalve	1011	25950	aragonite	micromilled	10	1.0113	0.088	1.1884	0.044
TT28	65724	Gastropod	1011	24987	aragonite	crushed	0	0.9929	0.011	1.4264	0.017

TT28	65724	Gastropod	1011	25892	aragonite	crushed	0	0.60629	0.034	1.3447	0.026
TT28	65724	Gastropod	1011	26343	aragonite	crushed	10	1.5218	0.071	1.7079	0.056
TT29	60586	Gastropod	1009	24924	aragonite	crushed	0	1.4542	0.037	1.2348	0.018
TT29	60586	Gastropod	1009	25943	aragonite	crushed	0	1.6791	0.039	1.1523	0.036
TT30	65725	Bivalve	1009	24895	aragonite	micromilled	0	1.6439	0.034	1.1153	0.055
TT30	65725	Bivalve	1009	25883	aragonite	micromilled	0	1.7441	0.055	1.0744	0.049
TT31	65726	Bivalve	827	24809	aragonite	micromilled	0	1.7607	0.016	1.3013	0.041
TT31	65726	Bivalve	827	25732	aragonite	micromilled	0	1.8058	0.06	1.3114	0.041
TT31	65726	Bivalve	827	25907	aragonite	micromilled	0	2.0527	0.034	1.3965	0.038
TT31	65726	Bivalve	827	26355	aragonite	micromilled	10	2.307	0.08	1.796	0.017
TT32	58307	Bivalve	827	24865	aragonite	micromilled	0	3.3497	0.013	1.1419	0.029
TT32	58307	Bivalve	827	25696	aragonite	micromilled	0	3.2389	0.059	0.93651	0.04
TT32	58307	Bivalve	827	25961	aragonite	micromilled	1000	3.2719	0.059	0.98309	0.055
TT33	65728	Bivalve	822	24880	aragonite	micromilled	1000	2.8021	0.045	1.4029	0.056
TT33	65728	Bivalve	822	25799	aragonite	micromilled	0	2.7947	0.052	1.2232	0.045
TT34	65727	Gastropod	822	24812	aragonite	micromilled	0	0.21562	0.024	0.89903	0.046
TT34	65727	Gastropod	822	25706	aragonite	micromilled	10	0.23721	0.064	0.69843	0.063
TT34	65727	Gastropod	822	25942	aragonite	micromilled	0	0.23299	0.034	0.73021	0.02
TT35	58776	Gastropod	1098	24858	aragonite	crushed	0	-0.20357	0.017	0.87607	0.021
TT35	58776	Gastropod	1098	25733	aragonite	crushed	0	-0.30672	0.038	0.72374	0.043
TT35	58776	Gastropod	1098	25886	aragonite	crushed	0	-0.42199	0.053	0.77595	0.029
TT36	65729	Bivalve	1098	25018	aragonite	micromilled	0	-2.0175	0.016	0.39337	0.023
TT36	65729	Bivalve	1098	25926	aragonite	micromilled	10	-1.8077	0.067	0.27701	0.049
TT37	58310	Ammonite	888	25027	aragonite	crushed	0	-2.4913	0.02	1.2028	0.015
TT37	58310	Ammonite	888	25885	aragonite	crushed	0	-2.4604	0.048	1.1308	0.031
TT38	65730	Gastropod	825	25019	aragonite	crushed	0	1.1525	0.025	1.3779	0.014
TT38	65730	Gastropod	825	25893	aragonite	crushed	0	1.0596	0.038	1.5508	0.028
TT39	65731	Bivalve	825	24835	aragonite	micromilled	0	2.9273	0.033	1.0847	0.02
TT39	65731	Bivalve	825	25756	aragonite	micromilled	10	2.9929	0.062	0.77551	0.03
TT40	65732	Bivalve	709	24916	calcite	micromilled	0	2.0444	0.028	0.7117	0.037
TT40	65732	Bivalve	709	25906	calcite	micromilled	0	2.0919	0.057	0.6147	0.025
TT41	58733	Ammonite	709	24946	aragonite	micromilled	0	1.2504	0.018	-0.58057	0.01
TT41	58733	Ammonite	709	25802	aragonite	micromilled	0	1.1575	0.055	-0.63571	0.054
TT42	65733	Gastropod	869	24860	aragonite	crushed	0	0.99627	0.008	1.6204	0.029

TT42	65733	Gastropod	869	25720	aragonite	crushed	0	0.97684	0.041	1.4899	0.037
TT42	65733	Gastropod	869	25972	aragonite	crushed	0	0.95987	0.054	1.4676	0.06
TT43	65734	Bivalve	869	24985	aragonite	crushed	0	0.60544	0.015	0.74705	0.025
TT43	65734	Bivalve	869	24971	aragonite	micromilled	0	2.4017	0.031	1.5401	0.029
TT43	65734	Bivalve	869	25764	aragonite	micromilled	0	5.7717	0.028	0.91587	0.048
TT43	65734	Bivalve	869	26342	aragonite	micromilled	0	2.5626	0.051	1.6887	0.017
TT43	65734	Bivalve	869	26367	aragonite	micromilled	10	2.873	0.065	1.8272	0.044
TT44	58748	Gastropod	1015	24813	aragonite	crushed	0	1.6131	0.022	1.2582	0.047
TT44	58748	Gastropod	1015	25801	aragonite	crushed	10	1.5834	0.061	1.2048	0.07
TT45	65735	Ammonite	1015	24853	aragonite	micromilled	0	-2.1611	0.018	0.46347	0.049
TT45	65735	Ammonite	1015	25728	aragonite	micromilled	10	-1.9235	0.085	0.50953	0.043
TT45	65735	Ammonite	1015	25905	aragonite	micromilled	0	-1.8483	0.038	0.60541	0.053
TT45	65735	Ammonite	1015	26330	aragonite	micromilled	10	-1.8904	0.077	0.75795	0.063
TT46	65736	Bivalve	1015	24935	calcite	micromilled	0	2.8153	0.032	0.55245	0.056
TT46	65736	Bivalve	1015	25752	calcite	micromilled	0	2.8913	0.052	0.72335	0.069
TT47	65737	Bivalve	955	24893	calcite	micromilled	10	2.3886	0.069	0.59023	0.057
TT47	65737	Bivalve	955	25836	calcite	micromilled	0	2.4639	0.058	0.65743	0.034
TT48	65738	Gastropod	928	24871	aragonite	crushed	0	2.3097	0.015	1.3444	0.023
TT48	65738	Gastropod	928	25811	aragonite	crushed	0	2.4894	0.033	1.3071	0.043
TT49	65739	Bivalve	928	24915	calcite	micromilled	0	2.4991	0.01	1.2404	0.019
TT49	65739	Bivalve	928	25917	calcite	micromilled	0	2.6317	0.06	1.2995	0.039
TT50	58226	Bivalve	852	24864	aragonite	micromilled	0	1.0867	0.014	0.70058	0.024
TT50	58226	Bivalve	852	25721	aragonite	micromilled	10	1.1304	0.071	0.50341	0.037
TT50	58226	Bivalve	852	25871	aragonite	micromilled	0	1.0299	0.05	0.50269	0.03
TT51	58219	Gastropod	852	24982	aragonite	crushed	0	1.9545	0.016	1.0986	0.009
TT51	58219	Gastropod	852	25941	aragonite	crushed	0	1.0967	0.036	1.1395	0.03
TT51	58219	Gastropod	852	26334	aragonite	crushed	10	1.8373	0.1	1.7443	0.055
TT52	58224	Gastropod	853	24879	aragonite	micromilled	0	0.66868	0.051	1.2094	0.064
TT52	58224	Gastropod	853	25805	aragonite	micromilled	0	0.56093	0.048	1.0864	0.022
TT53	58702	Gastropod	918	25014	aragonite	crushed	0	1.3292	0.023	1.3116	0.035
TT53	58702	Gastropod	918	25896	aragonite	crushed	10	1.3953	0.07	1.3615	0.034
TT54	58699	Bivalve	918	24910	calcite	micromilled	0	2.6827	0.026	0.86103	0.028
TT54	58699	Bivalve	918	25928	calcite	micromilled	0	2.8873	0.059	0.9376	0.043
TT55	58700	Belemnite	484	24986	aragonite	crushed	0	0.7008	0.02	0.66584	0.016

TT55	58700	Belemnite	484	25859	aragonite	crushed	0	0.78786	0.024	0.59808	0.045
TT56	58704	Bivalve	918	24962	aragonite	micromilled	0	3.284	0.026	0.41892	0.014
TT56	58704	Bivalve	918	25775	calcite	micromilled	10	3.1851	0.074	0.80488	0.053
TT56	58704	Bivalve	918	26351	calcite	micromilled	0	3.6388	0.034	1.0814	0.028
TT57	65740	Bivalve	431	24992	aragonite	micromilled	0	1.6414	0.012	0.75773	0.034
TT57	65740	Bivalve	431	25959	aragonite	micromilled	10	1.4923	0.086	0.7318	0.04
TT58	65741	Ammonite	986	24891	aragonite	micromilled	0	-3.263	0.019	0.43226	0.065
TT58	65741	Ammonite	986	25894	aragonite	micromilled	0	-3.1671	0.042	0.43144	0.045
TT59	68148	Bivalve	950	24991	aragonite	micromilled	0	1.6072	0.027	1.2637	0.038
TT59	68148	Bivalve	950	25902	aragonite	crushed	0	1.8235	0.027	1.3201	0.032
TT60	65743	Gastropod	919	24807	aragonite	crushed	0	1.5931	0.03	1.0003	0.022
TT60	65743	Gastropod	919	25820	aragonite	crushed	10	1.6487	0.064	1.0857	0.037
TT61	65746	Ammonite	917	25005	aragonite	crushed	0	-0.49171	0.017	0.77181	0.028
TT61	65746	Ammonite	917	25953	aragonite	crushed	10	-0.19483	0.061	0.75499	0.032
TT61	65746	Ammonite	917	26354	aragonite	crushed	10	-0.15895	0.065	0.99638	0.017
TT62	58685	Gastropod	917	24857	aragonite	micromilled	0	3.7005	0.018	1.5303	0.038
TT62	58685	Gastropod	917	25717	aragonite	micromilled	0	3.6524	0.054	1.2836	0.042
TT62	58685	Gastropod	917	25952	aragonite	micromilled	10	3.6284	0.079	1.2908	0.066
TT63	65745	Bivalve	940	24951	aragonite	micromilled	0	3.8783	0.018	0.72039	0.029
TT63	65745	Bivalve	940	25780	aragonite	micromilled	10	3.8001	0.074	0.64661	0.04
TT64	65748	Gastropod	873	25007	aragonite	crushed	0	2.9824	0.005	1.7037	0.026
TT64	65748	Gastropod	873	25916	aragonite	crushed	10	2.7071	0.08	1.6099	0.029
TT64	65748	Gastropod	873	26366	aragonite	crushed	10	3.2371	0.068	2.0718	0.035
TT65	65747	Gastropod	925	25016	aragonite	micromilled	0	-0.7005	0.021	0.76187	0.019
TT65	65747	Gastropod	925	25891	aragonite	micromilled	0	-0.70544	0.035	0.70584	0.052
TT66	65749	Ammonite	873	24936	aragonite	micromilled	0	-4.2603	0.029	1.0822	0.017
TT66	65749	Ammonite	873	25768	aragonite	micromilled	0	-3.9919	0.052	1.0026	0.023
TT66	65749	Ammonite	873	26352	aragonite	micromilled	10	-3.6889	0.081	1.2251	0.062
TT68	65749	Ammonite	863	24800	aragonite	micromilled	0	-3.7029	0.045	0.21365	0.048
TT68	65749	Ammonite	863	25718	aragonite	micromilled	1000	-3.7309	0.056	0.12317	0.063
TT68	65749	Ammonite	863	25915	aragonite	micromilled	10	-3.6515	0.065	0.28831	0.031
TT69	58764	Gastropod	867	24814	aragonite	crushed	0	1.1734	0.013	1.6113	0.02
TT69	58764	Gastropod	867	25745	aragonite	crushed	0	1.7006	0.03	1.654	0.031
TT69	58764	Gastropod	867	26361	aragonite	crushed	110.1	171.4923	24.768	419.4509	28.812

TT70	65750	Gastropod	867	24818	aragonite	crushed	0	1.6553	0.018	1.2364	0.011
TT70	65750	Gastropod	867	25719	aragonite	crushed	0	1.6402	0.06	1.1762	0.035
TT70	65750	Gastropod	867	25848	aragonite	crushed	0	1.539	0.038	1.3351	0.021
TT72	65751	Gastropod	885	24810	aragonite	crushed	0	-0.50523	0.013	1.5012	0.05
TT72	65751	Gastropod	885	25742	aragonite	crushed	10	-0.39283	0.071	1.4655	0.028
TT73	58657	Gastropod	#N/A	25003	aragonite	crushed	0	3.1159	0.014	1.1333	0.015
TT73	58657	Gastropod	#N/A	25938	aragonite	crushed	0	3.2438	0.034	1.229	0.037
TT74	65752	Bivalve	#N/A	24952	aragonite	micromilled	0	1.7453	0.008	0.71329	0.028
TT74	65752	Bivalve	#N/A	25788	calcite	micromilled	0	1.8004	0.04	0.99232	0.044
TT75	58601	Gastropod	#N/A	24811	aragonite	crushed	0	-1.6357	0.015	1.0995	0.039
TT75	58601	Gastropod	#N/A	25734	aragonite	crushed	0	-1.6304	0.051	1.0935	0.044
TT75	58601	Gastropod	#N/A	25849	aragonite	crushed	0	-1.9466	0.041	1.0543	0.043
TT76	58040	Gastropod	785	24939	aragonite	crushed	0	4.5036	0.018	1.4033	0.019
TT76	58040	Gastropod	785	25759	aragonite	crushed	10	4.1443	0.065	1.4251	0.032
TT76	58040	Gastropod	785	26356	aragonite	crushed	10	4.6136	0.068	1.713	0.048
TT77	65753	Ammonite	925	24963	aragonite	crushed	1000	-2.4204	0.015	1.3189	0.026
TT77	65753	Ammonite	925	25779	aragonite	crushed	0	-2.4631	0.043	1.3155	0.015
TT78	65754	Bivalve	693	24798	aragonite	micromilled	1010	3.3269	0.062	1.2388	0.063
TT78	65754	Bivalve	693	25757	aragonite	micromilled	0	3.2908	0.044	1.2523	0.042
TT79	65755	Ammonite	769	24890	aragonite	micromilled	10	-1.2818	0.079	0.88159	0.083
TT79	65755	Ammonite	769	25974	aragonite	micromilled	0	-1.4102	0.053	0.82716	0.075
TT80	65756	Ammonite	769	24894	aragonite	micromilled	10	-2.5685	0.121	1.0373	0.053
TT80	65756	Ammonite	769	25845	aragonite	micromilled	0	-2.5049	0.024	1.0491	0.046
TT81	65757	Bivalve	693	24905	aragonite	micromilled	0	3.3582	0.04	1.3263	0.031
TT81	65757	Bivalve	693	25861	aragonite	micromilled	10	3.3044	0.068	1.2097	0.052
TT82	65758	Gastropod	1058	24947	aragonite	micromilled	0	-2.4545	0.052	-0.77316	0.042
TT82	65758	Gastropod	1058	25794	aragonite	micromilled	0	-2.4282	0.023	-0.83201	0.022
TT83	58105	Bivalve	785	24830	aragonite	micromilled	0	6.2073	0.026	1.0295	0.015
TT83	58105	Bivalve	785	25702	aragonite	micromilled	10	6.2155	0.067	0.90532	0.044
TT83	58105	Bivalve	785	25847	aragonite	micromilled	10	6.2046	0.061	0.9802	0.04
TT83	58105	Bivalve	785	26341	aragonite	micromilled	0	6.4232	0.027	1.2106	0.04
TT84	65759	Ammonite	845	24993	aragonite	micromilled	0	-1.6772	0.013	0.74204	0.029
TT84	65759	Ammonite	845	25897	aragonite	micromilled	10	-1.982	0.083	0.63505	0.061
TT84	65759	Ammonite	845	26344	aragonite	micromilled	10	-1.2281	0.077	1.0445	0.058

TT85	65760	Bivalve	845	24906	aragonite	micromilled	0	3.6252	0.007	0.8397	0.039
TT85	65760	Bivalve	845	25826	aragonite	micromilled	0	3.7017	0.04	0.68962	0.056
TT86	60924	Bivalve	409	24824	aragonite	micromilled	0	-5.1416	0.024	-0.0011902	0.025
TT86	60924	Bivalve	409	25869	aragonite	micromilled	10	-5.0356	0.062	0.023407	0.036
TT86	60924	Bivalve	409	25710	aragonite	micromilled	10	-4.9161	0.061	-0.080529	0.05
TT87	68147	Ammonite	731	24829	aragonite	micromilled	0	-19.5846	0.022	0.4918	0.045
TT87	68147	Ammonite	731	25765	aragonite	micromilled	0	-19.6444	0.026	0.40819	0.028
TT88	65762	Gastropod	344	24981	aragonite	crushed	0	-0.48468	0.021	0.60642	0.029
TT88	65762	Gastropod	344	25846	aragonite	crushed	0	-0.67628	0.046	0.64636	0.064
TT89	65763	Bivalve	344	25002	aragonite	micromilled	0	2.7827	0.018	0.85361	0.038
TT89	65763	Bivalve	344	25840	aragonite	micromilled	0	2.7762	0.041	0.81357	0.019
TT90	65764	Bivalve	1055	24892	aragonite	micromilled	0	-4.2145	0.05	0.63982	0.039
TT90	65764	Bivalve	1055	25839	aragonite	micromilled	0	-4.1659	0.037	0.56434	0.046
TT91	61218	Gastropod	1053	24881	aragonite	micromilled	1010	-0.61558	0.105	0.79784	0.093
TT91	61218	Gastropod	1053	25814	aragonite	micromilled	0	-0.67148	0.055	0.60106	0.042
TT92	61219	Bivalve	1053	24970	aragonite	micromilled	0	0.16834	0.033	-0.15503	0.022
TT92	61219	Bivalve	1053	25747	aragonite	micromilled	0	0.0943	0.044	-0.31523	0.043
TT93	65765	Gastropod	497	24917	aragonite	micromilled	0	-0.16469	0.014	0.53705	0.016
TT93	65765	Gastropod	497	25964	aragonite	crushed	0	0.1416	0.043	0.35673	0.024
TT93	65765	Gastropod	497	26331	aragonite	micromilled	10	0.3249	0.061	0.73999	0.029
TT94	65766	Bivalve	497	24876	aragonite	micromilled	0	0.15819	0.039	0.046429	0.037
TT94	65766	Bivalve	497	25748	aragonite	micromilled	10	0.203	0.062	-0.08232	0.028
TT95	65767	Gastropod	659	25030	aragonite	crushed	0	0.78318	0.016	0.89927	0.028
TT95	65767	Gastropod	659	25908	aragonite	crushed	0	0.46355	0.025	0.8558	0.04
TT95	65767	Gastropod	659	26332	aragonite	crushed	10	1.0339	0.09	1.2774	0.052
TT96	65768	Gastropod	497	24913	aragonite	crushed	0	3.4234	0.017	1.3798	0.017
TT96	65768	Gastropod	497	25963	aragonite	micromilled	10	3.5491	0.068	1.4579	0.059
TT97	65769	Bivalve	659	24938	calcite	micromilled	0	2.9448	0.03	0.063776	0.038
TT97	65769	Bivalve	659	25755	calcite	micromilled	10	2.7997	0.065	0.0077896	0.038
TT98	65770	Bivalve	659	24923	aragonite	micromilled	0	0.83095	0.05	1.4259	0.034
TT98	65770	Bivalve	659	25901	aragonite	micromilled	0	0.64649	0.026	1.3448	0.026
TT99	61452	Bivalve	663	25006	aragonite	micromilled	0	2.082	0.028	1.6327	0.016
TT99	61452	Bivalve	663	25904	aragonite	micromilled	10	2.1733	0.07	1.5733	0.06
TT100	65791	Gastropod	692	24997	aragonite	micromilled	0	2.4514	0.018	0.84429	0.024

TT100	65791	Gastropod	692	25860	aragonite	micromilled	0	2.3213	0.037	0.73105	0.023
TT101	65773	Bivalve	672	24833	aragonite	micromilled	0	-2.8656	0.027	0.81576	0.029
TT101	65773	Bivalve	672	25837	aragonite	micromilled	0	-2.6968	0.043	0.56616	0.034
TT101	65773	Bivalve	672	25709	aragonite	micromilled	10	-2.7203	0.068	0.57212	0.05
TT102	61419	Gastropod	692	24927	aragonite	crushed	0	2.3104	0.029	1.3192	0.021
TT102	61419	Gastropod	692	25856	aragonite	crushed	10	2.2671	0.068	1.2573	0.044
TT103	61421	Bivalve	672	24921	calcite	micromilled	0	2.8855	0.025	0.7504	0.032
TT103	61421	Bivalve	672	25927	calcite	micromilled	10	2.8592	0.068	0.63829	0.042
TT104	61453	Bivalve	715	24820	aragonite	micromilled	0	-1.7763	0.027	1.2849	0.021
TT104	61453	Bivalve	715	25774	aragonite	micromilled	10	-1.3067	0.068	1.2156	0.041
TT104	61453	Bivalve	715	26346	aragonite	micromilled	10	-1.084	0.121	1.589	0.065
TT105	61609	Bivalve	769	24960	aragonite	micromilled	0	2.4931	0.017	1.286	0.024
TT105	61609	Bivalve	769	25793	aragonite	micromilled	0	2.2282	0.033	1.3331	0.038
TT106	65788	Gastropod	769	24961	aragonite	crushed	0	3.2871	0.028	1.4985	0.025
TT106	65788	Gastropod	769	25791	aragonite	crushed	0	3.2507	0.045	1.4607	0.039
TT107	61598	Bivalve	785	25763	aragonite	micromilled	0	5.4879	0.033	1.0341	0.037
TT107	61598	Bivalve	785	26345	aragonite	micromilled	0	6.0093	0.044	1.3047	0.041
TT108	65790	Bivalve	785	24996	aragonite	micromilled	0	4.1157	0.012	1.3586	0.032
TT108	65790	Bivalve	785	25958	aragonite	micromilled	10	4.1406	0.077	1.3108	0.032
TT109	61695	Gastropod	955	25008	aragonite	micromilled	0	1.7668	0.015	0.88339	0.009
TT109	61695	Gastropod	955	25937	aragonite	micromilled	0	1.7524	0.022	0.80066	0.01
TT110	61690	Ammonite	863	24889	aragonite	crushed	0	-0.97265	0.055	1.3391	0.039
TT110	61690	Ammonite	863	25851	aragonite	crushed	0	-1.1342	0.025	1.34	0.054
TT111	65776	Bivalve	955	24914	calcite	micromilled	0	2.5793	0.034	0.93697	0.023
TT111	65776	Bivalve	955	25932	calcite	micromilled	10	2.6553	0.066	0.82099	0.05
TT112	61673	Gastropod	950	24925	aragonite	crushed	1010	0.38532	0.095	1.1752	0.072
TT112	61673	Gastropod	950	25913	aragonite	crushed	10	0.5108	0.115	1.3083	0.046
TT113	65777	Ammonite	709	24940	aragonite	micromilled	1000	-7.0568	0.051	0.59764	0.042
TT113	65777	Ammonite	709	25803	aragonite	micromilled	0	-7.4562	0.048	0.71582	0.059
TT113	65777	Ammonite	709	26357	aragonite	micromilled	10	-7.438	0.073	1.0275	0.069
TT114	61829	Bivalve	1074	24854	aragonite	micromilled	10	3.1267	0.078	-0.82087	0.042
TT114	61829	Bivalve	1074	25712	aragonite	micromilled	0	3.3573	0.036	-0.67608	0.027
TT114	61829	Bivalve	1074	25858	aragonite	micromilled	10	3.1929	0.066	-0.59582	0.015
TT115	65778	Bivalve	1046	24922	aragonite	micromilled	0	-1.1423	0.032	1.2699	0.028

TT115	65778	Bivalve	1046	25931	aragonite	micromilled	0	-1.0987	0.039	1.1565	0.032
TT116	61821	Bivalve	1046	24956	aragonite	micromilled	0	1.5445	0.02	1.0026	0.035
TT116	61821	Bivalve	1046	25812	aragonite	micromilled	10	1.9088	0.062	0.75633	0.045
TT116	61821	Bivalve	1046	26365	aragonite	micromilled	10	1.8302	0.064	0.64415	0.033
TT117	65779	Bivalve	1074	24877	aragonite	micromilled	0	3.9245	0.019	1.4089	0.012
TT117	65779	Bivalve	1074	25767	aragonite	micromilled	0	4.0426	0.052	1.4324	0.055
TT118	65780	Bivalve	1073	24797	aragonite	micromilled	0	2.5739	0.05	1.7484	0.03
TT118	65780	Bivalve	1073	25815	aragonite	micromilled	0	3.1503	0.049	1.6062	0.03
TT118	65780	Bivalve	1073	26328	aragonite	micromilled	10	3.1519	0.111	1.6651	0.05
TT119	65781	Gastropod	1046	24866	aragonite	crushed	0	-0.95926	0.027	1.0724	0.028
TT119	65781	Gastropod	1046	25731	aragonite	crushed	0	-1.9395	0.056	0.94011	0.046
TT119	65781	Gastropod	1046	25918	aragonite	crushed	10	-1.5397	0.062	0.96424	0.023
TT119	65781	Gastropod	1046	26333	aragonite	crushed	10	-1.4796	0.09	1.3016	0.056
TT120	65782	Bivalve	1046	24867	aragonite	micromilled	0	-2.8444	0.011	0.79238	0.033
TT120	65782	Bivalve	1046	25697	aragonite	micromilled	0	-2.7574	0.028	0.58163	0.038
TT120	65782	Bivalve	1046	25882	aragonite	micromilled	0	-2.757	0.02	0.63367	0.021
TT121	65783	Gastropod	1067	24967	aragonite	micromilled	0	-2.3822	0.058	0.86131	0.084
TT121	65783	Gastropod	1067	25800	aragonite	micromilled	0	-2.5849	0.029	0.37794	0.064
TT121	65783	Gastropod	1067	26335	aragonite	micromilled	10	-2.2688	0.122	0.69654	0.083
TT122	65784	Gastropod	1104	24870	aragonite	micromilled	0	0.95909	0.022	-0.23745	0.019
TT122	65784	Gastropod	1104	25813	aragonite	micromilled	0	0.89841	0.046	-0.36752	0.032
TT123	61919	Gastropod	1149	24926	aragonite	micromilled	0	-1.7665	0.058	0.53098	0.053
TT123	61919	Gastropod	1149	25855	aragonite	micromilled	0	-1.791	0.055	0.33866	0.04
TT124	65785	Gastropod	900	25013	aragonite	micromilled	0	-2.3698	0.023	0.495	0.008
TT124	65785	Gastropod	900	25939	aragonite	micromilled	0	-0.95205	0.038	0.38193	0.027
TT124	65785	Gastropod	900	26329	aragonite	micromilled	10	-0.8132	0.078	0.6663	0.037
TT125	65771	Bivalve	982	24998	aragonite	micromilled	0	3.3348	0.019	0.61134	0.024
TT125	65771	Bivalve	982	25835	aragonite	micromilled	0	3.3556	0.057	0.51669	0.041
TT126	65772	Gastropod	982	24972	aragonite	micromilled	10	2.4599	0.062	1.3392	0.042
TT126	65772	Gastropod	982	25744	aragonite	micromilled	0	2.4243	0.049	1.2688	0.068
TT127	65774	Gastropod	982	24973	aragonite	micromilled	0	2.202	0.025	0.81617	0.057
TT127	65774	Gastropod	982	25798	aragonite	micromilled	0	2.3287	0.021	0.69444	0.026
TT128	65789	Ammonite	871	24856	aragonite	micromilled	0	-3.7298	0.009	0.38866	0.026
TT128	65789	Ammonite	871	25707	aragonite	micromilled	1010	-3.6807	0.062	0.21477	0.041

TT128	65789	Ammonite	871	25948	aragonite	micromilled	0	-3.7972	0.06	0.25568	0.021
TT129	65775	Bivalve	982	24941	aragonite	micromilled	1000	1.3909	0.036	0.5223	0.037
TT129	65775	Bivalve	982	25778	aragonite	micromilled	0	1.5235	0.029	0.50907	0.025
TT130	65786	Bivalve	838	24822	aragonite	micromilled	0	1.8671	0.016	1.6477	0.032
TT130	65786	Bivalve	838	25724	aragonite	micromilled	0	2.0747	0.049	1.4824	0.042
TT130	65786	Bivalve	838	25914	aragonite	micromilled	10	2.0909	0.071	1.5595	0.041
TT131	61233	Gastropod	997	25015	aragonite	crushed	0	0.39263	0.029	1.4383	0.02
TT131	61233	Gastropod	997	25890	aragonite	crushed	0	0.34897	0.056	1.4818	0.047
TT132	65792	Bivalve	997	24950	aragonite	micromilled	0	0.28779	0.048	0.4696	0.06
TT132	65792	Bivalve	997	25766	aragonite	micromilled	0	0.29559	0.034	0.38363	0.042
TT133	61209	Bivalve	997	24995	calcite	micromilled	0	2.4002	0.017	1.2279	0.032
TT133	61209	Bivalve	997	25884	calcite	micromilled	0	2.3472	0.054	1.2114	0.043
TT134	65793	Ammonite	997	24819	aragonite	crushed	0	-0.57752	0.021	1.5339	0.045
TT134	65793	Ammonite	997	25729	aragonite	crushed	10	-1.4127	0.061	1.4515	0.074
TT134	65793	Ammonite	997	25834	aragonite	crushed	0	-1.2417	0.037	1.5391	0.051
TT134	65793	Ammonite	997	26363	aragonite	crushed	10	-0.86291	0.067	1.8464	0.026
TT135	62135	Bivalve	953	25029	aragonite	micromilled	0	1.2662	0.012	1.04	0.045
TT135	62135	Bivalve	953	25857	aragonite	micromilled	0	1.2367	0.047	0.9353	0.053
TT136	65794	Gastropod	659	24878	aragonite	micromilled	0	0.7139	0.031	0.76521	0.024
TT136	65794	Gastropod	659	25754	aragonite	micromilled	0	0.63276	0.041	0.53339	0.058
TT137	65795	Gastropod	958	24994	aragonite	micromilled	0	0.23805	0.019	0.77788	0.03
TT137	65795	Gastropod	958	25872	aragonite	micromilled	0	0.26265	0.053	0.77771	0.023
TT138	65796	Gastropod	897	24900	aragonite	crushed	0	-0.15566	0.023	1.4751	0.05
TT138	65796	Gastropod	897	25930	aragonite	crushed	0	-0.15868	0.029	1.3352	0.046
TT139	65797	Gastropod	931	24983	aragonite	crushed	0	0.81021	0.023	1.6166	0.026
TT139	65797	Gastropod	931	25880	aragonite	crushed	0	0.8043	0.017	1.6375	0.012
TT140	65798	Bivalve	1071	24844	aragonite	micromilled	0	-0.45379	0.038	0.10218	0.027
TT140	65798	Bivalve	1071	25769	aragonite	micromilled	0	-0.48945	0.032	0.050487	0.022
TT141	65799	Gastropod	672	24859	aragonite	crushed	0	0.15115	0.012	0.99066	0.034
TT141	65799	Gastropod	672	25722	aragonite	crushed	0	0.178	0.037	0.79259	0.03
TT141	65799	Gastropod	672	25973	aragonite	crushed	0	0.12231	0.056	0.87528	0.048
TT142	62079	Gastropod	672	24903	aragonite	micromilled	1010	-0.28112	0.075	0.7331	0.086
TT142	62079	Gastropod	672	25866	aragonite	micromilled	0	-0.42322	0.022	0.58405	0.046
TT143	62139	Bivalve	1168	25951	aragonite	crushed	10	0.77027	0.099	0.71959	0.068

TT143	62139	Bivalve	1168	26353	aragonite	crushed	0	1.112	0.044	1.1298	0.039
TT144	65797	Gastropod	931	24875	aragonite	micromilled	0	0.42147	0.023	1.0935	0.017
TT144	65797	Gastropod	931	25713	aragonite	micromilled	10	0.38875	0.068	1.0135	0.043
TT144	65797	Gastropod	931	25838	aragonite	micromilled	0	0.38015	0.043	0.8193	0.057
TT145	62119	Gastropod	957	24834	aragonite	crushed	0	-0.10967	0.017	1.4159	0.03
TT145	62119	Gastropod	957	25743	aragonite	crushed	0	-0.068747	0.033	1.3343	0.027
TT146	61030	Bivalve	962	24899	aragonite	micromilled	0	3.6141	0.055	-0.028197	0.036
TT146	61030	Bivalve	962	25949	aragonite	micromilled	0	3.5772	0.051	-0.099765	0.055
TT147	61026	Gastropod	822	25017	aragonite	crushed	0	2.8268	0.018	1.471	0.019
TT147	61026	Gastropod	822	25895	aragonite	crushed	10	2.89	0.069	1.538	0.023
TT148	65802	Bivalve	1028	24948	calcite	micromilled	0	2.0875	0.032	0.56604	0.022
TT148	65802	Bivalve	1028	25753	calcite	micromilled	0	2.0438	0.037	0.56037	0.03
TT149	65803	Bivalve	968	24821	calcite	micromilled	0	2.3179	0.019	1.1265	0.052
TT149	65803	Bivalve	968	25824	aragonite	micromilled	10	2.3578	0.067	0.62202	0.027
TT149	65803	Bivalve	968	26362	calcite	micromilled	10	2.807	0.079	1.4727	0.055
TT150	65804	Bivalve	1023	24945	calcite	micromilled	0	3.3784	0.022	0.77805	0.011
TT150	65804	Bivalve	1023	25822	calcite	micromilled	0	3.5088	0.049	0.95862	0.052
TT151	65805	Bivalve	1017	24901	calcite	micromilled	1000	3.306	0.047	0.8886	0.052
TT151	65805	Bivalve	1017	25936	calcite	micromilled	10	3.286	0.068	0.63032	0.052
TT152	60966	Gastropod	827	24801	aragonite	crushed	0	2.8199	0.016	1.2532	0.008
TT152	60966	Gastropod	827	25746	aragonite	crushed	0	2.8711	0.044	1.2494	0.06
TT153	60948	Bivalve	827	24849	aragonite	micromilled	0	-2.1189	0.019	-0.016115	0.031
TT153	60948	Bivalve	827	25711	aragonite	micromilled	0	-2.0901	0.057	-0.11796	0.057
TT153	60948	Bivalve	827	25947	aragonite	micromilled	0	-2.0718	0.025	-0.1182	0.051
TT154	60967	Bivalve	1020	25009	calcite	micromilled	0	2.874	0.016	1.033	0.013
TT154	60967	Bivalve	1020	25912	calcite	micromilled	0	2.8528	0.045	1.0079	0.015
TT155	65806	Bivalve	1031	24984	calcite	micromilled	0	5.2911	0.034	-1.6592	0.037
TT155	65806	Bivalve	1031	25870	calcite	micromilled	0	5.2395	0.045	-1.4801	0.047

flagged samples (except just 1000, removed)

Appendix 3.1.

Paleomagnetic and fossil sampling localities and GPS points.

Horizon	Long	Lat
LB05-01	-56.81244	-64.25027
LB05-02	-56.81210	-64.25101
LB05-04	-56.81099	-64.25130
LB05-05	-56.81005	-64.25138
LB05-06	-56.80970	-64.25210
LB05-07	-56.80914	-64.25213
LB05-08	-56.80882	-64.25232
LB05-09	-56.80836	-64.25263
LB05-10	-56.80794	-64.25266
LB05-11	-56.80374	-64.25134
LB05-12	-56.80075	-64.25028
LB05-13	-56.79858	-64.24982
LB05-14	-56.79561	-64.24965
LB05-15	-56.79314	-64.24930
LB05-16	-56.79165	-64.24928
LB05-17	-56.79122	-64.24944
LB06-01	-56.78983	-64.25019
LB06-02	-56.78970	-64.25027
LB06-03	-56.78941	-64.25035
LB06-04	-56.78817	-64.25075
LB06-05	-56.78662	-64.25114
LB06-06	-56.78390	-64.25056
LB06-07	-56.78272	-64.25057
LB06-08	-56.78229	-64.25064
LB06-09	-56.78220	-64.25075
LB06-10	-56.78126	-64.25085
LB06-11	-56.78068	-64.25107
LB06-12	-56.77991	-64.25120
LB06-13	-56.77818	-64.25144
LB06-14	-56.77710	-64.25144
LB06-15	-56.77572	-64.25171
LB06-16	-56.77484	-64.25182
LB06-17	-56.77431	-64.25189
LB06-18	-56.77320	-64.25205
LB07-01	-56.77266	-64.25229
LB07-02	-56.77157	-64.25243
LB07-03	-56.76969	-64.25275
LB07-04	-56.76854	-64.25341
LB07-05	-56.76778	-64.25351
LB07-06	-56.76689	-64.25365
LB07-07	-56.76566	-64.25397
LB07-08	-56.76396	-64.25401
LB07-09	-56.76240	-64.25419
LB07-10	-56.76149	-64.25446
LB07-11	-56.76075	-64.25473
LB07-30	-56.75888	-64.25468
LB07-31	-56.75837	-64.25484
LB07-32	-56.75779	-64.25498
LB07-33	-56.75765	-64.25534
LB07-34	-56.75710	-64.25575
LB07-35	-56.75618	-64.25636
LB07-36	-56.75383	-64.25682
LB08-01	-56.74541	-64.25633
LB08-04	-56.74544	-64.25634
LB08-05	-56.74455	-64.25691
LB08-07	-56.74333	-64.25741
LB08-09	-56.74270	-64.25770
LB08-10	-56.74252	-64.25781
LB08-11	-56.74245	-64.25782
LB08-12	-56.74204	-64.25788
LB08-13	-56.74230	-64.25842
LB08-14	-56.74138	-64.25865
LB08-15	-56.73935	-64.25903
LB08-16	-56.73959	-64.25920
LB08-17	-56.73935	-64.25935
LB08-18	-56.73800	-64.25981
LB08-19	-56.73721	-64.25955
LB08-20	-56.73618	-64.25896
LB08-21	-56.73539	-64.25906
LB08-22	-56.73271	-64.26001
LB08-23	-56.73136	-64.25986
LB09-01	-56.72899	-64.26019
LB09-02	-56.72884	-64.26020
LB09-03	-56.72805	-64.26082
LB09-04	-56.72690	-64.26086
LB09-05	-56.72629	-64.26056
LB09-06	-56.72617	-64.26086
LB09-07	-56.72573	-64.26100
LB09-08	-56.72578	-64.26116
LB09-09	-56.72542	-64.26143
LB09-10	-56.72542	-64.26143
LB09-12	-56.72502	-64.26164
LB09-13	-56.72469	-64.26145
LB09-14	-56.72474	-64.26143
LB09-15	-56.72379	-64.26192
LB09-17	-56.72316	-64.26207
LB09-18	-56.72281	-64.26212
LB09-19	-56.72257	-64.26216
LB09-20	-56.72257	-64.26218
LB09-21	-56.72168	-64.26334
LB09-22	-56.72148	-64.26380
LB09-23	-56.72128	-64.26386
LB09-24	-56.72123	-64.26395
LB09-25	-56.72058	-64.26426
LB09-26	-56.71998	-64.26499
LB09-27	-56.72137	-64.27007
LB09-28	-56.72084	-64.27126
LB09-29	-56.72102	-64.27114
LB09-30	-56.72045	-64.27166
LB09-31	-56.72010	-64.27229
LB09-32	-56.71881	-64.27215
LB09-33	-56.71874	-64.27213
LB09-34	-56.71852	-64.27214
LB09-35	-56.71840	-64.27216
LB09-36	-56.71864	-64.27256
LB09-38	-56.71856	-64.27271
LB09-40	-56.71842	-64.27267
LB09-42	-56.72007	-64.27356
LB10-01	-56.72123	-64.27387
LB10-10	-56.72090	-64.27387
LB10-11	-56.71905	-64.27478
LB10-12	-56.71818	-64.27493
LB10-13	-56.71687	-64.27533
LB10-14	-56.71653	-64.27553
LB10-15	-56.71656	-64.27577
LB10-16	-56.71374	-64.27629
LB10-17	-56.71354	-64.27653

Appendix 4.1				
Sample Key for Figures MAP and RESIDUALS, GPS coordinates are available to qualified researchers - please contact one of the first two authors				
Letter	**Type**	**Description**	**Strat and Uncertainty (± 95% analytical, - geological) m**	**Stratigraphic Height for Fossils**
A	K-Pg	near McKeever Ranch 1 (UCMP-V72210)		
B	K-Pg	near Billy Creek 1 (UCMP-V72211) & 2 (V75173)		
C	K-Pg (Impact evidence)	Iridium Hill (no Trimble GPS) see Alvarez (1983)		
D	K-Pg (Impact evidence)	near Herpijunk Promontory (UCMP-V77129)		
E	K-Pg (Impact evidence)	near Herpijunk Promontory (UCMP-V77129)		
F	K-Pg	near Hell's Hollow Channel (UCMP-V74110)		
G	Fossil Sample	L0019 - Hartman (1998)	-10.7 ± 3.0, -2	From Hartman (1998) - beyond areal extent of stratigraphic plane, though consistent with stratigraphic plane value (15m ± 18m)
H	Fossil Sample	MacDonald (UCMP-72201)	33.6 ± 3.3, -15	Stratigraphic plane assignment
I	K-Pg (Impact evidence)	Brownie Butte - see Bohor et al. (1984)		
J	K-Pg	Section G from Fastovsky (1987)		
K	Fossil Sample	L5233A - Hartman (1998)	-26.3 ± 2.8, -3	Stratigraphic plane assignment (matches Hartman 1998)
L	Fossil Sample	L6214 & L6215 - Hartman (1998)	-4.3/-1.5 ± 3.0, 0, L6214-L6215 stratigraphic distance fixed at 2.8m as measured in outcrop	From Hartman (1998) - fault offsets location from strat plane, location is also outside areal extent of stratigraphic plane - mapped fault offset matches strat plane offset within error
M	Fossil Sample	Happy Days	-65.4 ± 2.9, -1	Stratigraphic plane assignment
N	K-Pg (Impact evidence)	Lerbekmo Hill - see Baadsgaard et al. (1998)		
O	Fossil Sample	Gene Gastropod	-20.5 ± 2.6, 0	Stratigraphic plane assignment
P	Fossil Sample	near MicrotetonB (UWBM-C1165)	-66.0 ± 2.5, -6	Stratigraphic plane assignment
Q	K-Pg	near Broken Hart (UCMP-V82026)		
R	Fossil Sample	Shiny Things (UWBM-C1178)	-24.6 ± 3.6, -2.5	Stratigraphic plane assignment
S	K-Pg (Impact evidence)	Flag Butte - see Moore et al. (2014)		
T	Fossil Sample	near Harbaugh Ranch 1 (UWBM-C1420)	53.5 ± 11.6, -1	Stratigraphic plane assignment, outside areal extent of stratigraphic plane control, value matches within error with published geologic maps

U	K-Pg	Carl's Pile			
V	K-Pg	2 km from Yoshi's Microsite (UWBM-C1667)			
W	K-Pg	near Flat Creek 5 (UCMP-V73087)			
X	Fossil Sample	L0010a - Hartman (1998)	35.4 ± 3.0, -10	From Hartman (1998) - beyond strat. plane extent, geologic evidence on the ground contradicts theoretical strat. plane height	
UCMP = University of California Museum of Paleonotology					
UWBM = University of Washington Burke Museum					

Alvarez, L.W., 1983, Experimental evidence that an asteroid impact led to the extinction of many species 65 million years ago: Proceedings of the National Academy of Sciences of the United States of America, v. 80, no. 2, p. 627.

Baadsgaard, H., Lerbekmo, J.F., and McDougall, I., 1988, A radiometric age for the Cretaceous-Tertiary boundary based upon K-Ar, Rb-Sr, and U-Pb ages of bentonites from Alberta, Saskatchewan, and Montana: Canadian Journal of Earth Sciences, v. 25, no. 7, p. 1088–1097.

Bohor, B.F., Foord, E.E., Modreski, P.J., and Triplehorn, D.M., 1984, Mineralogic evidence for an impact event at the Cretaceous-Tertiary boundary: Science, v. 224, no. 4651, p. 867–869.

Fastovsky, D.E., 1987, Paleoenvironments of vertebrate-bearing strata during the Cretaceous-Paleogene transition, eastern Montana and western North Dakota: Palaios,, p. 282–295.

Hartman, J.H., 1998, The biostratigraphy and paleontology of latest Cretaceous and Paleocene freshwater bivalves from the Western Williston Basin, Montana, USA: Bivalves: an eon of evolution: paleobiological studies honoring Norman D. Newell,, p. 317.

Moore, J.R., Wilson, G.P., Sharma, M., Hallock, H.R., and Braman, D.R., 2014, Assessing the relationships of the Hell Creek-Fort Union contact, Cretaceous-Paleogene boundary, and Chicxulub impact ejecta horizon at the Hell Creek Formation lectostratotype, Montana, US: Geological Society of America Special Paper, v. 503, p. 123-136.

Appendix 4.2

Matlab (*.m) file titled KPgSurfaceFit.m

```
function [fitresult,gof] = KPgSurfaceFit(xK, yK, zK)
%CREATESURFACEFIT(XK,YK,ZK)
%  Fit surface to data.
%
%  Data for 'untitled fit 1' fit:
%      X Input : xK
%      Y Input : yK
%      Z output: zK
%      Weights : (none)
%
%  Output:
%      fitresult : an sfit object representing the fit.
%      gof : structure with goodness-of fit info.
%
%  See also FIT, SFIT.

%  Auto-generated by MATLAB on 31-Jul-2013 11:26:46
%  Edited by Tom Tobin shortly afterward to make a standalone m-file
%  Added raw data for constructing K-Pg surface
%  Requires sftool.m
%
%  HOW TO USE:
%  1. Place this file in your working matlab directory (or possibly set
%  path to it)
%  2. Type [model,gof]=KPgSurfaceFit()
%  3. You will see a plot of the surface fit that you can play with
%  4.
%  5. use command:
%  predint(model,[X,Y], 0.95, 'Observation') to find vertical 95% confidence
%  interval bounds for the predicted surface height at any given location
%  described by X,Y as easting and northing coordinates in UTM 13N - check
%  that site is reasonably within areal extent of controlling points
%  6. use model(X,Y) to get calculated surface value for that location
%
%  N.B. Technically some trig should be used to project your sampling
%  location perpendicular to the stratigraphic plane, but due to the
%  shallowness of the dip (0.2 deg) this actually ends up being irrelevant

format long e
%Overrides any other x,y,z data to be the K-Pg surface data
east_x=[    3.550258530000000e+005
    3.239850780000000e+005
    3.366234050000000e+005
    3.367136130000000e+005
    3.378606570000000e+005
    3.253545950000000e+005
    3.252666400000000e+005
    3.865441540000000e+005
    3.865783770000000e+005
    3.482130770000000e+005
    3.540239730000000e+005
    3.828867180000000e+005
```

```
    3.489263380000000e+005
    3.933583190000000e+005
    3.595201380000000e+005];
north_y=[    5.266644810000000e+006
    5.273757185000000e+006
    5.267092774000000e+006
    5.266620670000000e+006
    5.266777047000000e+006
    5.276110774000000e+006
    5.276781925000000e+006
    5.283054277000000e+006
    5.283046457000000e+006
    5.266129535000000e+006
    5.265291846000000e+006
    5.278011040000000e+006
    5.265778457000000e+006
    5.264212543000000e+006
    5.268269448000000e+006];
elev_z=[    8.312411521000000e+002
    9.185127498000001e+002
    8.770822933000000e+002
    8.772815448000000e+002
    8.811629039000000e+002
    9.273169384000000e+002
    9.286120022000000e+002
    8.043067359000000e+002
    8.118614560000000e+002
    8.462170678000000e+002
    8.360298995000001e+002
    8.038597923000000e+002
    8.439968771000000e+002
    7.368498737000000e+002
    8.250231635000000e+002];

xK=east_x;
yK=north_y;
zK=elev_z;
% End added data

%% Fit: 'untitled fit 1'.
ft = fittype( 'poly11' );
opts = fitoptions( ft );
opts.Robust = 'Bisquare';
opts.Weights = zeros(1,0);
[fitresult, gof] = fit( [xK, yK], zK, ft, opts );

% Plot fit with data.
figure( 'Name', 'untitled fit 1' );
h = plot( fitresult, [xK, yK], zK, 'Style', 'PredObs' );
grid on
% Label axes
xlabel( 'xK' );
ylabel( 'yK' );
zlabel( 'zK' );
legend( h, 'untitled fit 1', 'zK vs. xK, yK', 'Location', 'NorthEast' );
```

Appendix 4.3

Analysis	Sample	Batch	Strat	$\delta^{13}C$ (‰)	$\delta^{18}O$ (‰)	ARF Δ_{47}	se	T (Zaarur)	95% (Zaarur)	95% (SE*1.96)	$\delta^{18}O_w$ (‰)	$\delta^{18}O_w$ (err)	Eagle2013 AragoniteT	Eagle2013 BiogenicT	Henkes 2013T
2012_LA_1A_1		2		-8.84	-5.01	0.692	0.017	27.4					29.6	15.9	26.6
2012_LA_1A_2		2		-8.82	-5.01	0.664	0.010	34.5					39.6	22.1	38.9
2012_LA_1A_3	2012-LA-1A	2		-8.96	-4.90	0.698	0.012	26.1					27.7	14.7	24.4
2012_LA_2A_1		2		-8.91	-4.71	0.710	0.013	23.2					23.7	12.1	19.6
2012_LA_2A_2	2012-LA-2A	2		-7.47	-8.40	0.696	0.008	26.5					28.3	15.0	25.1
2012_LA_3A_2		2		-8.84	-3.79	0.716	0.015	21.9					22.0	11.0	17.5
2012_LA_3A_3		2		-8.78	-4.19	0.677	0.014	31.2					34.9	19.2	33.1
2012_LA_3A_4	2012-LA-3A	2		-8.88	-4.15	0.699	0.012	25.9					27.5	14.5	24.1
Lousiana (Modern) Mean:				**-8.63**	**-5.19**	**0.695**	**0.005**	**26.7**	**2.5**	**2.6**	**-3.2**	**0.4**	**28.8**	**15.3**	**25.7**
HC_CC_A_1		2		-5.35	-17.96	0.699	0.014	25.7					27.3	14.4	23.9
HC_CC_A1	HC-CC-A	1		-5.30	-17.89	0.689	0.009	28.3					30.9	16.7	28.2
HC_CC_B1		1		-4.31	-17.66	0.686	0.011	29.1					31.9	17.4	29.5
HC_CC_B2	HC-CC-B	1		-4.36	-17.74	0.694	0.009	26.9					28.9	15.4	25.8
HC_CC_C1		1		-5.40	-16.70	0.720	0.008	20.8					20.5	10.0	15.8
HC_CC_C2	HC-CC-C	1		-5.50	-16.79	0.669	0.010	33.2					37.7	20.9	36.6
HC_CC_D1		1		-4.40	-16.97	0.695	0.014	26.8					28.7	15.3	25.6
HC_CC_D2	HC-CC-D	1		-4.51	-17.49	0.709	0.010	23.4					24.1	12.4	20.1
Site P means:			-66	**-4.89**	**-17.40**	**0.695**	**0.002**	**26.7**	**1.5**	**1.2**	**-15.5**	**0.3**	**28.8**	**15.3**	**25.7**
HC_GG_A1	HC-GG-A	1		0.98	-12.25	0.652	0.009	37.9					44.5	25.1	45.0
HC_GG_B1	HC-GG-B	1		-5.61	-11.83	0.701	0.012	25.3					26.7	14.0	23.1
HC_GG_C1	HC-GG-C	1		-2.36	-9.83	0.684	0.009	29.5					32.5	17.7	30.3
Site O (gastropod) means:			-20.5	**-2.33**	**-11.31**	**0.679**	**0.014**	**30.8**	**7.5**	**7.3**	**-8.6**	**0.8**	**34.6**	**18.9**	**32.8**
HC_HB1_A1		1		-6.00	-9.90	0.711	0.009	23.0					23.5	12.0	19.4
HC_HB1_A2	HC-HB1-A	1		-6.00	-9.90	0.711	0.009	22.9					23.4	11.9	19.3
HC_HB1_C_1		2		-5.76	-9.89	0.723	0.016	20.1					19.6	9.4	14.7
HC_HB1_C1	HC-HB1-C	1		-5.68	-9.94	0.715	0.008	21.9					22.0	11.0	17.6
Site T (bivalve) means:				**-5.86**	**-9.91**	**0.715**	**0.003**	**22.0**	**2.0**	**1.6**	**-8.9**	**0.4**	**22.1**	**11.1**	**17.7**
HC_HB1_G1	HC-HB1-G	1		-8.14	-13.51	0.685	0.008	**29.1**					32.0	17.4	29.6
HC_HB1_H1	HC-HB1-H	1		-6.67	-13.09	0.677	0.011	**31.2**					34.9	19.2	33.1
Site T (gastropod) means:			54	**-7.40**	**-13.30**	**0.681**	**0.004**	**30.1**	**2.0**	**2.0**	**-10.7**	**0.4**	**33.4**	**18.3**	**31.3**
HC_HD_A1		1		-6.88	-8.78	0.673	0.011	32.2					36.3	20.1	34.8

HC_HD_A2		1		-6.85	-8.72	0.699	0.010	25.8					27.3	14.4	23.9
HC_HD_A3	HC-HD-A	1		-6.79	-8.65	0.681	0.010	30.2					33.5	18.3	31.4
HC_HD_B_1		2		-5.83	-11.98	0.716	0.010	21.9					21.9	11.0	17.5
HC_HD_B1	HC-HD-B	1		-5.93	-11.84	0.682	0.010	30.0					33.2	18.2	31.1
HC_HD_D1		1		-6.56	-8.43	0.701	0.008	25.3					26.7	14.0	23.2
HC_HD_D2	HC-HD-D	1		-6.55	-8.45	0.723	0.008	20.3					19.8	9.6	14.9
Site M means:			-66	**-6.43**	**-9.69**	**0.698**	**0.008**	**25.9**	**4.0**	**3.7**	**-7.9**	**0.6**	**27.7**	**14.7**	**24.5**
HC_L5233A_A1		1		-4.12	-8.71	0.694	0.011	27.0					29.0	15.5	26.0
HC_L5233A_A2	HC-L5233A-A	1		-4.01	-8.67	0.697	0.008	26.4					28.2	15.0	25.0
HC_L5233A_B1		1		-5.65	-8.54	0.695	0.010	26.8					28.7	15.3	25.6
HC_L5233A_B2	HC-L5233A-B	1		-5.81	-8.70	0.659	0.009	35.8					41.5	23.3	41.3
HC_L5233A_D_1		2		-5.22	-9.52	0.645	0.012	39.8					47.3	26.8	48.5
HC_L5233A_D_2		2		-5.25	-9.49	0.662	0.011	35.2					40.6	22.7	40.2
HC_L5233A_D1	HC-L5233A-D	1		-5.26	-9.52	0.696	0.009	26.5					28.3	15.1	25.1
Site K means:			-26	**-5.01**	**-8.94**	**0.680**	**0.007**	**30.5**	**3.5**	**3.5**	**-6.3**	**0.5**	**34.1**	**18.7**	**32.3**
HC_MCD_A1		1		-5.67	-10.54	0.686	0.009	29.0					31.8	17.2	29.3
HC_MCD_A2	HC-MCD-A	1		-5.73	-10.55	0.694	0.011	27.0					29.0	15.5	26.0
HC_MCD_B_1		2		-4.59	-10.48	0.701	0.011	25.4					26.8	14.1	23.3
HC_MCD_B1	HC-MCD-B	1		-4.68	-10.61	0.688	0.009	28.6					31.2	16.9	28.6
HC_MCD_D_1		2		-4.32	-10.79	0.657	0.010	36.4					42.4	23.8	42.4
HC_MCD_D_2		2		-4.34	-10.91	0.685	0.015	29.2					32.1	17.5	29.7
HC_MCD_D2	HC-MCD-D	1		-4.65	-10.53	0.703	0.009	24.9					26.1	13.7	22.5
Site H means:			34	**-4.92**	**-10.61**	**0.689**	**0.004**	**28.3**	**2.0**	**1.9**	**-8.4**	**0.4**	**31.0**	**16.7**	**28.4**
HC_ST_B1		1		-7.09	-9.43	0.673	0.010	32.2					36.4	20.1	34.9
HC_ST_B2	HC-ST-B	1		-7.13	-9.36	0.688	0.010	28.5					31.1	16.8	28.4
HC_ST_D1		1		-6.88	-9.59	0.694	0.010	27.0					29.1	15.5	26.0
HC_ST_D2	HC-ST-D	1		-6.90	-9.62	0.666	0.011	34.1					39.1	21.8	38.3
Site R means:			-25	**-7.00**	**-9.50**	**0.680**	**0.000**	**30.4**	**1.5**	**0.2**	**-6.8**	**0.7**	**33.9**	**18.6**	**31.9**
HC_VEIN	**Vein**	**1**	**-15**	**-10.06**	**-14.965**	**0.622**	**0.006**	**46.1**	**4.0**		**-8.6**	**0.5**	**56.7**	**32.3**	**60.4**
S12078_1		2		-7.03	-9.03	0.686	0.008	28.9					31.7	17.2	29.2
S12078_2		2		-7.17	-8.76	0.732	0.010	18.2					17.0	7.7	11.6
S12078_3	S12078	2		-7.12	-8.78	0.693	0.009	27.2					29.3	15.7	26.4
S12079_1		2		-6.46	-10.73	0.712	0.018	22.8					23.3	11.8	19.1
S12079_2	S12079	2		-6.46	-10.87	0.677	0.013	31.2					35.0	19.3	33.2
S12080_1		2		-6.94	-8.67	0.675	0.012	31.7					35.6	19.6	34.0
S12080_3		2		-7.00	-8.75	0.759	0.011	12.3					9.1	2.5	2.5

S12080_4	S12080	2		-6.92	-8.56	0.688	0.011	28.5					31.1	16.9	28.6
Site G means:			-10.7	**-6.84**	**-9.44**	**0.702**	**0.004**	**25.1**	**2.0**	**1.7**	**-7.8**	**0.4**	**26.8**	**14.0**	**23.4**
S12082_1		2		-3.08	-19.82	0.710	0.012	23.2					23.8	12.1	19.7
S12082_2		2		-3.17	-19.60	0.766	0.011	10.9					7.2	1.2	0.3
S12082_3	S12082	2		-3.08	-19.78	0.654	0.017	37.2					43.5	24.5	43.7
S12083_2		2		-4.72	-19.92	0.731	0.011	18.3					17.1	7.8	11.7
S12083_3	S12083	2		-4.65	-19.84	0.676	0.009	31.4					35.2	19.4	33.5
S12085_1		2		-3.35	-20.29	0.702	0.015	25.1					26.3	13.8	22.7
S12085_2		2		-3.44	-20.02	0.736	0.009	17.2					15.6	6.8	10.0
S12085_3	S12085	2		-3.35	-20.18	0.719	0.007	21.0					20.8	10.2	16.1
Site L (L6214) means:			-4.3	**-3.73**	**-19.92**	**0.711**	**0.004**	**22.9**	**2.0**	**2.2**	**-18.8**	**0.4**	**24.0**	**12.2**	**20.0**
S12086_1		2		-5.46	-17.60	0.709	0.007	23.3					24.0	12.3	19.9
S12086_2	S12086	2		-5.82	-14.93	0.679	0.007	30.7					34.2	18.8	32.3
S12087_1		2		-5.23	-17.05	0.702	0.012	25.1					26.4	13.8	22.8
S12087_2	S12087	2		-5.40	-16.90	0.752	0.007	13.9					11.2	3.9	4.9
S12089_1		2		-3.81	-19.82	0.723	0.007	20.1					19.6	9.4	14.7
S12089_2	S12089	2		-3.82	-19.45	0.713	0.015	22.4					22.7	11.4	18.3
S12090_1		2		-4.74	-17.19	0.731	0.013	18.5					17.4	8.0	12.1
S12090_2	S12090	2		-4.73	-17.08	0.690	0.009	28.1					30.6	16.5	27.8
Site L (L6215) means:			-1.5	**-4.88**	**-17.50**	**0.712**	**0.007**	**22.6**	**3.5**	**3.2**	**-16.4**	**0.4**	**23.2**	**11.8**	**19.1**
S13114_1		2		-5.60	-17.30	0.732	0.009	18.2					17.0	7.7	11.7
S13114_2	S13114	2		-5.52	-17.31	0.675	0.007	31.8					35.7	19.7	34.1
S13115_1		2		-5.35	-16.56	0.683	0.015	29.7					32.8	17.9	30.6
S13115_2	S13115	2		-5.34	-16.73	0.711	0.008	22.9					23.3	11.9	19.2
S13116_1		2		-5.20	-18.55	0.732	0.008	18.3					17.1	7.8	11.7
S13116_2	S13116	2		-5.27	-18.70	0.699	0.010	25.8					27.4	14.5	24.0
Site X means:			35	**-5.38**	**-17.52**	**0.705**	**0.005**	**24.3**	**2.5**	**2.5**	**-16.1**	**0.4**	**25.6**	**13.2**	**21.9**

	This study	Dennis2013
Mean of all fossil shells:	0.699	0.683
st.dev:	0.014	0.003
n:	33	4

Bold columns used to generate data for figure

Key to column headings:

Analysis - Unique isotopic analysis name assigned during measurement of sample

Sample - A single fossil specimen

Batch - Whether the sample was run as part of 2010 (Batch 1) or 2012 (Batch 2) set of analyses

Strat - Stratigraphic heigh relative to the K-Pg boundary

d13c, d18o - isotopic values for carbon and oxygen respectively

ARF D47 - Delta47 converted to the Absolute Reference Frame c

se - standard error on D47 analysis

T(zaarur) - temperature calculated using Zaarur 2013 calibration absolute reference fram equation

95% Conf (from Graph) - reading off the expected 95% confidence interval from Zaarur Fig. 2b

95% Conf (samp) - Standard error calculated from average of different sample temperatures, multiplied by 1.96 to get 95% confidence (altman2005)

d18ow - Reconstructed d18O of water

d18ow 1sd = 1 stdev error on d18ow

Eagle2013 (2) - Temperature reconstructed from D47 using 2 different calibrations from Eagle 2013 study

Henkes2013 - Temperature reconstructed using calibration from Henkes 2013 study

Data used to generate Figure 2 are the Bold rows above, and are simplified below

Sample	**Strat**	**d13C**	**d18o**	**ARF D47**	**se**	**T (Zaarur)**	**95% (Zaarur)**	**95% (SE*1.96)**	**d18Ow**	**d18Ow err**	**Eagle2013A ragoniteT**	**Eagle2013 BiogenicT**	**Henkes 2013T**
Lousiana (Modern) Mean:	0	-8.63	-5.19	0.695	0.005	26.7	2.5	2.6	-3.2	0.4	28.8	15.3	25.7
Site P means:	-66	-4.89	-17.40	0.695	0.002	26.7	1.5	1.2	-15.5	0.3	28.8	15.3	25.7
Site O (gastropod) means:	-20.5	-2.33	-11.31	0.679	0.014	30.8	7.5	7.3	-8.6	0.8	34.6	18.9	32.8
Site T (bivalve) means:	0	-5.86	-9.91	0.715	0.003	22.0	2	1.6	-8.9	0.4	22.1	11.1	17.7
Site T (gastropod) means:	54	-7.40	-13.30	0.681	0.004	30.1	2	2.0	-10.7	0.4	33.4	18.3	31.3
Site M means:	-66	-6.43	-9.69	0.698	0.008	25.9	4	3.7	-7.9	0.6	27.7	14.7	24.5
Site K means:	-26	-5.01	-8.94	0.680	0.007	30.5	3.5	3.5	-6.3	0.5	34.1	18.7	32.3
Site H means:	34	-4.92	-10.61	0.689	0.004	28.3	2	1.9	-8.4	0.4	31.0	16.7	28.4
Site R means:	-25	-7.00	-9.50	0.680	0.000	30.4	1.5	0.2	-6.8	0.7	33.9	18.6	31.9
Vein	-15	-10.06	-14.96	0.622	0.006	46.1	4	0.0	-8.6	0.5	56.7	32.3	60.4
Site G means:	-10.7	-6.84	-9.44	0.702	0.004	25.1	2	1.7	-7.8	0.4	26.8	14.0	23.4
Site L (L6214) means:	-4.3	-3.73	-19.92	0.711	0.004	22.9	2	2.2	-18.8	0.4	24.0	12.2	20.0
Site L (L6215) means:	-1.5	-4.88	-17.50	0.712	0.007	22.6	3.5	3.2	-16.4	0.4	23.2	11.8	19.1
Site X means:	35	-5.38	-17.52	0.705	0.005	24.3	2.5	2.5	-16.1	0.4	25.6	13.2	21.9

Appendix 4.4

Appendix 4.4 is hosted online at www.tstobin.com/Tobin_Dissertation_Appendix_4.4.xlsx